AAEC/E558

AAEC/E558

AUSTRALIAN ATOMIC ENERGY COMMISSION

RESEARCH ESTABLISHMENT

LUCAS HEIGHTS RESEARCH LABORATORIES

DEVELOPED SINGLE-PHASE TURBULENT FLOW THROUGH A SQUARE-PITCH ROD CLUSTER FOR AN EXTENDED RANGE OF REYNOLDS NUMBERS

by

*J.D. HOOPER
**D.H. WOOD
W.J. CRAWFORD

* CSIRO Division of Mineral Physics, Lucas Heights Research Laboratories

** Department of Mechanical Engineering, Newcastle University, NSW

June 1983

ISBN 0 642 59773 1

AUSTRALIAN ATOMIC ENERGY COMMISSION
RESEARCH ESTABLISHMENT

LUCAS HEIGHTS RESEARCH LABORATORIES

DEVELOPED SINGLE-PHASE TURBULENT FLOW THROUGH A SQUARE-PITCH ROD CLUSTER FOR AN EXTENDED RANGE OF REYNOLDS NUMBERS

by

*J.D. HOOPER
**D.H. Wood
W.J. CRAWFORD

ABSTRACT

The mean velocity profiles, wall shear stress distribution and all components of the Reynolds stress tensor have been determined from measurements for developed single-phase flow through a square-pitch rod cluster. For a rod pitch-to-diameter ratio of 1.107, four Reynolds numbers, in the range 22.6×10^3 to 207.6×10^3, were investigated. The experimental technique, which involved a rotatable inclined hot-wire anemometer probe, allowed the measurement of secondary flow components of the order of 1 per cent of the local velocity. No evidence was found for secondary flows in the

* CSIRO Division of Mineral Physics, Lucas Heights Research Laboratories.

** Department of Mechanical Engineering, Newcastle University, NSW.

open rod gap area. The highly anisotropic nature of the turbulence, particularly for the interconnecting rod gap region, was shown by the level of the azimuthal turbulent shear stress. The mean velocity profiles were generally consistent with the logarithmic region of the universal velocity profile, using the Patel values for the profile constants. The wall shear stress distribution, measured by Preston tubes, was shown to be symmetrical around the central rods of the array.

National Library of Australia card number and ISBN 0 642 59773 1

The following descriptors have been selected from the INIS Thesaurus to describe the subject content of this report for information retrieval purposes. For further details please refer to IAEA-INIS-12 (INIS: Manual for Indexing) and IAEA-INIS-13 (INIS: Thesaurus) published in Vienna by the International Atomic Energy Agency.

EXPERIMENTAL DATA; FLOW RATE; FUEL ELEMENT CLUSTERS; FUEL RODS; REACTOR LATTICE PARAMETERS; REYNOLDS NUMBER; SHEAR; SQUARE CONFIGURATION; STRESSES; TURBULENT FLOW; VELOCITY

CONTENTS

(Continued)

1. INTRODUCTION

The problem of calculating the coolant velocity distribution, wall shear stress distribution and forced convective heat transfer rates at the surface of heat generating rods is of major interest to the nuclear power industry. Long cylindrical fuel rods are employed in the majority of power reactor cores, and developed flow for single-phase coolants may be expected to apply over most of the rod length. Because of the intractable nature of turbulent flow, prediction of the fluid velocity distribution is a difficult part of the coupled fluid mechanics and heat transfer problem.

Limitation of the upper fuel rod cladding temperature is an important design constraint for all power reactors. Moreover, the advent of the liquid metal-cooled fast breeder reactor, with rod spacing reduced because of neutron moderation and capture, has potentially increased the azimuthal variation of the rod wall shear stress and the associated heat transfer coefficient. The anisotropy of the heat removal process in the rod gap region is of particular importance in closely spaced rod arrays.

Axially developed turbulent single-phase flow is the simplest example of the coolant conditions in a bare rod array. An understanding of this is required before the effect of entry conditions, fuel element grids and spacers, or partial channel blockages can be considered. Relatively few workers have published detailed information on mean velocity distributions and components of the Reynolds stresses for even basic rod bundle flow.

A summary of the published work for bare rod arrays based on a modified survey of Bartzis and Todreas [1977], is given in Table 1. The majority of the experimental studies are for triangular pitch rod arrays. Detection of secondary flow velocity components has been shown to be experimentally difficult for rod bundle geometries, with only one study by Kjellstrom [1974] indicating their presence. Kjellstrom showed a net circulation around one rod of the array, but the secondary flow components were most likely associated with the lack of flow symmetry in the test section. The extensive studies of Rehme [1977a,b; 1978a,b; 1980a,b] for closely spaced rod arrays reported no measurable mean secondary flow velocities.

The study of Seale [1979] is the only distributed parameter experiment to model the heat transfer process in the rod gap area. Here, a long horizontally mounted rectangular duct containing a single row of rods

regularly spaced at three p/d ratios was used. Heat transfer was not from the rod surface to the air coolant, but from the heated top wall of the duct to the water-cooled lower wall. Insulated rod walls reduced the rod conduction to about 2 per cent of the total heat flow. Seale [1979] found the effective eddy heat diffusivities in the rod gap to be strongly anisotropic, with no evidence of mean secondary flow.

The objective of the present work was to investigate experimentally the flow structure of axially developed single phase turbulent flow through a square-pitch rod array having a pitch-to-diameter (p/d) ratio of 1.107. The dependence of the mean velocity distribution, wall shear stress distribution and Reynolds stresses was investigated for the Reynolds number range 22.6 x 10^3 to 207.6 x 10^3. Typical results are discussed in this report, and the complete data bank is given in Hooper et al. [1983].

2. EQUATIONS OF MOTION

The continuity equation and the fluid momentum or Navier-Stokes equations for a constant viscosity and density fluid in polar coordinates are [Hinze 1975:28] :

$$\frac{\partial U}{\partial z} + \frac{1}{r}\frac{\partial (rV)}{\partial r} + \frac{1}{r}\frac{\partial W}{\partial \theta} = 0 \tag{1}$$

z axis momentum:

$$\rho \frac{DU}{Dt} = -\frac{\partial P}{\partial z} + \mu\nabla^2 U - \rho \frac{\partial \overline{u^2}}{\partial z} - \frac{\rho}{r}\frac{\partial (\overline{ruv})}{\partial r} - \frac{\rho}{r}\frac{\partial \overline{uw}}{\partial \theta} + F_z \tag{2}$$

r axis momentum:

$$\rho\left(\frac{DV}{Dt} - \frac{W^2}{r}\right) = -\frac{\partial P}{\partial r} + \mu\left(\nabla^2 V - \frac{V}{r^2} - \frac{2}{r^2}\frac{\partial W}{\partial \theta}\right) - \frac{\rho}{r}\frac{\partial(r\overline{v^2})}{\partial r} - \frac{\rho}{r}\frac{\partial \overline{vw}}{\partial \theta} - \rho\frac{\partial \overline{uv}}{\partial z} + \rho\frac{\overline{w^2}}{r} + F_r \tag{3}$$

θ axis momentum:

$$\rho\left(\frac{DW}{Dt} + \frac{VW}{r}\right) = -\frac{1}{r}\frac{\partial P}{\partial \theta} + \mu\left(\nabla^2 W - \frac{W}{r^2} + \frac{2}{r^2}\frac{\partial V}{\partial \theta}\right)$$

$$- \frac{\rho}{r} \frac{\partial \overline{w^2}}{\partial \theta} - \rho \frac{\partial \overline{vw}}{\partial r} - \rho \frac{\partial \overline{uw}}{\partial z} - 2\rho \frac{\overline{vw}}{r} + F_\theta \qquad (4)$$

The ∇^2 operator represents

$$\frac{\partial}{\partial z^2} + \frac{\partial^2}{\partial r^2} + \frac{1}{r} \frac{\partial}{\partial r} + \frac{1}{r^2} \frac{\partial^2}{\partial \theta^2}$$

and the fluid total derivative

$$\frac{D}{Dt} = \frac{\partial}{\partial t} + U \frac{\partial}{\partial z} + V \frac{\partial}{\partial r} + \frac{W}{r} \frac{\partial}{\partial \theta}$$

For the horizontally mounted six-rod cluster air rig used in this study, the body forces (F_z, F_r and F_θ) may be taken as zero.

3. SQUARE-PITCH ROD SUBCHANNEL TEST SECTION

The square-pitch rod subchannel test section was designed to model the fluid mechanics of axially developed turbulent single phase flow through a closely spaced rod cluster. A square-pitch geometry was selected for the study; most of the reported work (Table 1) has been for triangular arrays. A numerical study of rod bundle flow by the ROFLO code [Hooper 1975] showed that for the same (p/d) ratio and Reynolds number, the wall shear stress distribution in an axial plane is substantially higher for the square-pitch than for the triangular-pitch array.

A large variation in the wall shear stress distribution was considered to be associated with a significant departure of the turbulent flow structure from axisymmetric pipe flow conditions.

The cross-section of the test section is shown in Figure 1a. The two interconnected subchannels were intended to represent, for the -45 to 45° segment about the top and lower centre-line rods, the repeated symmetrical zone of an interior subchannel in a large square-pitch array. The presence of the walls in the rod gap is shown for laminar flow to introduce an error of less than 1 per cent in the mean velocity at the subchannel centre, calculated by the ROFLO [Hooper 1975] code for p/d ratios less than 1.20. For turbulent flow, neglecting the effect of secondary flows, the effect of the rod gap walls would be further reduced by the higher mean velocity gradients near wall boundaries.

The scale of the rig was made as large as possible, consistent with the need to have at least 80 hydraulic diameters for flow development. Subbotin et al. [1971a] have suggested that between 13 and 17 hydraulic diameters are required to stabilise the axial pressure gradient, and up to 50 hydraulic diameters to establish a developed mean velocity profile. The test section length was 9.14 m, and the outside diameter of the rods forming the test section 140 mm. Measurements were normally made 50 or 100 mm upstream of the rig exit. A general arrangement of the rig is shown in Figure 1b, with the open loop system being powered by a 45 kW centrifugal blower. The test-section entry was attached directly to the 1.20 m diameter by 1.50 m long flow settling drum; this drum had a fine mesh internal screen, and its entry pipe elbow had turning vanes to ensure more uniform flow entry conditions to the test-section. An orifice plate was located in the 0.10 m i.d. pipe connecting the blower to the settling drum.

The axial static pressure gradient was determined by 19 static tap stations, spaced equally at 457 mm intervals along the test-section. Each static tap location consisted of three 1.20 mm diameter holes located centrally in the strips forming the rod gap walls, and interconnected by a piezometric ring (Figure 1a). The replacement of the aluminium strips in slots machined along the test-section rods allowed the rig to operate at different p/d ratios, although only one value (1.107) was examined in this work. The equivalent infinite square-pitch rod array hydraulic diameter is given by Equation 5, and the subchannel hydraulic diameter by Equation 6:

$$d_{h_\infty} = 4\,d\,((p/d)^2 - \tfrac{\pi}{4})/\pi \tag{5}$$

$$d_{h_s} = 4\,d\,((p/d)^2 - \tfrac{\pi}{4})/(\pi + 3((p/d) - 1)) \tag{6}$$

The hydraulic diameters and flow development lengths are given in Table 2. The infinite array hydraulic diameter and the average velocity for the -45 to 45° segment about the top and lower central rods of the array were used to calculate experimental Reynolds numbers.

The surfaces of the aluminium rods were highly polished, and the three segments of each rod joined axially were aligned to ensure that no steps or wall roughness elements higher than 0.02 mm were present. A polar scanning system, capable of motorised traverse in both the radial and azimuthal directions, was designed to be located in any of the six rods at the test-section exit. Geared Slo-Syn pulse-operated motors were used for both

traverse directions. When under computer control, the resolution for the radial traverse was ± 0.02 mm and the azimuthal traverse 0.3°. Both traverse directions could be operated manually with the same accuracy.

The computerised measurement of the six terms of the Reynolds stress tensor, even when limited to the symmetry zone about the top and lower centre-rods of the array, is a task requiring approximately 150 hours for each rod and Reynolds number. Automatic measurement, using a two element hot-wire anemometer probe as sensor, and a PDP11/10 for rig control and data processing, are described by Hooper [1980] and Hooper and Harris [1981].

4. MEAN FLOW RESULTS

Complete experimental data of the mean velocity distribution, wall shear stress distribution and Reynolds stresses for the four Reynolds numbers (22.6×10^3, 46.3×10^3, 133.0×10^3 and 207.6×10^3) are presented in tabular form by Hooper et al. [1983], and typical results are given in the present report. The $Re = 46.3 \times 10^3$ study was conducted with the air flow through the test section reversed, and the measurement plane located 25 mm upstream of the test-section exit into the flow settling drum. Additional studies at approximately the same Reynolds number [Hooper 1980] for the normal flow direction showed the same experimental results for the mean flow and Reynolds stress measurements. The data for the three lower Reynolds numbers were measured from the top centre-line rod. Antisymmetric components of the Reynolds stresses, with respect to the symmetry line at 0° from the top and lower central rods of the array, change sign when the cylindrical coordinate system is relocated from the top to lower rod.

4.1 Wall Shear Stress Distribution

The wall shear stress distribution for the centre-line rods of the array, normalised by the average rod shear stress, is shown in Figure 2(a) for the four Reynolds numbers. The shear stress was measured by Preston tubes, using the correlations of Patel [1965]. There is some evidence that the azimuthal shear stress variation depends on Reynolds number, since the normalised shear stresses are slightly lower in the rod gap at 0° for the lower mean velocities. In common with the experimental results of Fakory and Todreas [1979], using a triangular pitch rod array spaced at a p/d ratio of 1.10, and Rehme [1978a; 1979a; 1980a,b], using a square-pitch rod array spaced at a p/d

ratio of 1.07, the wall shear stress increases monotonically from the central rod gap at 0° to the subchannel diagonal at ± 45°.

The symmetry of the shear stress distribution about the top and lower central rods of the array for Re = 133.0 x 10^3 is shown in Figure 2b, which also demonstrates the consistency of the Patel [1965] correlations for a range of Preston tube diameters. The normalised shear stress distribution for the lower left-hand rod on the outside of the test-section is also shown in Figure 2b. The variation for this outer rod shows a local minimum in the wall shear stress at -45°. The lack of symmetry of the outer rod shear stress distribution, in contrast to the central rods of the array, is an effect associated with the rod gap walls. Radial traverses at ±45° from the central rods of the array, which form lines of symmetry in large rod arrays, therefore only approximate lines of symmetry in the test-section.

4.2 Mean Velocity Profiles

The dimensionless mean velocity profiles for the turbulent core at Re = 22.6 x 10^3 are shown in Figures 3a and b. Similar profiles for Re = 207.6 x 10^3 are shown in Figures 4a and b. For comparison, the logarithmic velocity profiles given by

$$U^+(r,\theta) = \frac{1}{\kappa} \ell n\, y^+ + C \qquad (7)$$

are also shown in these figures.

The value of the Von Karman constant κ has been taken as 0.4187 (as suggested by Patel [1965]), and the corresponding value of the constant C is 5.45. It is apparent that for Re = 22.6 x 10^3 the mean velocity points are below the logarithmic distribution for all radial traverses. However, for Re = 207.6 x 10^3, the data are well described by the Patel [1965] version of the logarithmic profile. This agreement of the mean velocity data with the logarithmic profile is common to all studies except that performed at the lowest Reynolds number. Rehme [1978a; 1980a,b] used the Nikuradse values of 0.40 and 5.5 for κ and C respectively, and his data points fall slightly below the logarithmic distribution. The Nikuradse values were also used by Kjellstrom [1974] and Subbotin et al. [1971b].

There are no universally agreed numerical values for κ and the corresponding constant C [Hooper 1980]. The use of the Patel [1965] values

is, however, consistent with the use of the Patel [1965] interpretation of Preston tube data. Agreement between Equation 7 and the experimental velocities supports the use of these correlations in a geometry very different to the flat plate boundary layer and axisymmetric pipe flow used to establish them.

The rotatable, inclined hot-wire anemometer probe used to measure all terms of the Reynolds stress tensor, was also used to establish the direction of the mean velocity vector. Assuming a cosine response for the probe [Hooper 1980; Hooper and Harris 1981], it can be shown that the average anemometer bridge voltage must be measured to an accuracy of ± 0.15 per cent to resolve a secondary flow component of velocity V or W which is 1 per cent of the local axial velocity U. Using ensembles of the anemometer bridge voltage filtered by an 8 second passive low pass filter and averaged over approximately two minutes, a computer-calculated mean enabled this level of accuracy to be achieved. There was no evidence of non-zero values for V and W in the open rod gap for any of the radial traverses or Reynolds numbers investigated. This is consistent with the result of Rehme [1977a,b; 1978a,b; 1980a,b], who reported no significant secondary flow components for any of his studies in a square-pitch array.

5. TURBULENCE MEASUREMENTS

5.1 Reynolds Stresses

The Reynolds shear stress data at each Reynolds number and radial traverse were normalised by dividing by the local wall shear stress; similarly the turbulent intensities u', v' and w' were normalised to the local friction velocity $v^*(\theta)$. The turbulence-intensity data of Laufer [1954] and Lawn [1971] for axisymmetric developed pipe flow are also shown for comparison with the present rod cluster results. It should be noted however that although Lawn's data indicated no dependence of turbulence intensity on Reynolds number, this was not so with Laufer's data. Only the Laufer study for $Re = 500 \times 10^3$ is used for comparison.

5.1.1 Axial turbulence intensity u'

The axial turbulence intensity u' for $Re = 22.6 \times 10^3$ is shown in Figures 5a and b, and for $Re = 207.6 \times 10^3$ in Figures 6a and b. The elevation of u'

above levels typical of pipe flow for the rod gap region is a feature common to both Reynolds numbers. The location of the maximum level of u' for the traverses at ± 15° is also evident in both studies. The data of Hooper et al. [1983] for the intermediate Reynolds numbers of 46.3 x 10^3 and 133.0 x 10^3 also confirm this observation. However, there is evidence of a progressive increase in the general level of the axial turbulence intensity as the Reynolds number is increased. This may be partly due to the scaling effects shown by the mean velocity results, and the over-prediction of the wall shear stress by the Patel [1965] correlations for the lowest Reynolds number of 22.6 x 10^3.

The traverse at 0° is geometrically a symmetry line of the test-section. Within reasonable limits, the reflection of the experimental results about this radial traverse shows the same symmetry. Analytically, the axial turbulence intensity is a symmetric function in rod subchannels. The distribution at 45°, particularly for the high Reynolds number study, is similar to the results obtained by Laufer [1954] and Lawn [1971] for axisymmetric developed pipe flow.

5.1.2 Radial turbulence intensity v'

Figures 7a and 8a show that the normalised radial turbulence intensities v' in the rod gap are of the same order of magnitude as the pipe flow levels established for Re = 22.6 x 10^3 and 207.6 x 10^3. The limiting values of the $v'/v^*(\theta)$ component in the rod gap may be a result of the small distance between the opposing rod walls acting as a constraint on the turbulence scale in the r-z plane.

The distributions at 45° for both Reynolds numbers approximate pipe flow results (Figures 7b and 8b), although the data for the lower Reynolds number are again reduced in magnitude. The symmetry of the $v'/v^*(\theta)$ component about the 45° radial traverse is reasonable at both Reynolds numbers, the results for the 40° traverse being approximately equal to those at the 50° traverse.

5.1.3 Azimuthal turbulence intensity w'

The azimuthal turbulence intensity w', when scaled by the local wall friction velocity, reaches a local maximum for the traverse at 0° for both Reynolds numbers investigated (Figures 9a and 10a). The distribution is effectively independent of the wall distance for the traverses in the rod gap

area, and values of w' are considerably greater than those for the corresponding pipe flow. This result is an indication of a significant momentum interchange between the two subchannels. In common with the axial and radial turbulence intensity, the azimuthal component w' is both analytically, and approximately experimentally, symmetric about the rig geometrical symmetry lines. There is, however, some lack of symmetry in the experimental results of w' about the 0° traverse. The distributions at the other line of symmetry, i.e. 45°, (Figures 9b and 10b) again approximate the distributions typical of developed pipe flow, particularly for the higher Reynolds number study.

5.1.4 Radial turbulent shear stress $-\rho\ \overline{uv}$

The radial turbulent shear stress $-\rho\ \overline{uv}$ has a linear distribution in the rod gap at both Reynolds numbers (Figures 11a and 12a), and approaches the local wall shear stress (or unity when normalised by $\tau_w(\theta)$) as the wall is neared. From the axial momentum equation (Equation 2) for this line of symmetry, it can be seen that there are two extra terms to the axisymmetric developed pipe flow form of the equation; the advection term $\rho V(\partial U/\partial r)$; and the azimuthal gradient of the Reynolds shear stress $-\rho/r(\partial \overline{uw}/\partial\theta)$. Direct measurement of the secondary flow component V showed its magnitude to be less than 1 per cent of the local axial velocity U, but the advection term may still contribute to the axial momentum balance. The azimuthal gradient of $-\rho\ \overline{uw}$ is also not zero for the 0° radial traverse. However, the radial turbulent shear stress for the 0° line of symmetry is similar to the distribution of that component of the Reynolds shear stresses for developed pipe flow.

Away from this line of symmetry, the normalised $-\rho\ \overline{uv}$ distribution departs markedly from the linear distribution, which passes through unity at $y/y_{max} = 0$ (Figures 11b and 12b). The other possible line of symmetry (45°) does not have a linear distribution at either of the Reynolds numbers shown in Figures 11b and 12b, or in the complete data bank [Hooper et al. 1983]. The normalised radial turbulent shear stress is analytically a symmetric function about the subchannel diagonal at 45° for a large array, but the experimental results for traverses at 40° and 50° are not identical. The result is associated with the rod gap walls, and shows that the presence of these walls significantly changes the flow structure in the rod gap.

5.1.5 Azimuthal turbulent shear stress $-\rho \overline{uw}$

Analytically, the normalised azimuthal turbulent shear stress $-\rho \overline{uw}$ is antisymmetric for lines of symmetry. The experimental results for Re 22.6 x 10^3 (Figure 13a) and Re = 207.6 x 10^3 (Figure 14a) show this feature about the 0° measurement plane. The magnitude of $-\rho \overline{uw}$ is very close to the expected value of zero for the 0° traverse angle. The $-\rho \overline{uw}$ component of the Reynolds shear stresses increases in a remarkable manner away from the rod gap; at the centre of the 15° traverse, it becomes 1.2 $\tau_w(\theta)$ for Re = 22.6 x 10^3, and 1.6 $\tau_w(\theta)$ for Re = 207.6 x 10^3. As with other components of the Reynolds stresses, part of the Reynolds number dependence of the magnitude of $-\rho \overline{uw}$ may be related to an over-estimate of the wall shear stress by the Preston tube measurements for the lowest Reynolds number. A similar increase in the level of $-\rho \overline{uw}$ near the centre of the rod gaps was noted by Rehme [1977a; 1978a; 1980a,b] in his studies of a rod array with a p/d ratio of 1.07. This effect is linked to the energetic momentum interchange process between the subchannels of closely spaced rod arrays. The normalised values of $-\rho \overline{uw}$ are almost zero for the subchannel diagonal at 45° (Figures 13b and 14b). Additionally, the behaviour of $-\rho \overline{uw}$ is approximately antisymmetric with respect to this traverse angle.

5.1.6 Transverse Reynolds shear stress $-\rho \overline{vw}$

The transverse Reynolds shear $-\rho \overline{vw}$ is difficult to measure accurately with the rotatable inclined hot-wire probe, since essentially it is a measure of the difference of two large quantities [Hooper 1980]. However, the non-zero level of $-\rho \overline{vw}$ for the rod gap area, and its antisymmetric behaviour across the 0° traverse, were shown by the data for all four studies. The results at Re = 22.6 x 10^3 (Figures 15a and b) show that $-\rho \overline{uw}$ reaches a maximum level for the 15° traverse angle. The data are not, however, symmetrical with respect to the traverse angle at 0°. For traverse angles greater than approximately 35°, $-\rho \overline{vw}$ is effectively zero.

The same features are present in the study at Re = 207.6 x 10^3 (Figures 16a and b) and in the complete data bank for the four Reynolds numbers [Hooper et al. 1983].

5.2 Axial Momentum Balance

The axial momentum equation (Equation 2) may be integrated radially from the rod wall at R to a wall distance y. If the viscous term is ignored, except for its magnitude at the rod wall, where $\tau_w(\theta)$ is equal to $\mu(\partial U/\partial r)$, the integral becomes:

$$\rho \int_R^{R+y} r\left(V \frac{\partial U}{\partial r} + \frac{W}{r} \frac{\partial U}{\partial \theta}\right) dr = - \frac{\partial p}{\partial z} \left(\frac{y^2 + 2Ry}{2}\right) - R\, \tau_w(\theta)$$

$$- \rho\, \overline{uv}\, (y + R) - \rho \int_R^{R+y} \frac{\partial uw}{\partial \theta}\, dr \qquad (8)$$

The advection terms of the momentum integral equation for the axial direction thus become the unknown or balance terms of Equation 8, in which all other quantities are known or may be calculated. The axial momentum equation may therefore be used to assess the importance of the secondary velocity components V and W, and for the symmetry line at 0°, W may be assumed to be zero. A further analysis of the possible distribution of V and W is discussed by Wood [1981].

The calculated azimuthal gradient of the azimuthal shear stress contains the most uncertainties. However, a central finite difference scheme for this term was used [Hooper 1980] and, in the radial integral, the term was assumed to vary linearly from zero at the wall to the first measured value. The axial momentum balance for Re = 22.6 x 10^3 and the azimuthal angles 0, 15, 25 and 45° is shown in Figures 17a to d and for Re = 207.6 x 10^3 in Figures 18a to d.

It is apparent that the advection term contribution, D, to the axial momentum balance is small for all angles. Also, the radial integral of the azimuthal gradient of the Reynolds shear stress $-\rho\, \overline{uw}$, C, is most important at 0°. For the latter traverse angle, the term becomes larger at the duct centre-line than either the pressure term, B, or the radial Reynolds shear stress $-\rho\, \overline{uv}$, A. The terms of Equation 8 have been normalised by $\tau_w(\theta) \cdot y_{max}$.

5.3 Turbulent Kinetic Energy and the Ratio A2

The turbulent kinetic energy, defined as 1/2 $(u'^2 + v'^2 + w'^2)$ and normalised by $v^{*2}(\theta)$, is shown for Re = 22.6 x 10^3 in Figures 19a and b and for Re = 207.6 x 10^3 in Figures 20a and b. The lower magnitude of the

turbulent kinetic energy for the lower Reynolds number at all radial traverse angles is apparent. The elevation of the turbulent kinetic energy above the level determined by Lawn [1971] for axisymmetric developed pipe flow in the rod gap is also shown at both Reynolds numbers; this effect is consistent with the convection of higher energy fluid from the subchannel centre to the rod gap. The distribution for the 45° traverse is similar to the Lawn [1971] results for the highest Reynolds number investigated.

The ratio of the algebraic sum of the radial and azimuthal Reynolds shear stresses to the normal Reynolds stress is shown in Figures 21a and b at Re = 22.6×10^3, and in Figures 22a and b at Re = 207.6×10^3. The ratio A2 is defined as

$$A2 = \frac{\sqrt{\overline{uv}^2 + \overline{uw}^2}}{u'^2 + v'^2 + w'^2} \qquad (9)$$

and is used as a constant in some numerical models of single-phase turbulent flows. As can be seen, however, the ratio is far from constant for the rod bundle geometry.

6. CONCLUSIONS

The experimental results for the wall shear stress variation, and comparisons of the axial velocity profiles with a standard form of logarithmic distribution showed that the normalised mean flow structure is substantially independent of Reynolds number for Reynolds numbers of 46.3×10^3, 133.0×10^3 and 207.6×10^3. There was, however, some discrepancy between the logarithmic distribution and the mean axial velocity data for the lowest Reynolds number of 22.6×10^3.

The Reynolds stresses were approximately independent of Reynolds number for the three highest Reynolds number studies, but the magnitudes of all six components of the Reynolds stresses were lower for Re = 22.6×10^3.

There was no direct experimental evidence of secondary flow components V and W within the level of accuracy of measurement, approximately ± 1 per cent of the local axial velocity U. The relative unimportance of the secondary flow components to the axial momentum balance was shown by numerical integration of the axial momentum equation. The contribution of the advection term, containing the secondary flow velocities V and W, to this balance was

shown to be insignificant.

7. REFERENCES

Bartzis, J.G. and Todreas, N.E. [1977] - Hydrodynamic behaviour of a bare rod bundle. ERDA COO-22445-48TP.

Carajilescov, P. and Todreas, N.E. [1975] - Experimental and analytical study of axial turbulent flows in an interior subchannel of a bare rod bundle. Paper HT/51, ASME Winter Annual Meeting.

Chieng, C.C. and Lin C. [1979] - Velocity distribution in the peripheral subchannels of the CANDU-type 19-rod bundle. Nucl. Eng. Des., 55:389.

Eifler, W. and Nijsing, R. [1967] - Experimental investigation of velocity distribution and flow resistance in a triangular array of parallel rods. Nucl. Eng. Des., 5:22.

Fakory, M. and Todreas, N.E. [1979] - Experimental investigation of flow resistance and wall shear stress in the interior subchannel of a triangular array of parallel rods. J. Fluids Eng., 101:429.

Hinze. J.O. [1975] - Turbulence (2nd ed.). McGraw Hill, New York.

Hooper, J.D. [1975] - The calculation of fully developed turbulent and laminar single-phase flow in four rod subchannels. AAEC/E351.

Hooper, J.D. [1980] - Fully developed turbulent flow through a rod cluster. Ph.D Thesis, School of Nuclear Engineering, University of NSW.

Hooper, J.D. and Harris, R.W. [1981] - Hot wire anemometry techniques for an automated rig. AAEC/E516.

Hooper, J.D., Wood, D.H. and Crawford, W.J. [1983] - Data bank of developed single-phase flow through a square-pitched rod cluster for four Reynolds numbers. AAEC/E559.

Kjellstrom, B.[1974] - Studies of turbulent flow parallel to a rod bundle of triangular array. AE-487.

Laufer, J. [1954] - The structure of turbulence in fully developed pipe flow. NACA 1174.

Lawn, C.J. [1971] - The determination of the rate of dissipation in turbulent pipe flow. J. Fluid Mech., 48(3)477.

Patel, V.C. [1965] - Calibration of Preston tube and limitations on its use in pressure gradients. J. Fluid Mech., 23(1)185.

Rehme, K. [1977a] - Measurements of the velocity, turbulence and wall shear stress distributions in a corner channel of a rod bundle. KfK-2512.

Rehme, K. [1977b] - Turbulent flow through a wall subchannel of a rod bundle. KfK-2617.

Rehme, K. [1978a] - The structure of turbulent flow through a wall subchannel of a rod bundle. Nucl. Eng. Des., 45:311.

Rehme, K. [1978b] - The structure of turbulent flow through a wall subchannel of a rod bundle with roughened ribs. KfK-2716.

Rehme, K. [1980a] - Experimental investigations of turbulent flow through an asymmetric rod bundle. KfK-3047.

Rehme, K. [1980b] - Experimental investigation on the fluid flow through an asymmetric rod bundle. KfK-3069.

Rowe, D.S. [1973] - Measurement of the turbulence intensity scale and velocity in rod bundle flow channels. BNWL-1736.

Seale, W.J. [1979] - Turbulent diffusion of heat between connected flow passages. Nucl. Eng. Des., 54:183.

Subbotin, V.I., Ushakov, P.A., Leuchenko, Yu. D and Bibkov, L.N. [1971a] - Study of the velocity profiles in the inlet section of densely packed bundles of rods. Heat Transfer - Soviet Res., 3(5)1.

Subbotin, V.I., Ushakov, P.A., Leuchenko, Yu. D. and Aleksandrov, A.M. [1971b] - Velocity field in turbulent flow past rod bundles. Heat Transfer - Soviet Res., 3(2)9.

Trupp, A.C. and Azad, R.S. [1975] - The structure of turbulent flow in a triangular array rod bundle. Nucl. Eng. Des., 32:47.

Vouka, V. and Hoornstra, J. [1979] - A hydraulic experiment to support calculations of heat mixing between reactor subchannels. 2nd Symposium on Turbulent Shear Flows, London, July.

Wood, D.H. [1981] - The equations describing secondary flow in cylindrical polar coordinates. University of Newcastle, NSW, TN-FM61.

8. NOTATION

A2	ratio of algebraic sum of radial and azimuthal Reynolds shear stresses to algebraic sum of normal Reynolds stresses
C	constant in logarithmic law of wall
d_h	hydraulic diameter
d	rod diameter
F	fluid body force
ℓ	length of rig
p	rod pitch
P	pressure
p/d	rod pitch/diameter ratio
q	turbulent kinetic energy
R	pipe radius

Re	Reynolds number
U,V,W	mean velocity components in z,r,θ direction
u,v,w	fluctuating velocity components in z,r,θ direction
u',v',w'	normalised axial, radial and azimuthal turbulence intensity
v*	friction velocity
y	wall distance
y^+	dimensionless wall distance
y_{max}	distance from rod wall to subchannel centre-line of symmetry

Greek Symbols

τ_w	wall shear stress
ν	kinematic viscosity
μ	dynamic viscosity
ρ	air density
κ	Von Karman constant

Subscripts

z,r,θ	component resolved along designated polar coordinate axis
w	wall value
s	test section value
∞	value for large symmetrical array

Superscripts

'	r.m.s. quantity
___	time-averaged quantity

TABLE 1

DISTRIBUTED PARAMETER MEASUREMENTS OF DEVELOPED SINGLE-PHASE TURBULENT FLOW IN A BARE ROD BUNDLE

Experimenter	p/d	ℓ/d_n	$Re/10^3$	Mean Velocity		Intensities	Reynolds stresses	Technique	$\tau_w(0)$	Array
				Axial U	Secondary V,W	u', v', w'	$-\rho\overline{uv}, -\rho\overline{uw}, -\rho\overline{vw}$			
Eifler & Nijsing (1967)	1.05 1.10 1.15	139 90 65	15.0,30.0,50.0 " " "	* * *				Pitot tube		Triangular
Subbotin *et al.* (1971b)	1.05 1.10 1.20	154 100 72	18.8-31.0 " "	* * *				Pitot, Preston tubes	*	Triangular
Rowe (1973)	1.25 1.125	85 -	50-200 "	* *		* * * *		Laser-Doppler anemometer		Square/ mixed geometry
Kjellstrom (1974)	1.217	81	149-373	*	*	* * *	* *	Preston tube H.W.anemometer	*	Triangular
Trupp & Azad (1975)	1.50 1.35 1.20	20 30 51	12-84 "	* *		* * * * * *	* * * *	H.W.anemometer Pitot, Preston tubes	 *	Triangular
Carajilescov & Todreas (1975)	1.123	77	27	*		*	*	Laser-Doppler anemometer		Triangular
Bartzie & Todreas (1977)	1.124	77	9,26.3,65	*		* * *	* *	Laser-Doppler		Triangular
Rehme(1977a) (1977b) (1978a) (1978b) (1980a) (1980b)	1.07 1.15 1.07 1.45 1.07 1.07	177 143 177 66 177 177	59.7 123 87 182 107 75.7	* * * * * *		* * * * * * * * * * * * * * * * * *	* * * * * * * * * * * *	Pitot, Preston tubes H.W.anemometer	* * * * * *	Square-edge
Fakory & Todreas (1979)	1.10	182	9.11 36.2	* *				Pitot, Preston tubes	*	Triangular
Vouka & Hoornstra (1979)	1.30	117	140	*			*	Laser-Doppler anemometer		Triangular/ mixed geometry
Chieng & Lin (1979)	1.149	-	-	*		*		Laser-Doppler anemometer		Mixed+
Seale † (1979)	1.833 1.375 1.10	216 469 996	34.4-299 45.8-189 46.2-91.1	* * *				Pitot probe and thermo-couple survey		Square-edge channel
Hooper (1980)	1.107 1.194		48 48-156	* *		* * * * * *	* * * * * *	Pitot, Preston tubes H.W.anemometer	* *	Square

† Data of Seale includes temperature fields

+ Mixed array denotes a combination of square, triangular and edge subchannels

TABLE 2

HYDRAULIC DIAMETERS AND FLOW DEVELOPMENT LENGTHS

(p/d)	d_{h_∞} mm	d_{h_s} mm	ℓ/d_{h_∞}	ℓ/d_{h_s}
1.107	78.44	71.17	117	128

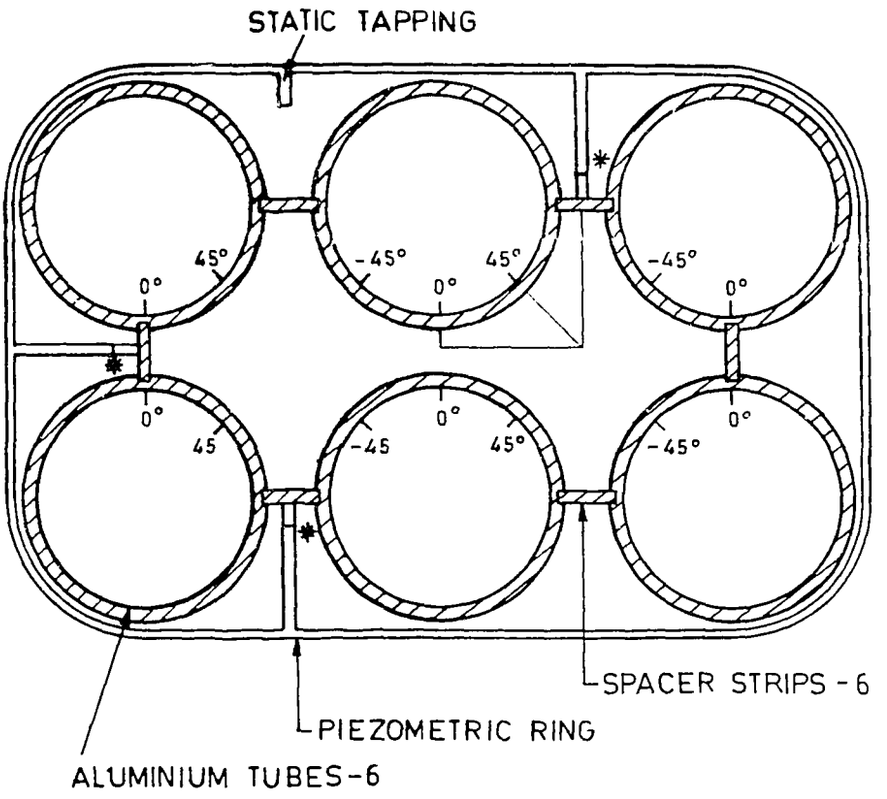

* – STATIC TAP POINTS

FIGURE 1a. CROSS-SECTION OF SIX-ROD CLUSTER

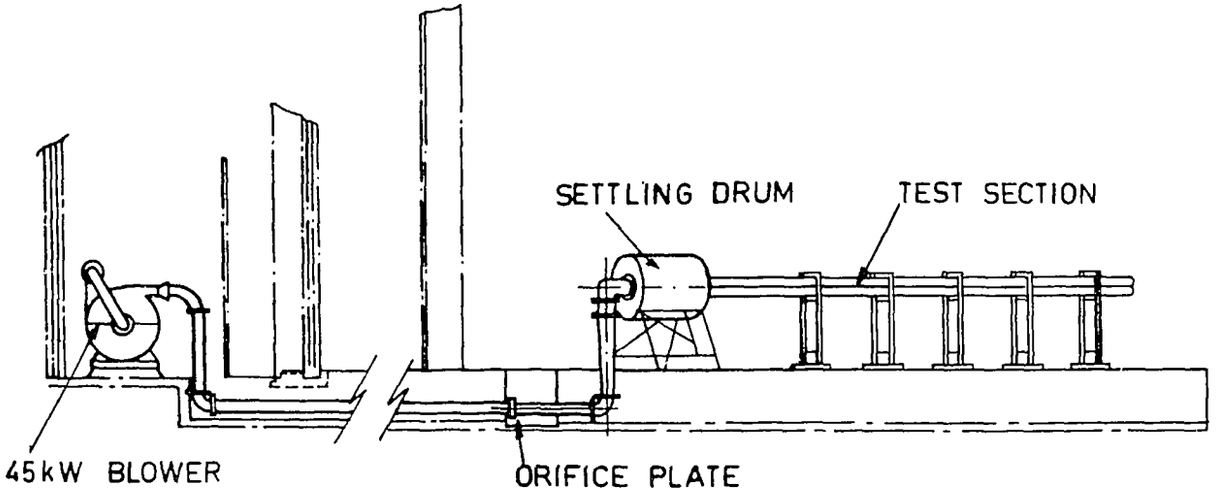

FIGURE 1b GENERAL ARRANGEMENT OF TEST RIG

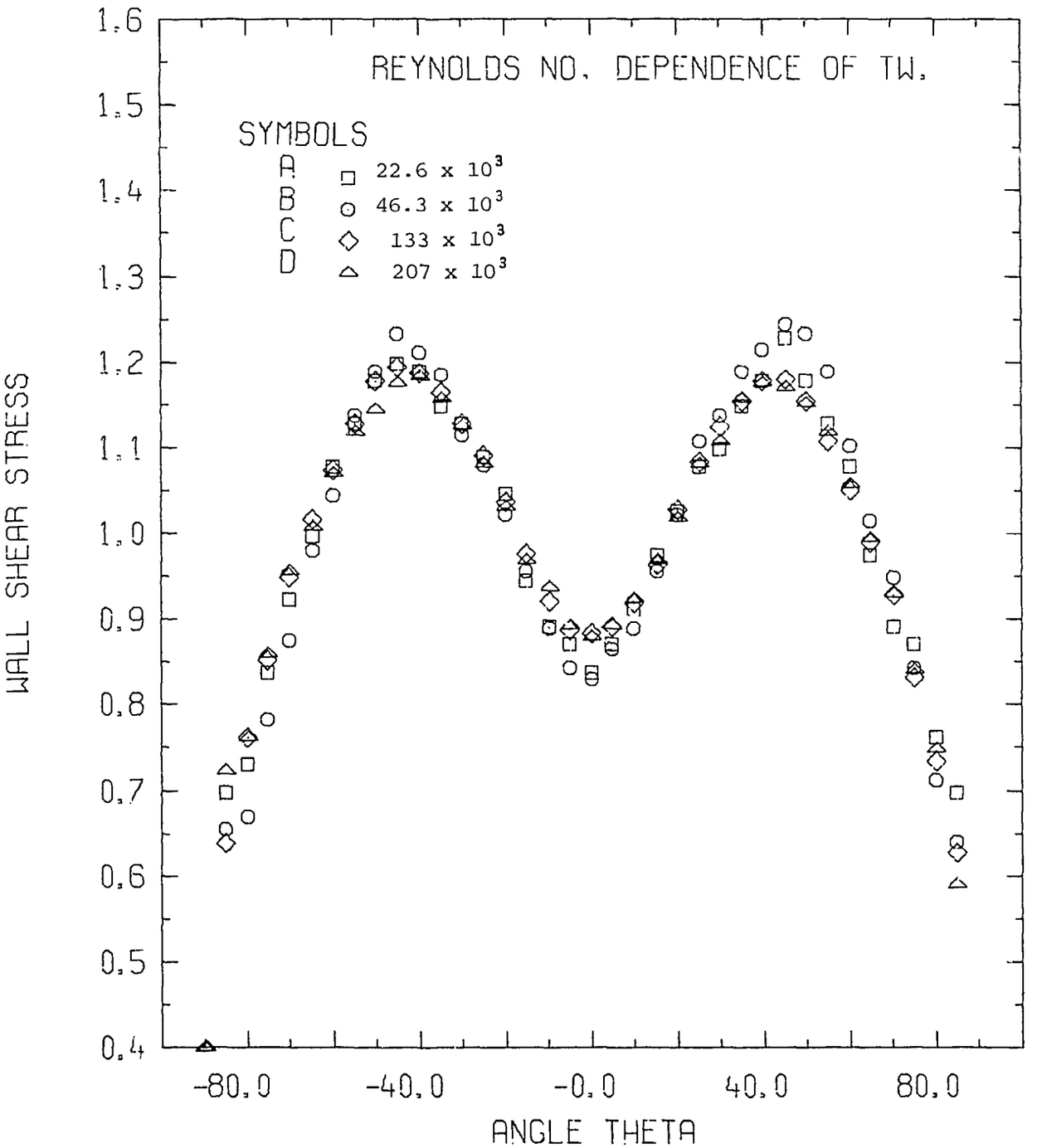

FIGURE 2a WALL SHEAR STRESS DISTRIBUTIONS, NORMALISED BY AVERAGE STRESS, FOR TOP CENTRE-LINE ROD OF THE ARRAY

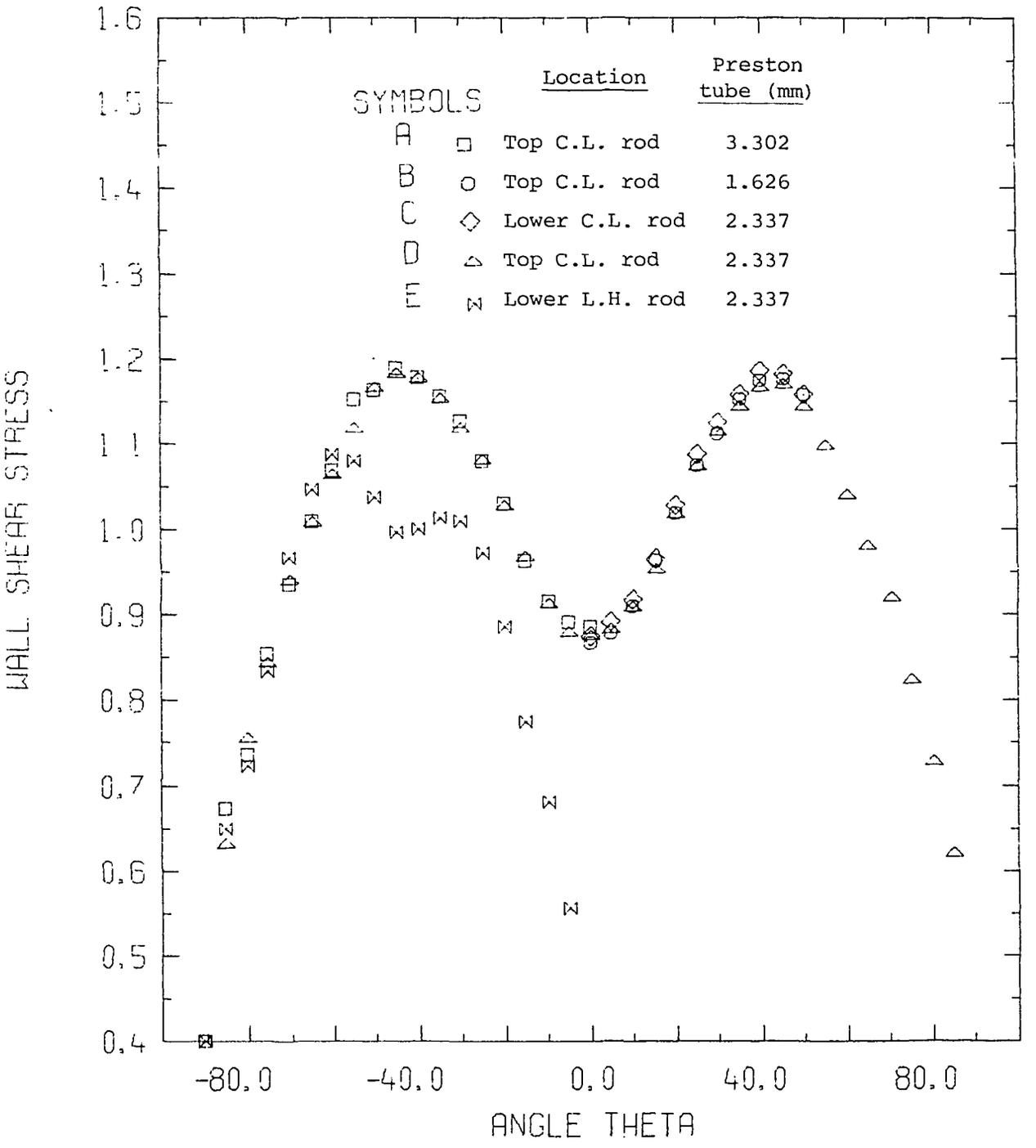

FIGURE 2b WALL SHEAR STRESS DISTRIBUTION.
Re = 133 × 10^3 ; p/d = 1.107

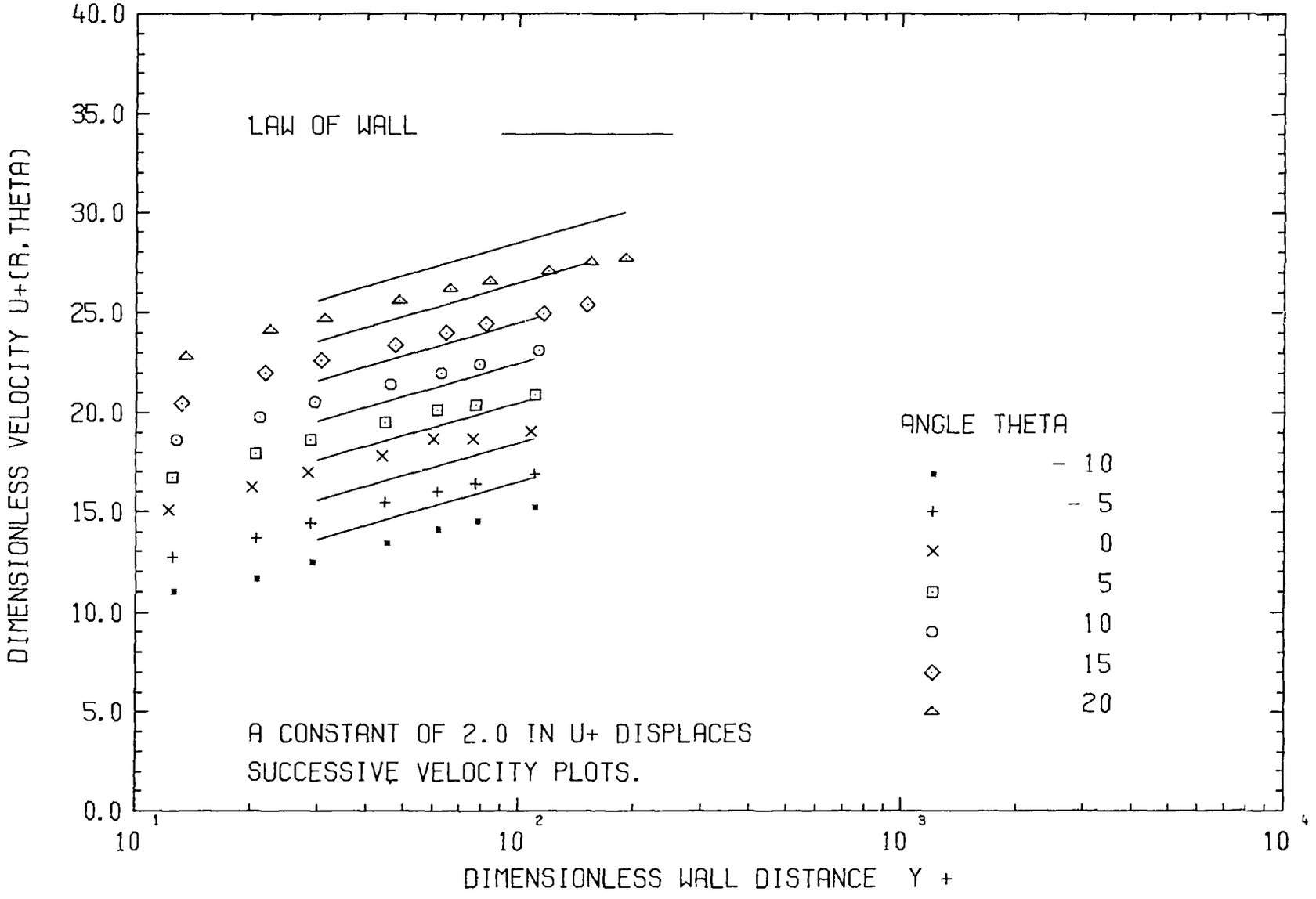

FIGURE 3a MEAN RADIAL VELOCITY PROFILES. RADIAL TRAVERSE AT -10° NOT DISPLACED BY CONSTANT. Re = 22.6 × 10^3

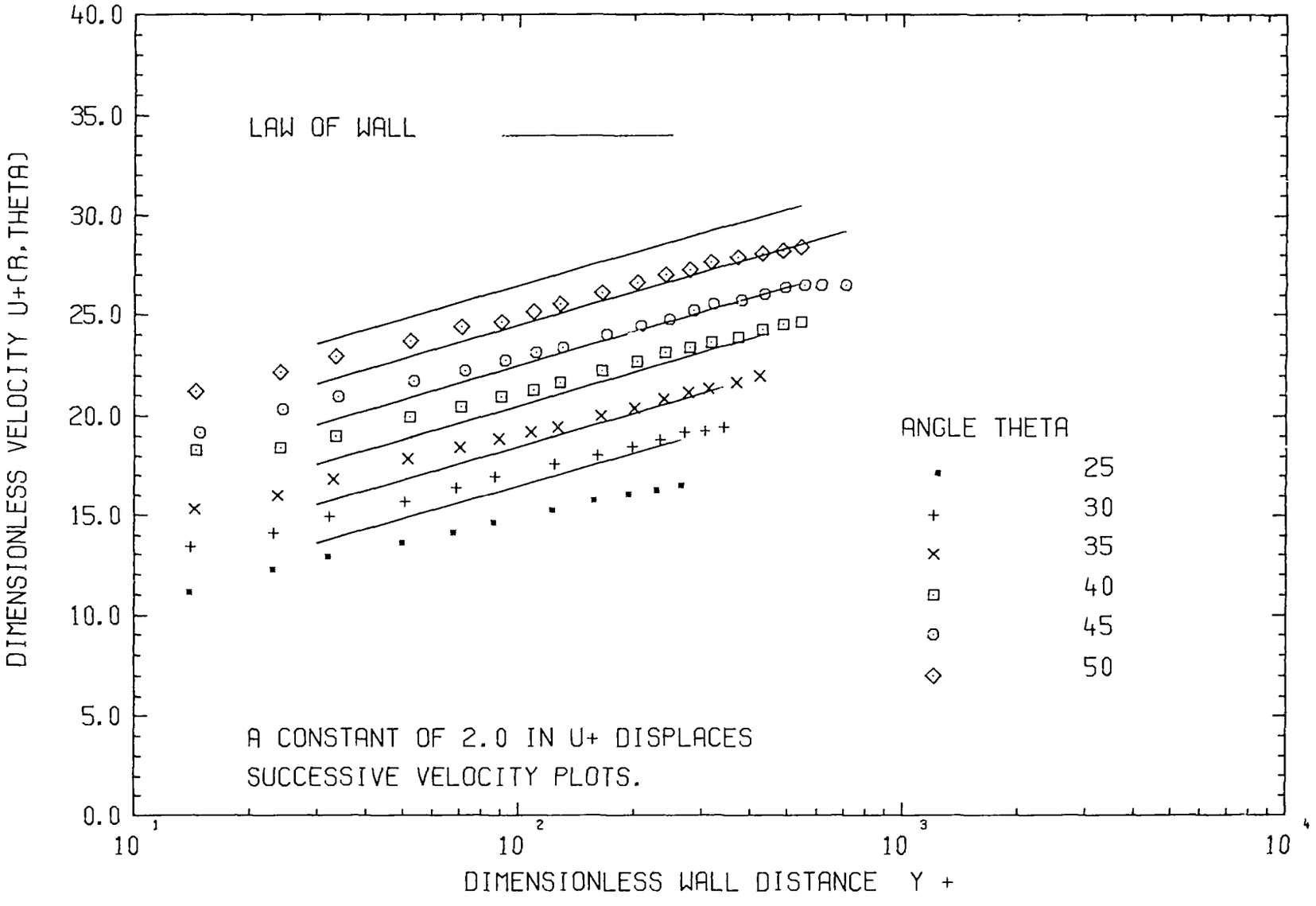

FIGURE 3b MEAN RADIAL VELOCITY PROFILES. RADIAL TRAVERSE AT 25° NOT DISPLACED BY CONSTANT. Re = 22.6×10^3

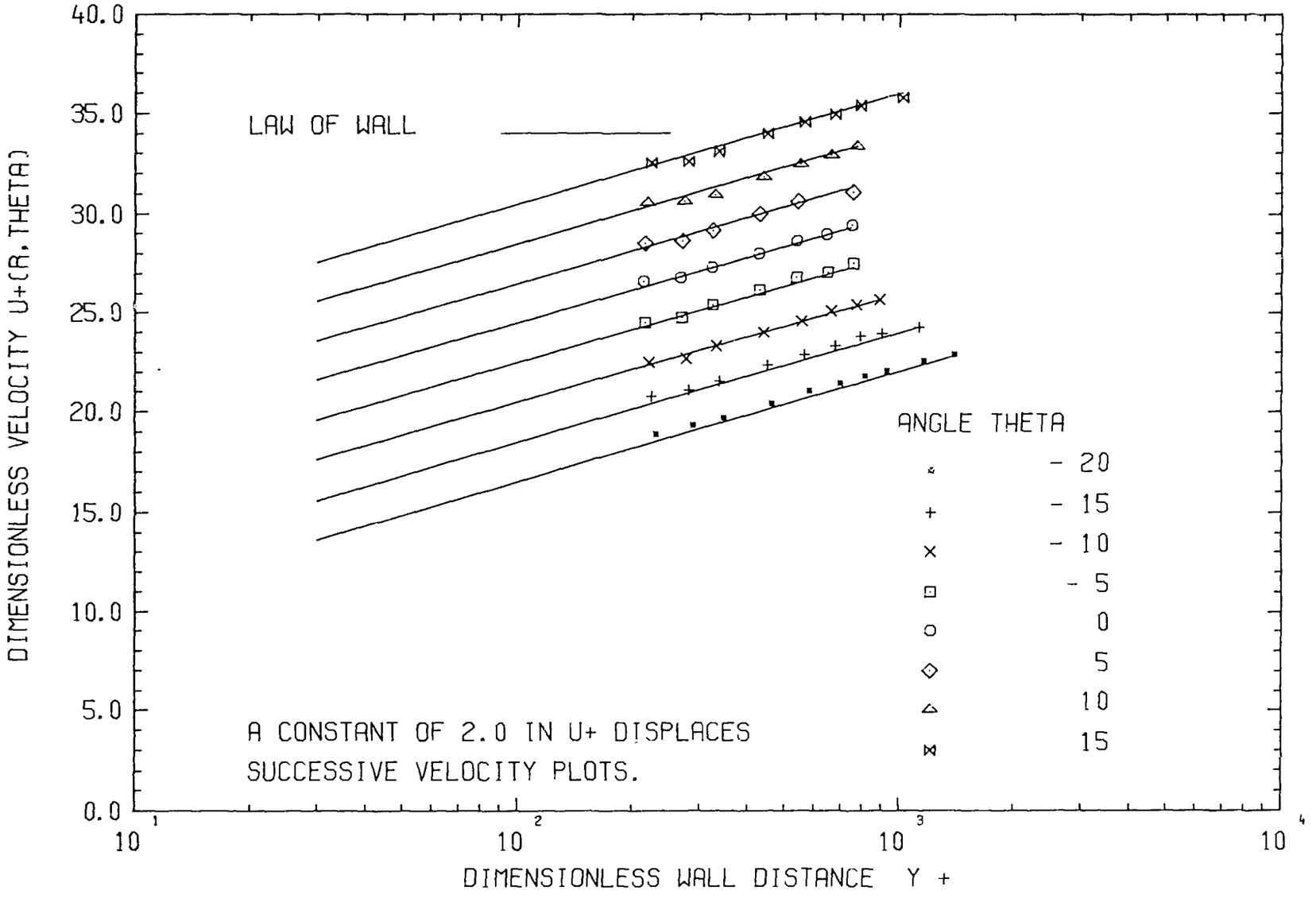

FIGURE 4a MEAN RADIAL VELOCITY PROFILES. RADIAL TRAVERSE AT -20° NOT DISPLACED BY CONSTANT. Re = 207.6 × 10^3

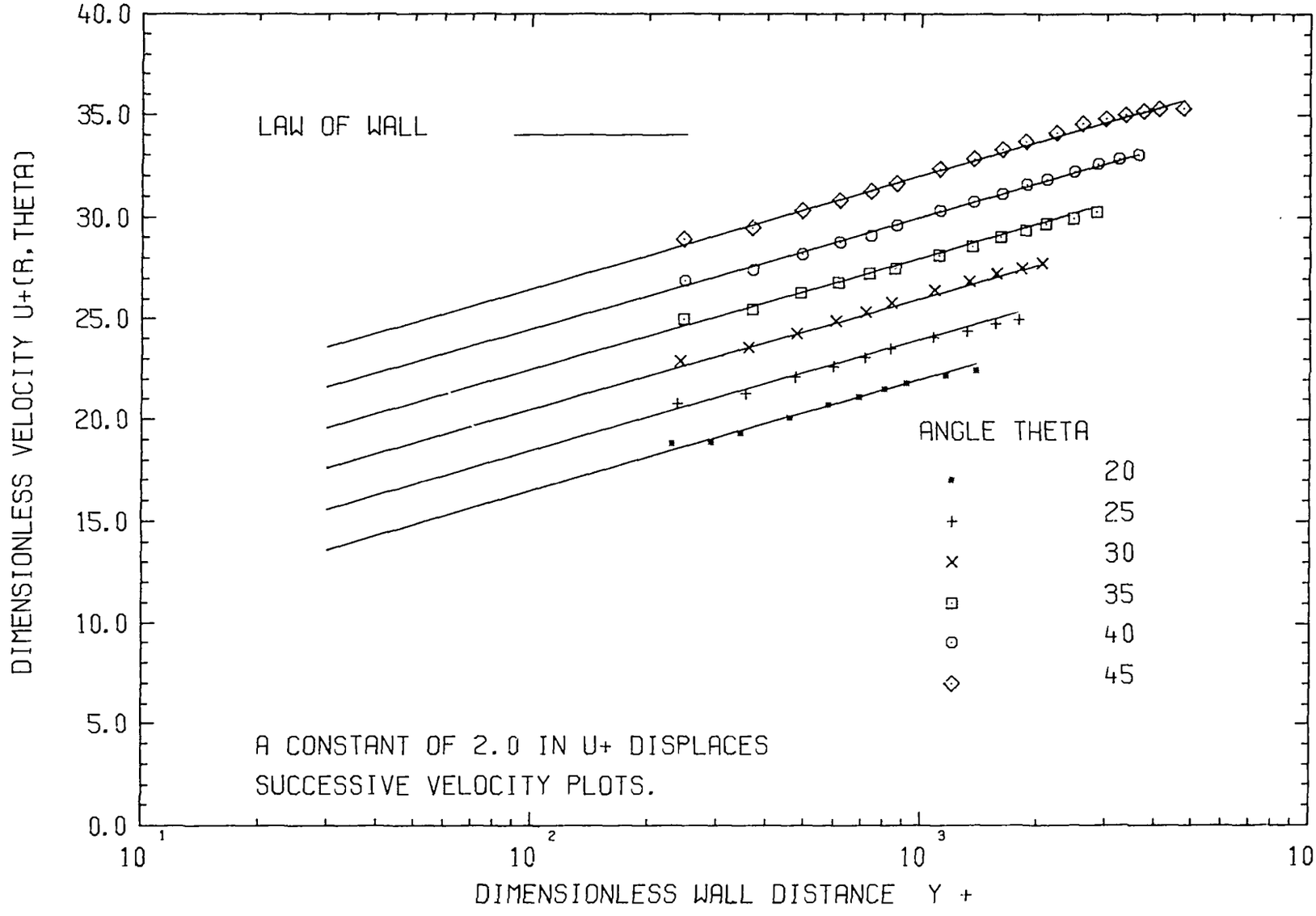

FIGURE 4b MEAN RADIAL VELOCITY PROFILES. RADIAL TRAVERSE AT 20° NOT DISPLACED BY CONSTANT. Re = 207.6 × 10 3

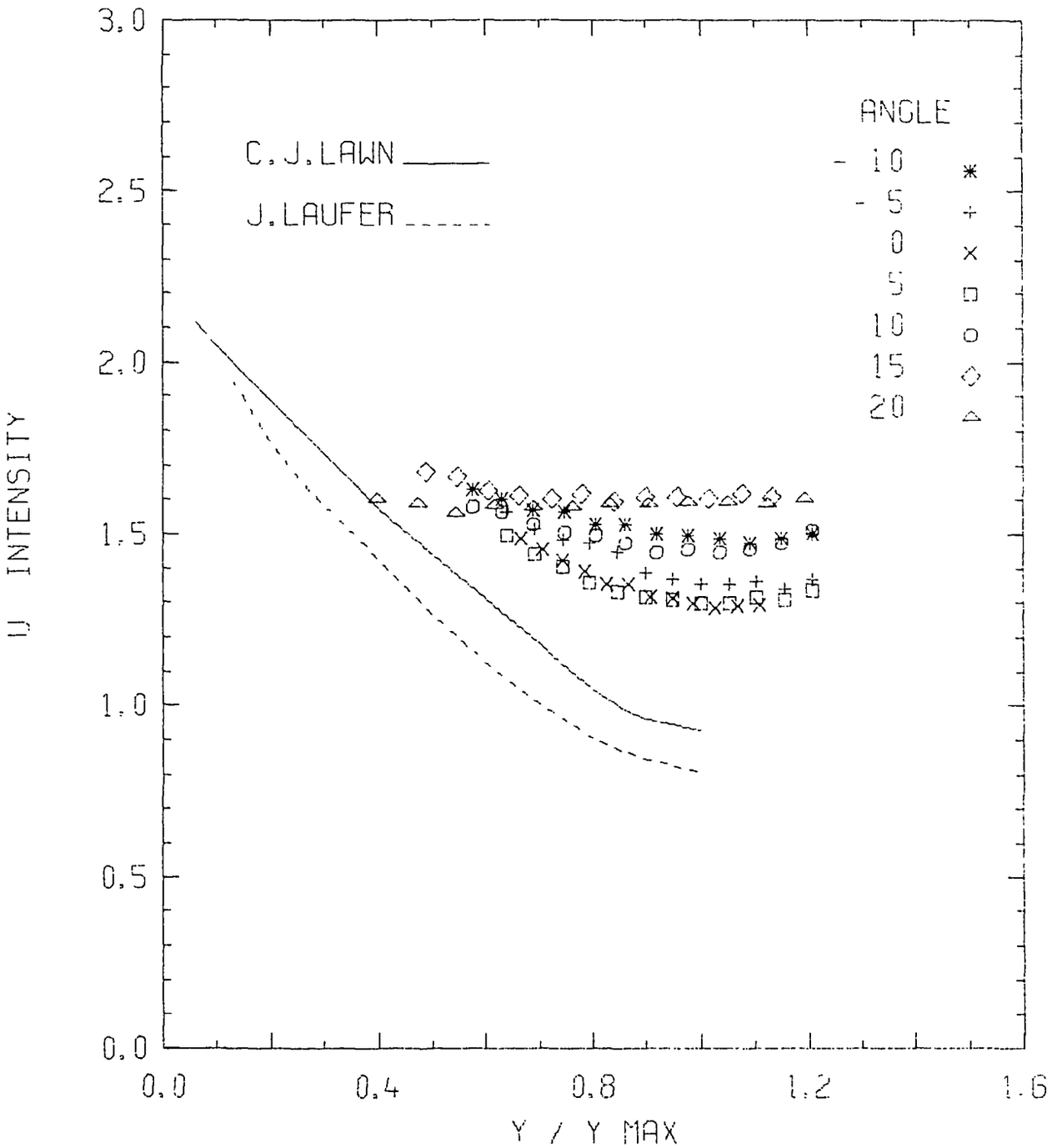

FIGURE 5a AXIAL TURBULENCE INTENSITY $u'/v^*(\theta)$.
$Re = 22.6 \times 10^3$, $p/d = 1.107$

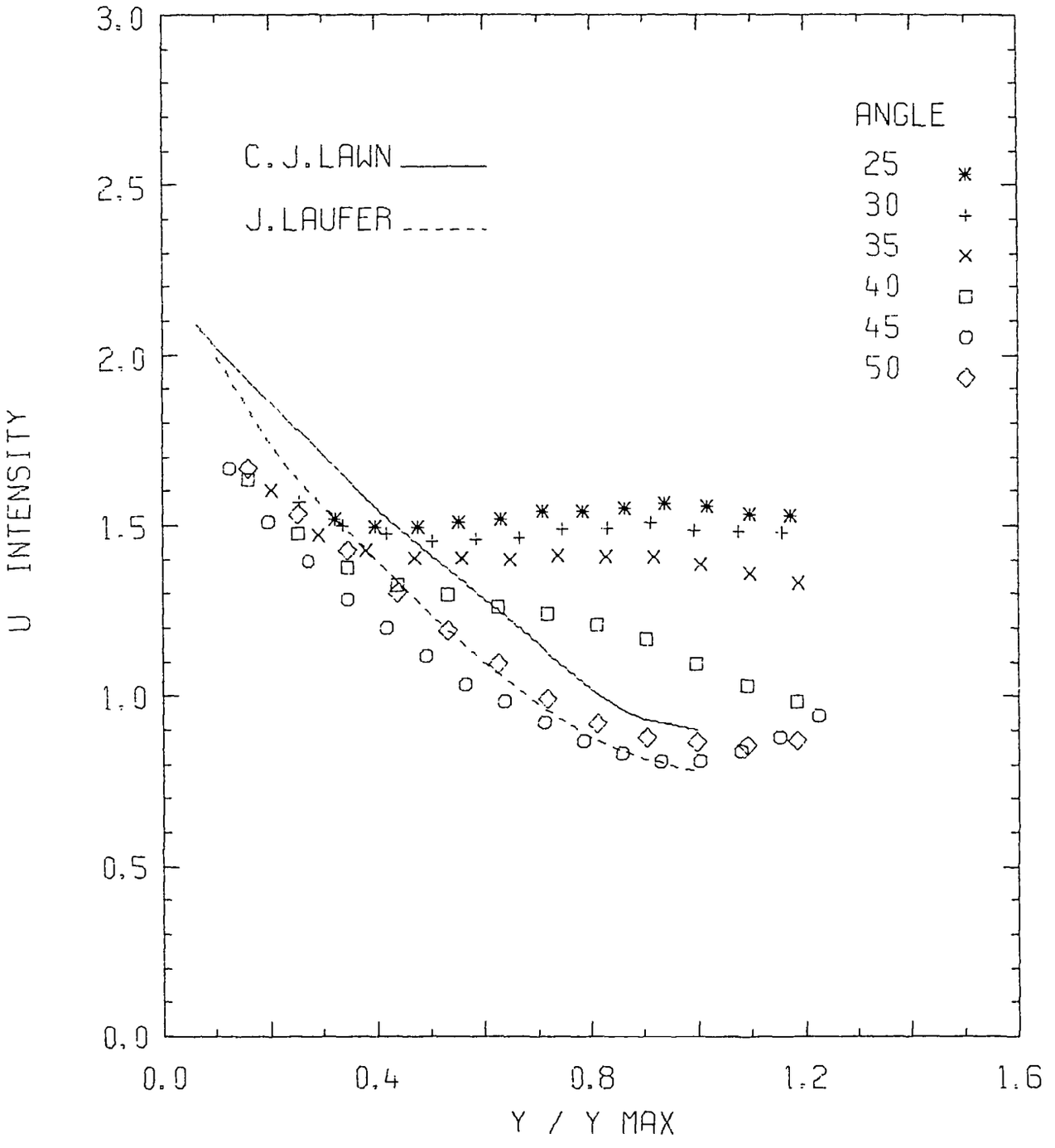

FIGURE 5b AXIAL TURBULENCE INTENSITY $u'/v^*(\theta)$.
Re = 22.6 × 10^3; p/d = 1.107

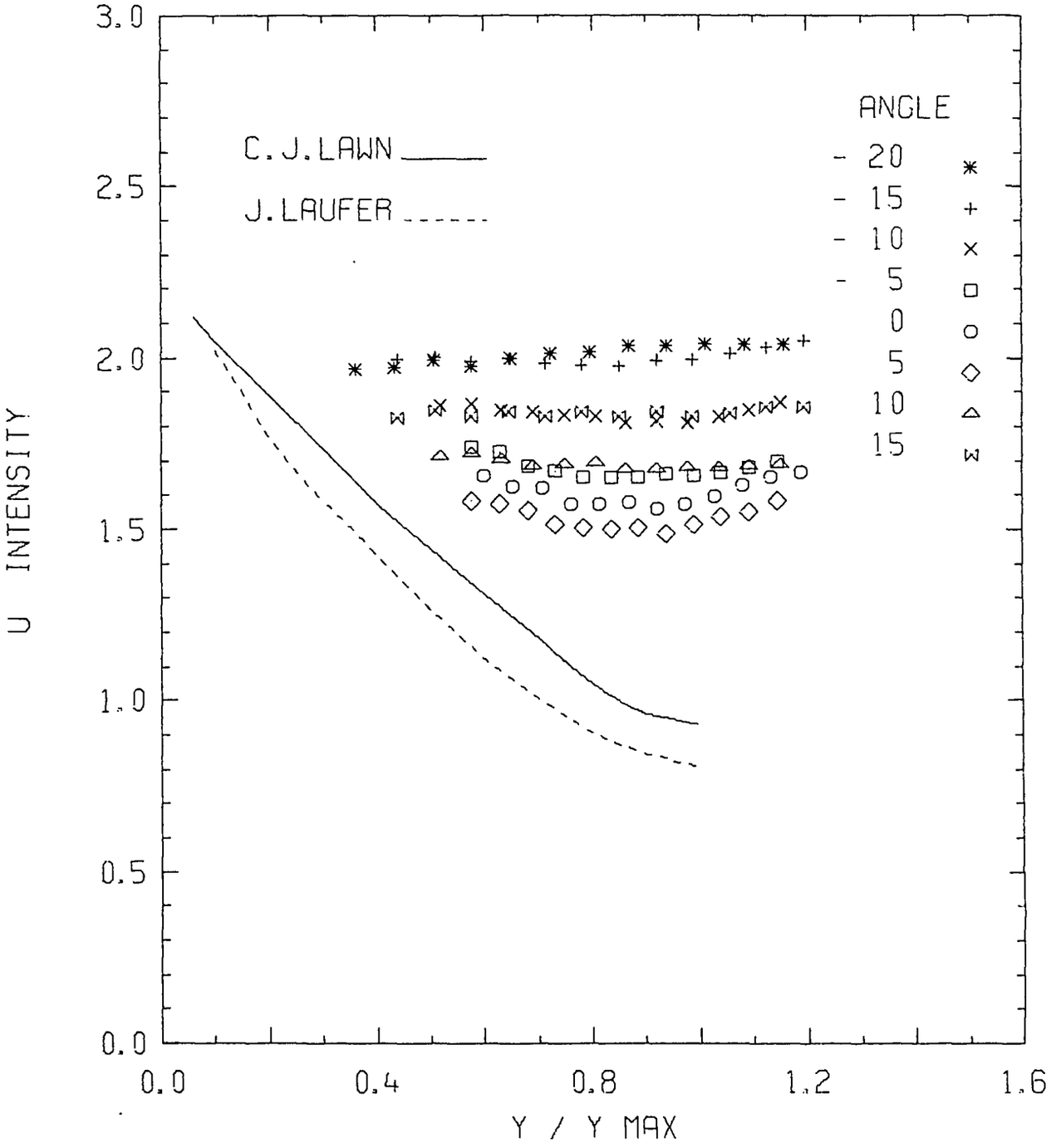

FIGURE 6a AXIAL TURBULENCE INTENSITY $u'/v^*(\theta)$.
Re = 207.6 × 10^3; p/d = 1.107

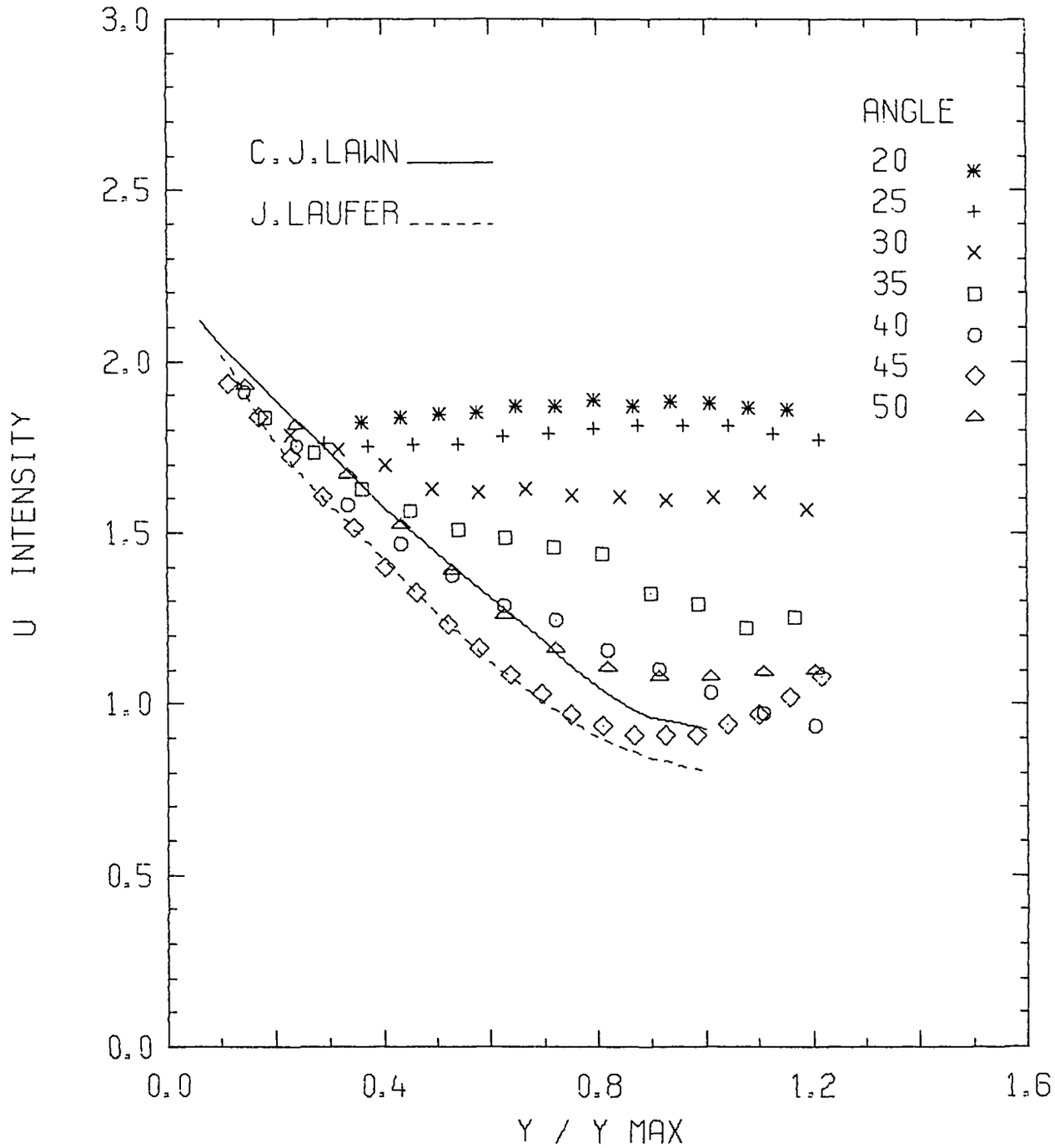

FIGURE 6b AXIAL TURBULENCE INTENSITY $u'/v^*(\theta)$.
Re = 207.6×10^3; p/d = 1.107

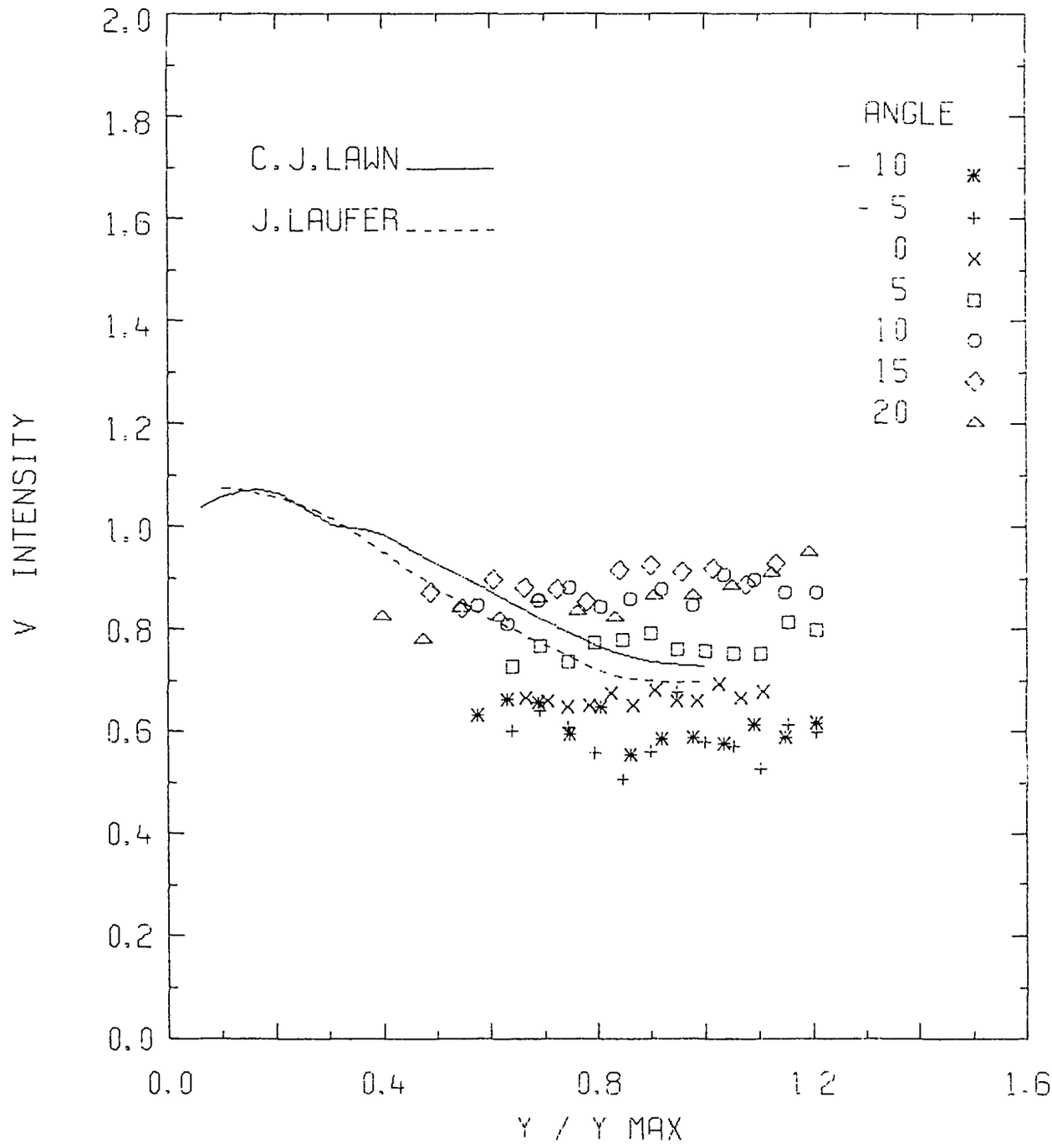

FIGURE 7a RADIAL TURBULENCE INTENSITY $v/v^*(\theta)$.
Re = 22.6 × 10^3; p/d = 1.107

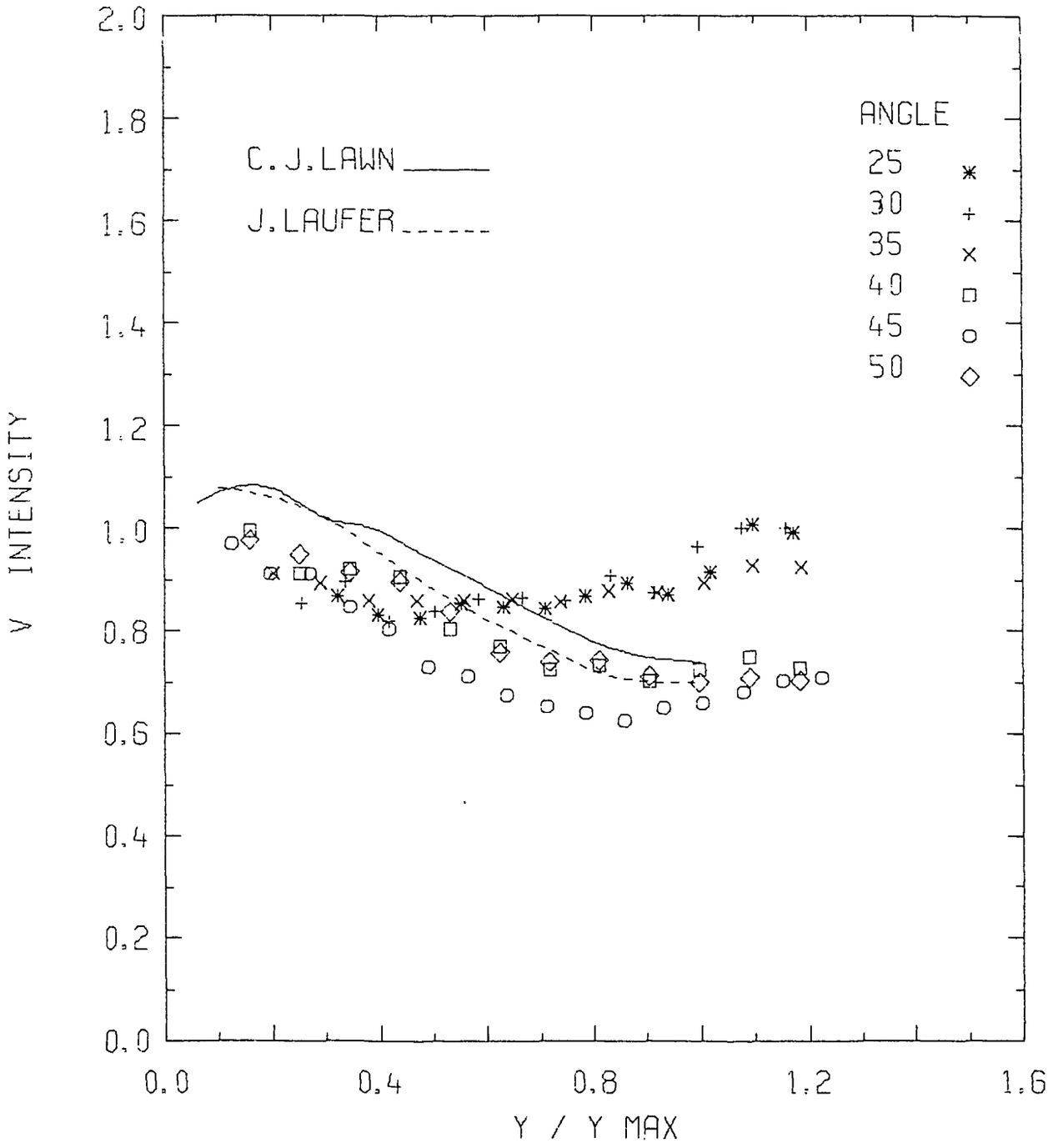

FIGURE 7b. RADIAL TURBULENCE INTENSITY $v/v^*(\theta)$.
Re = 22.6×10^3, p/d = 1.107

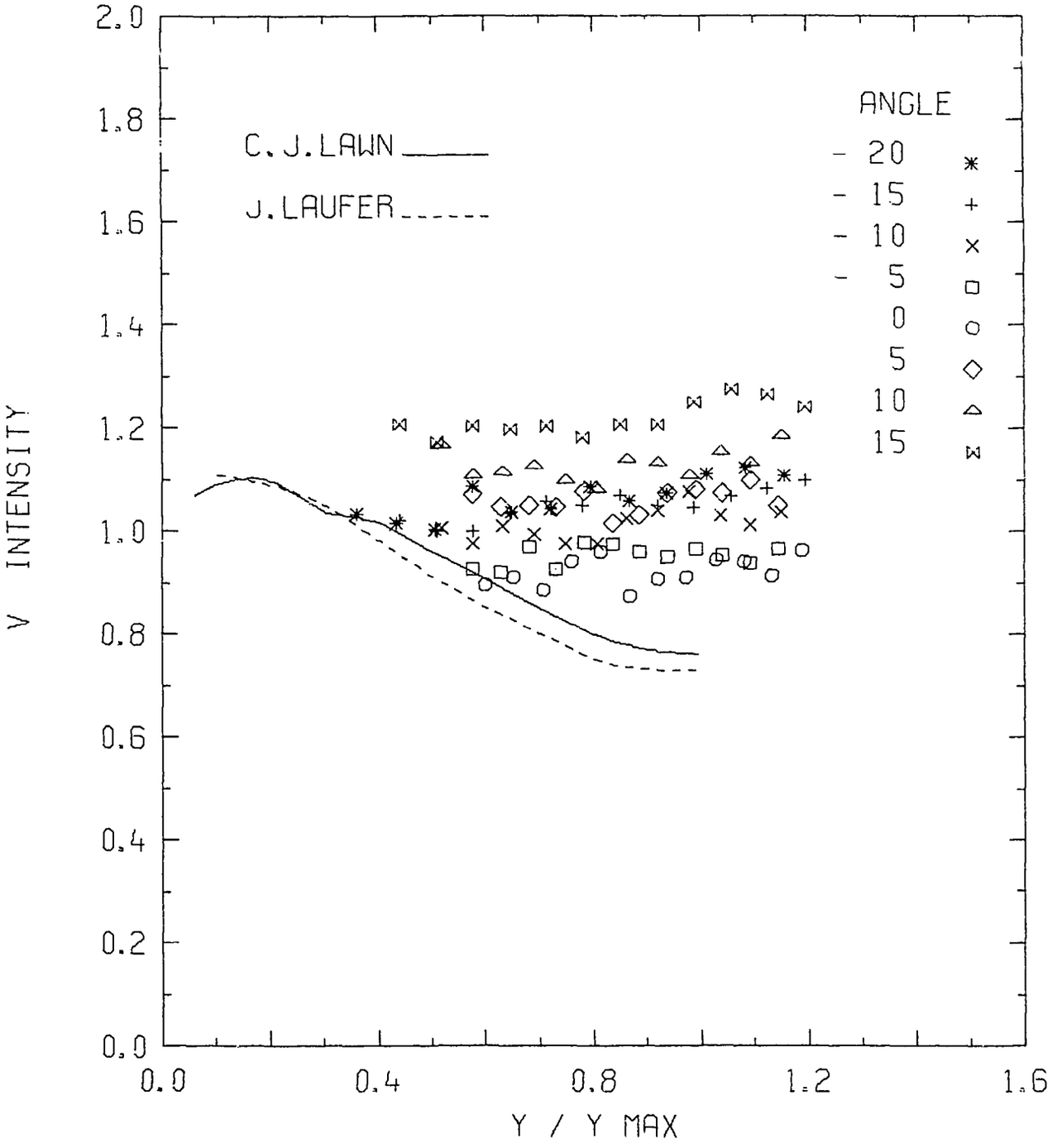

FIGURE 8a. RADIAL TURBULENCE INTENSITY $v/v^*(\theta)$.
Re = 207.6 × 10^3; p/d = 1.107

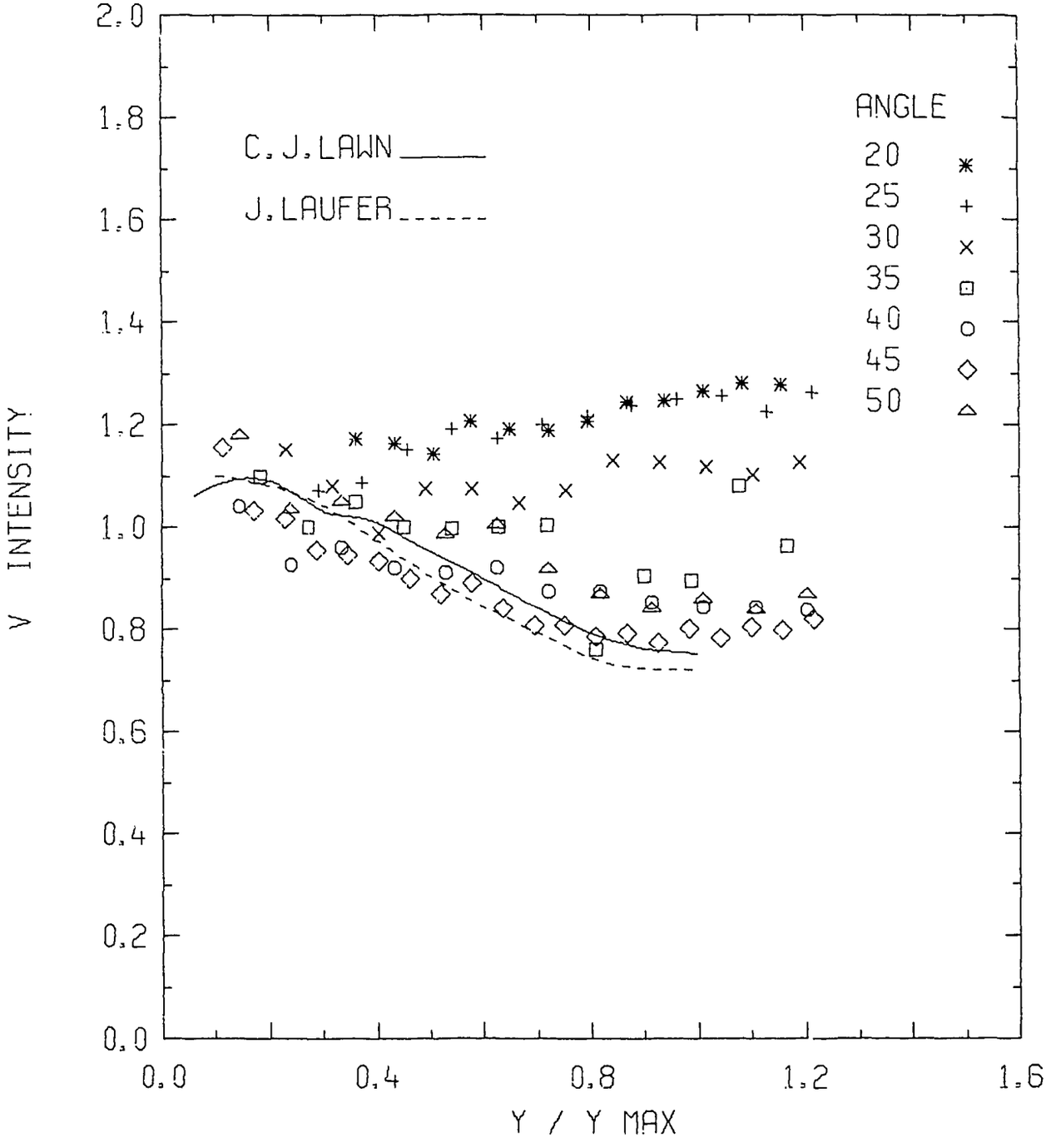

FIGURE 8b RADIAL TURBULENCE INTENSITY $v/v^*(\theta)$.
Re = 207.6×10^3; p/d = 1.107

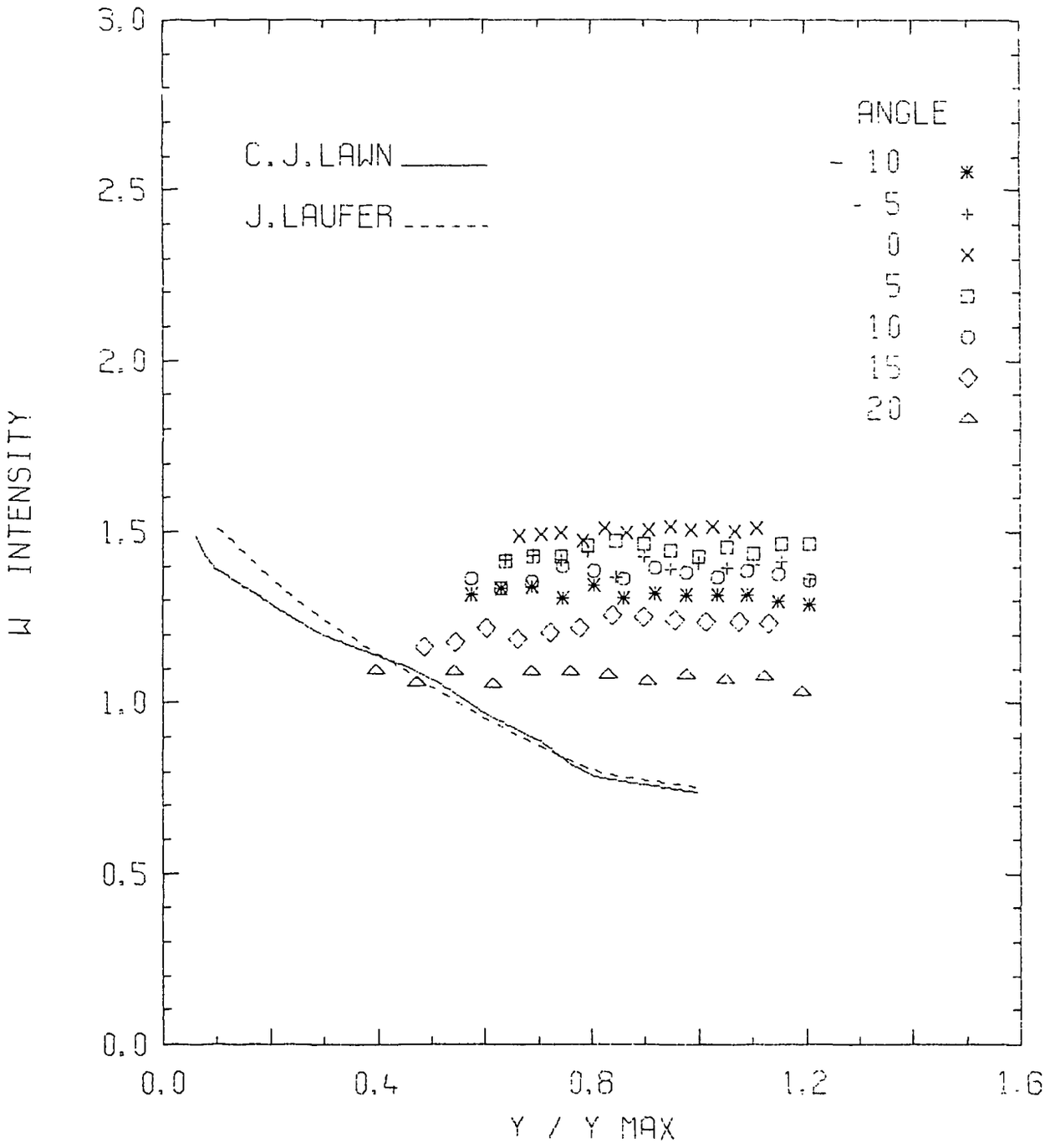

FIGURE 9a. AZIMUTHAL TURBULENCE INTENSITY $w/v^*(\theta)$.
Re = 22.6×10^3; p/d = 1.107

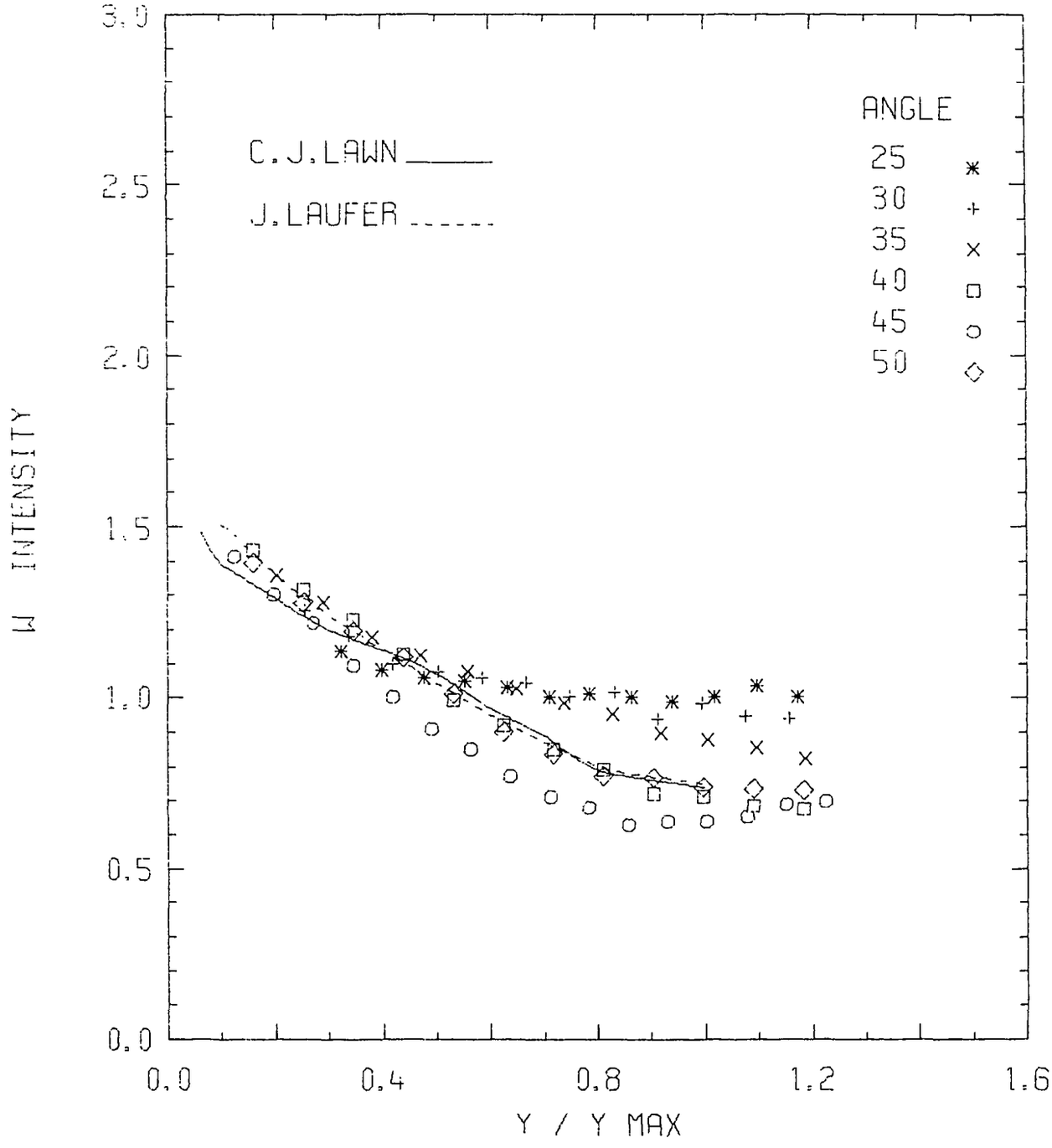

FIGURE 9b AZIMUTHAL TURBULENCE INTENSITY $w/v^*(\theta)$.
$Re = 22.6 \times 10^3$; $p/d = 1.107$

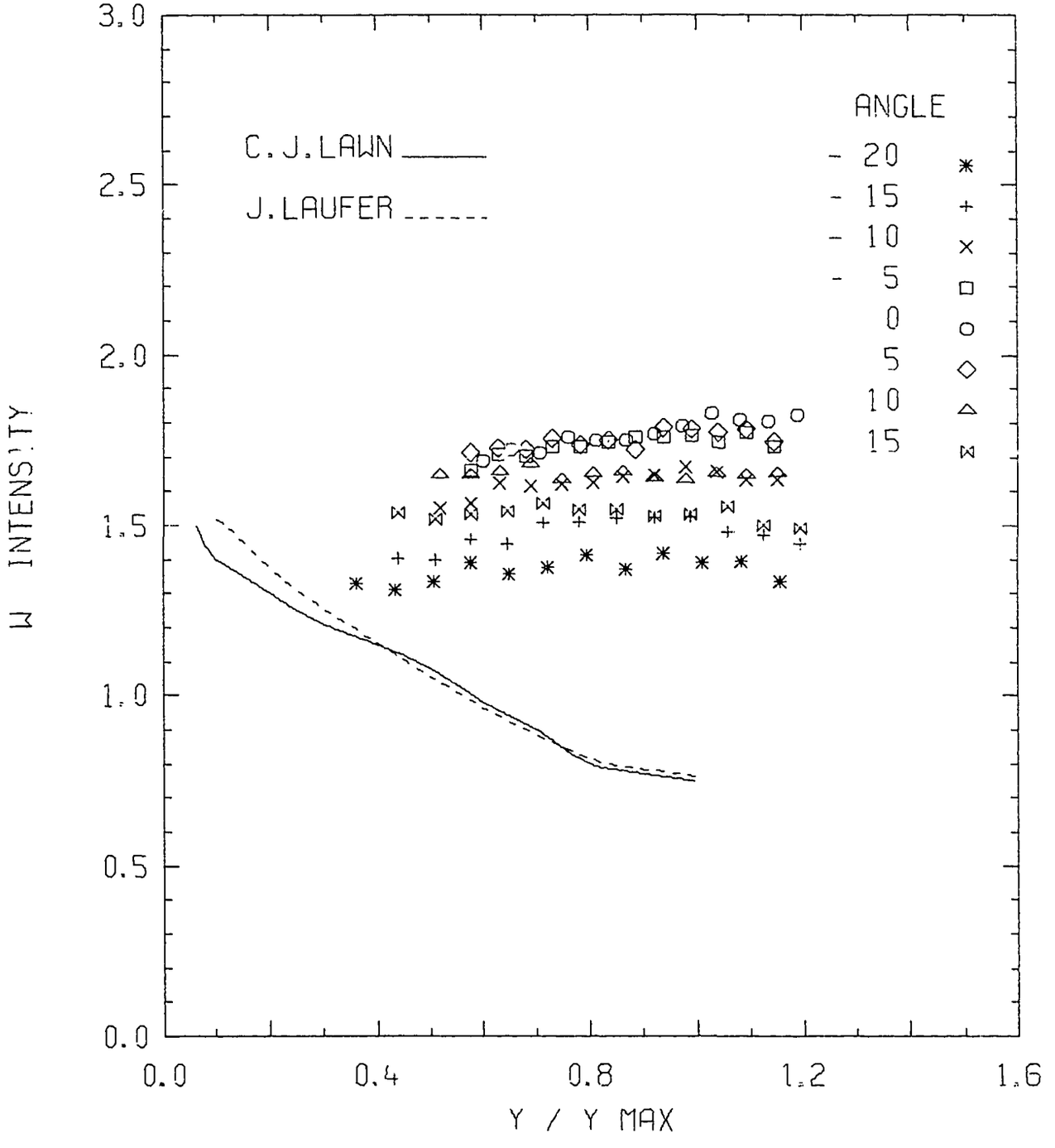

FIGURE 10a AZIMUTHAL TURBULENCE INTENSITY $w/v^*(\theta)$.
$Re = 207.6 \times 10^3$; $p/d = 1.107$

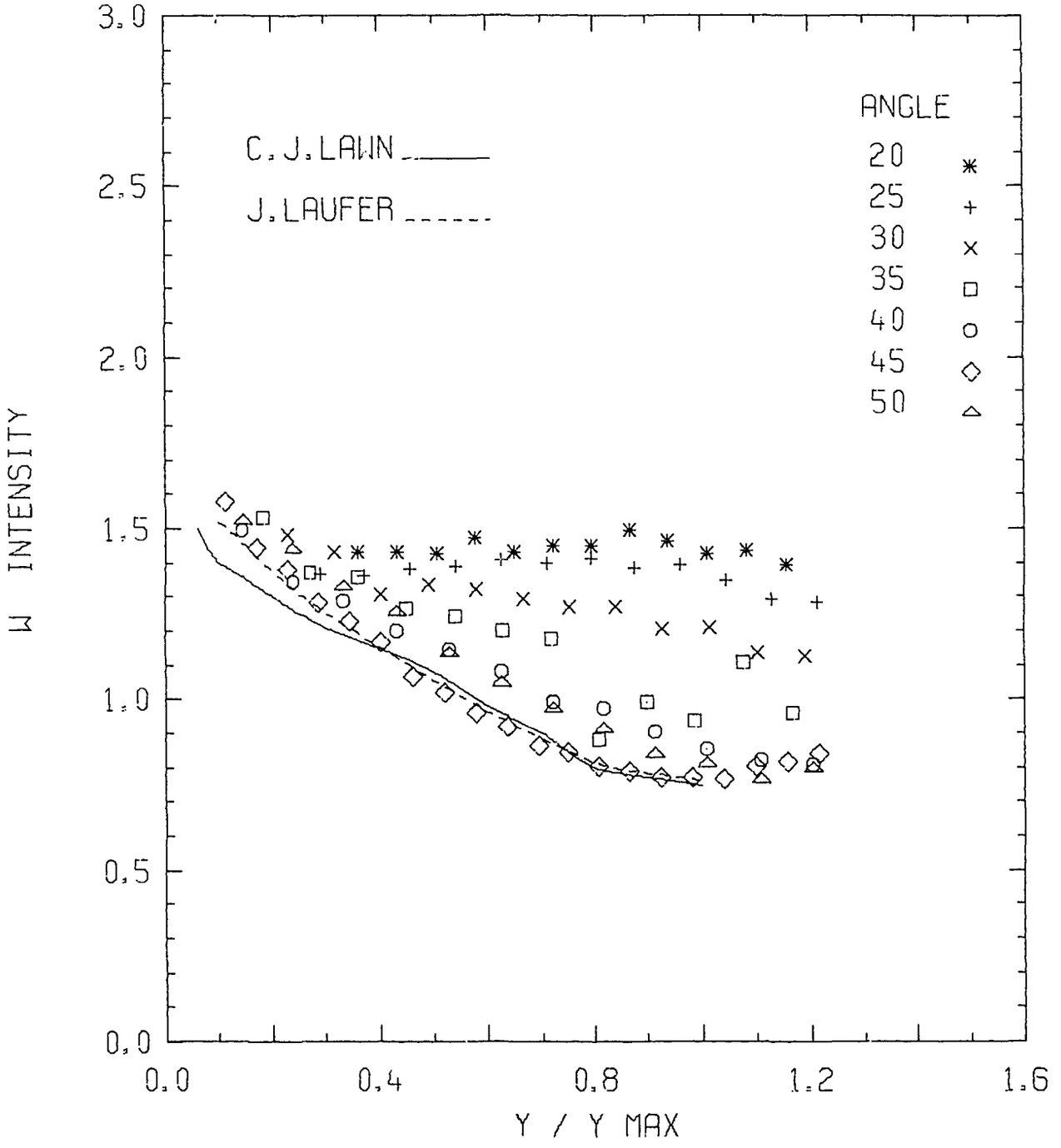

FIGURE 10b. AZIMUTHAL TURBULENCE INTENSITY $w/v^*(\theta)$.
$Re = 207.6 \times 10^3$; p/d = 1.107

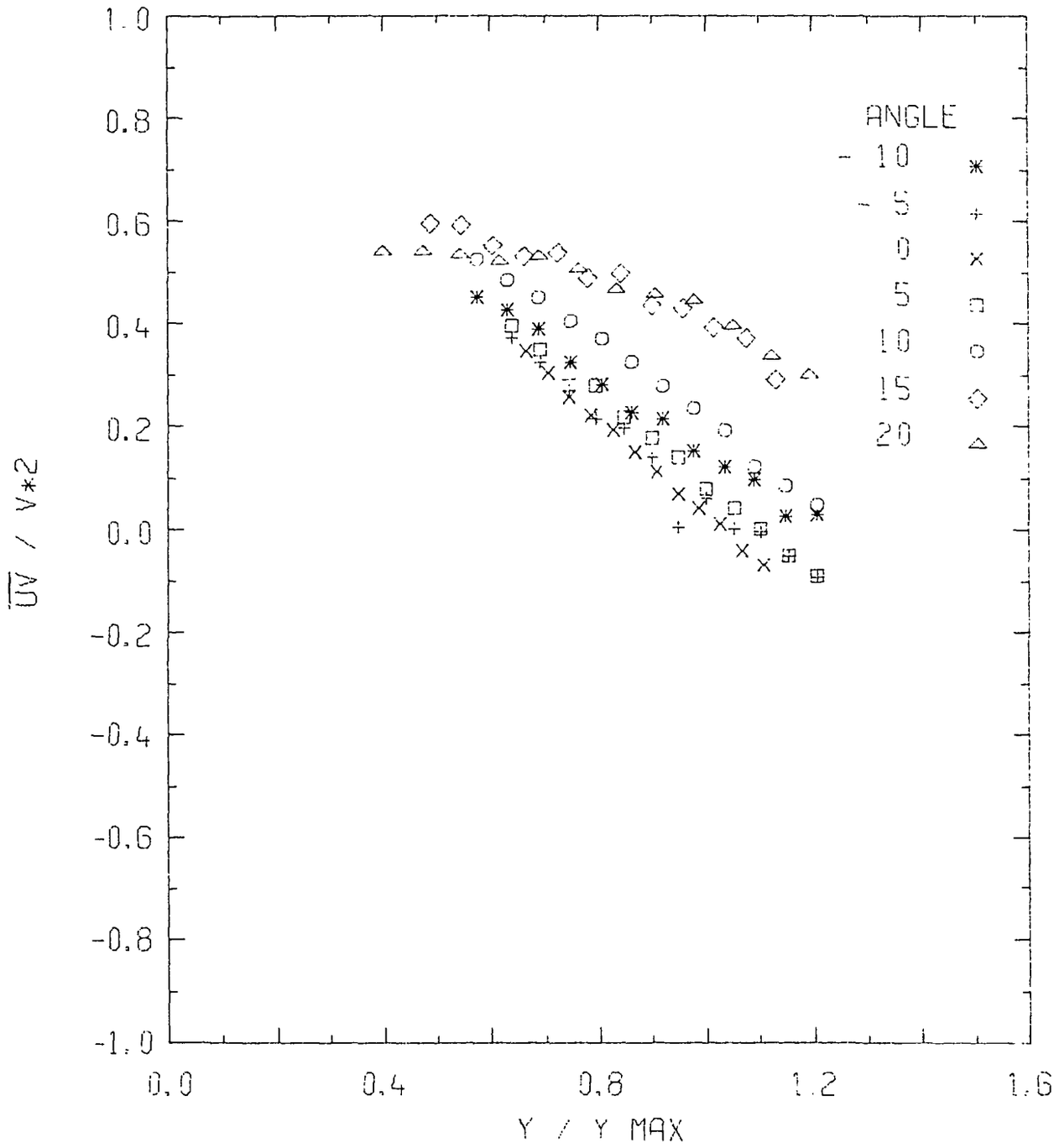

FIGURE 11a RADIAL TURBULENT SHEAR STRESS $\overline{uv}/v^{*2}(\theta)$.
Re = 22.6 × 10^3; p/d = 1.107

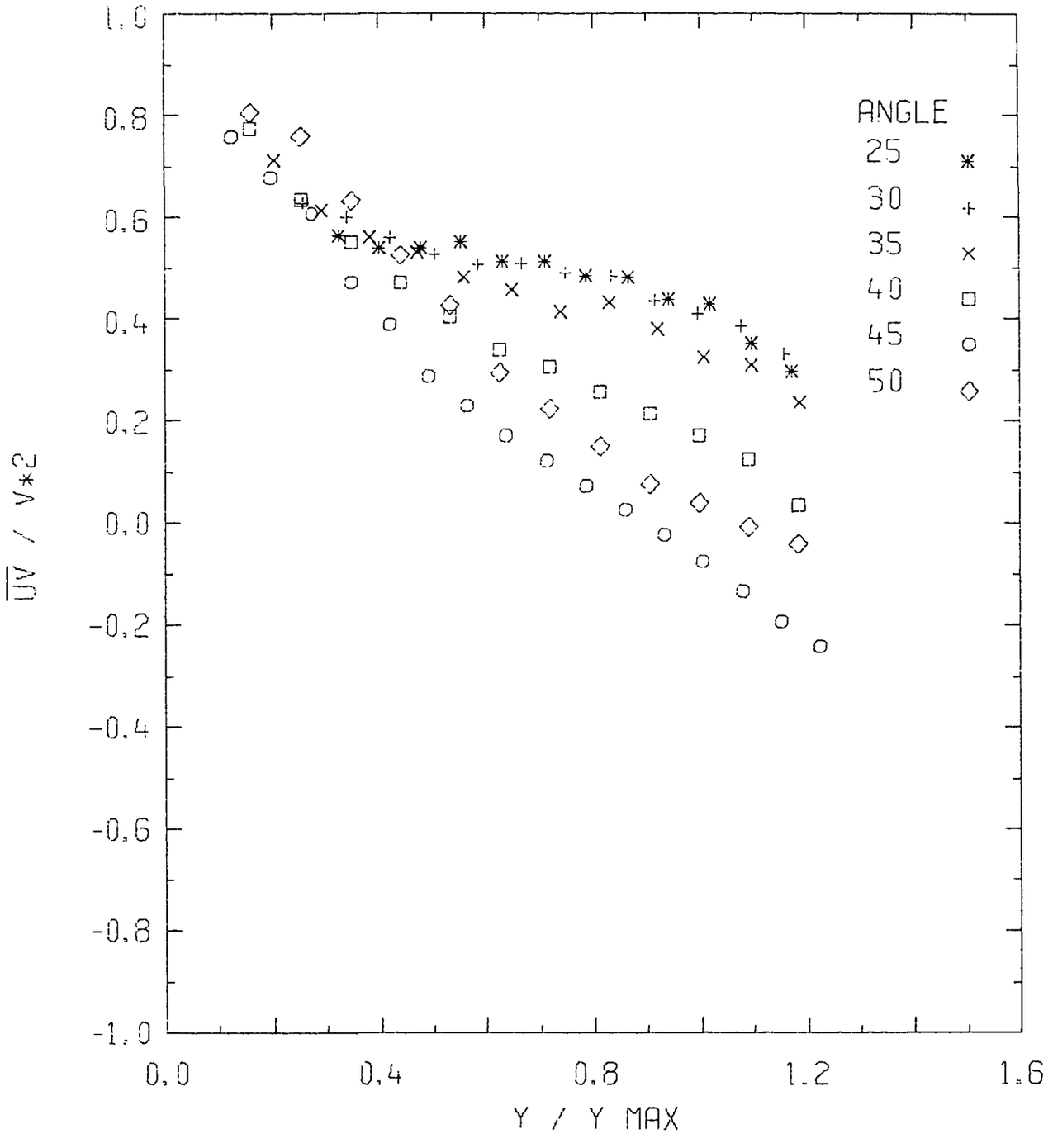

FIGURE 11b. RADIAL TURBULENT SHEAR STRESS $\overline{uv}/v^{*2}(\theta)$.
Re = 22.6 × 10^3; p/d = 1.107

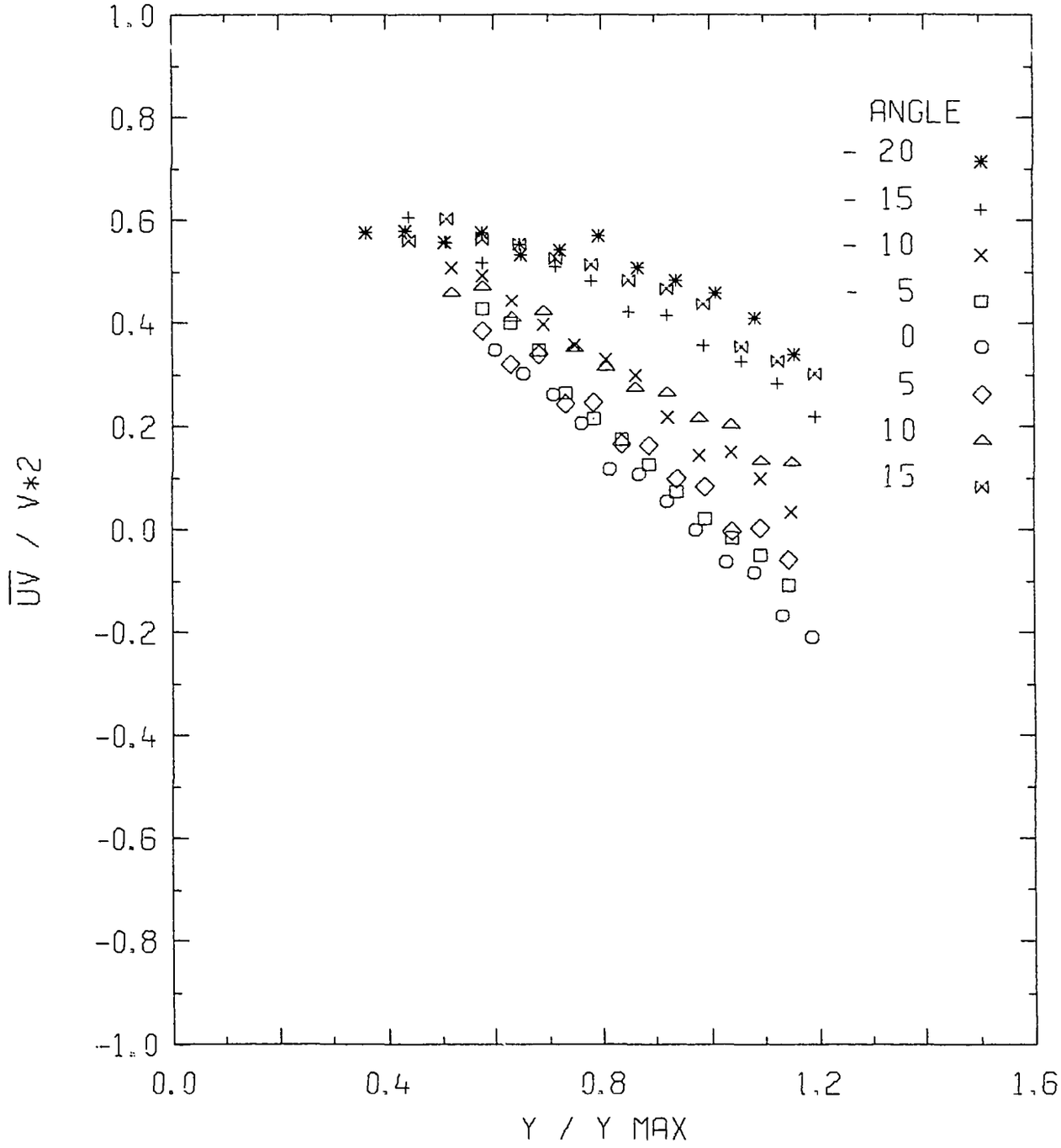

FIGURE 12a RADIAL TURBULENT SHEAR STRESS $\overline{uv}/v^{*2}(\theta)$.
Re = 207.6 × 10^3; p/d = 1.107

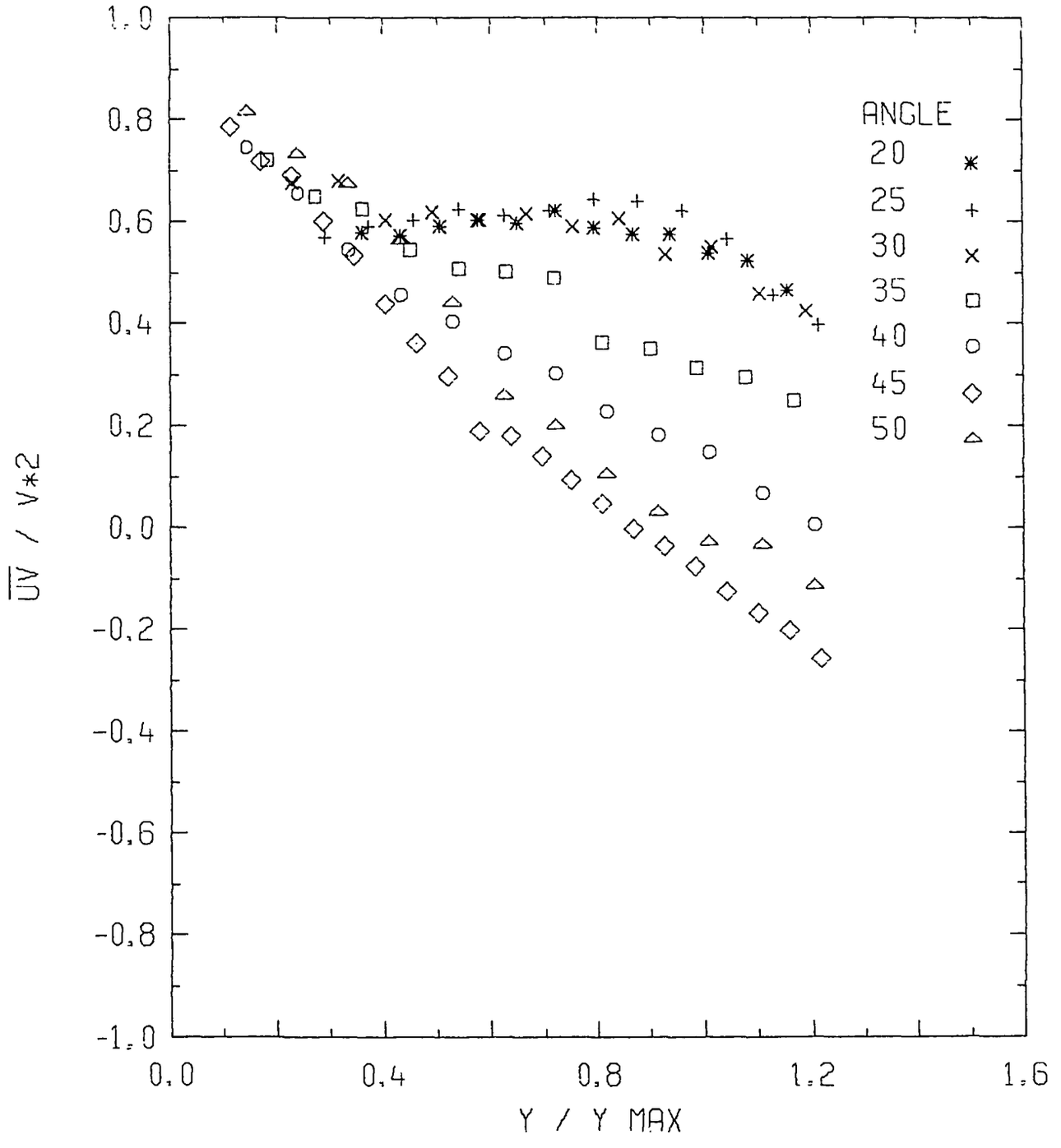

FIGURE 12b RADIAL TURBULENT SHEAR STRESS $\overline{uv}/v^{*2}(\theta)$.
Re = 207.6 × 10^3; p/d = 1.107

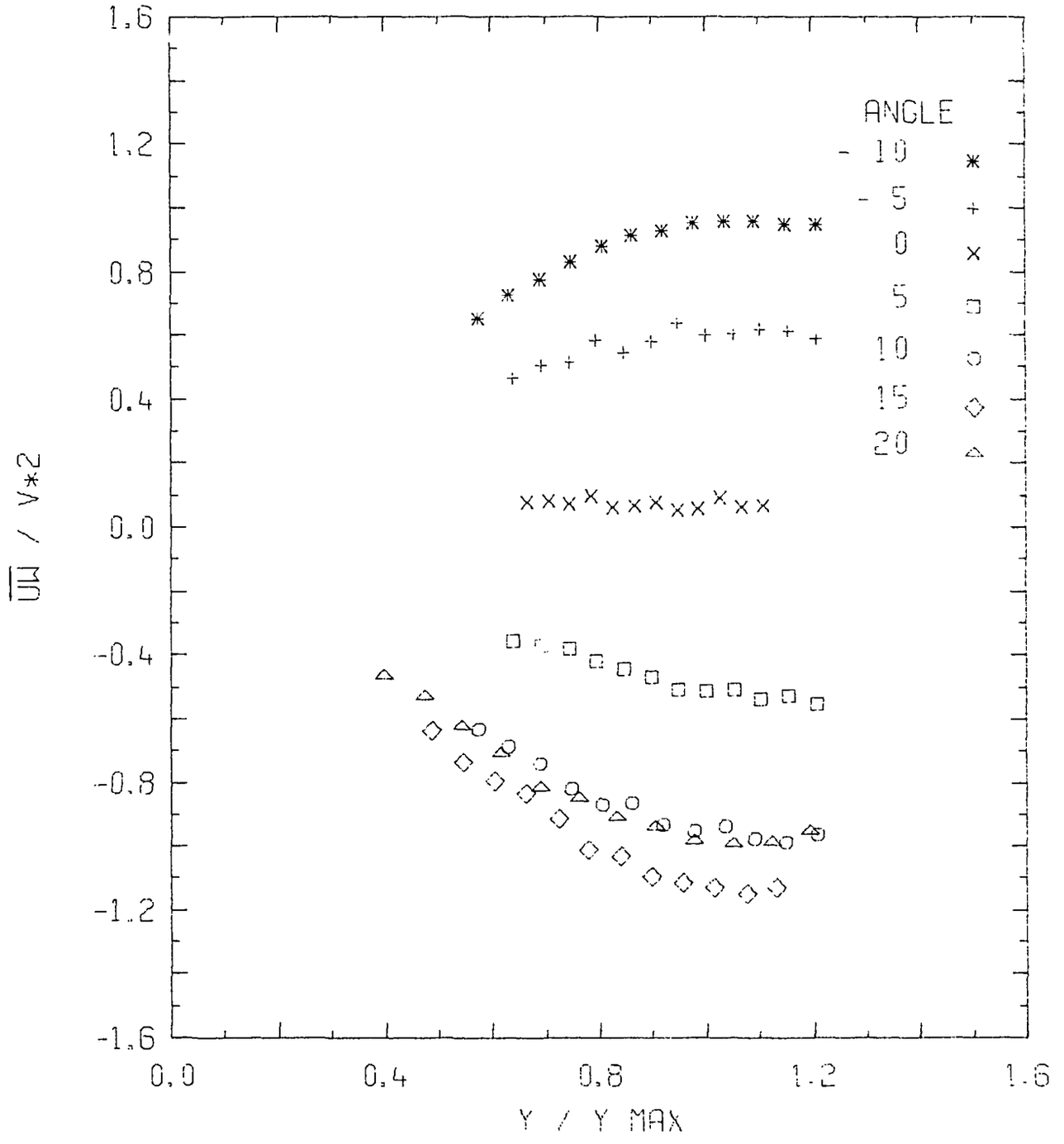

FIGURE 13a AZIMUTHAL TURBULENT SHEAR STRESS $\overline{uw}/v^{*2}(\theta)$.
Re = 22.6 × 10^3; p/d = 1.107

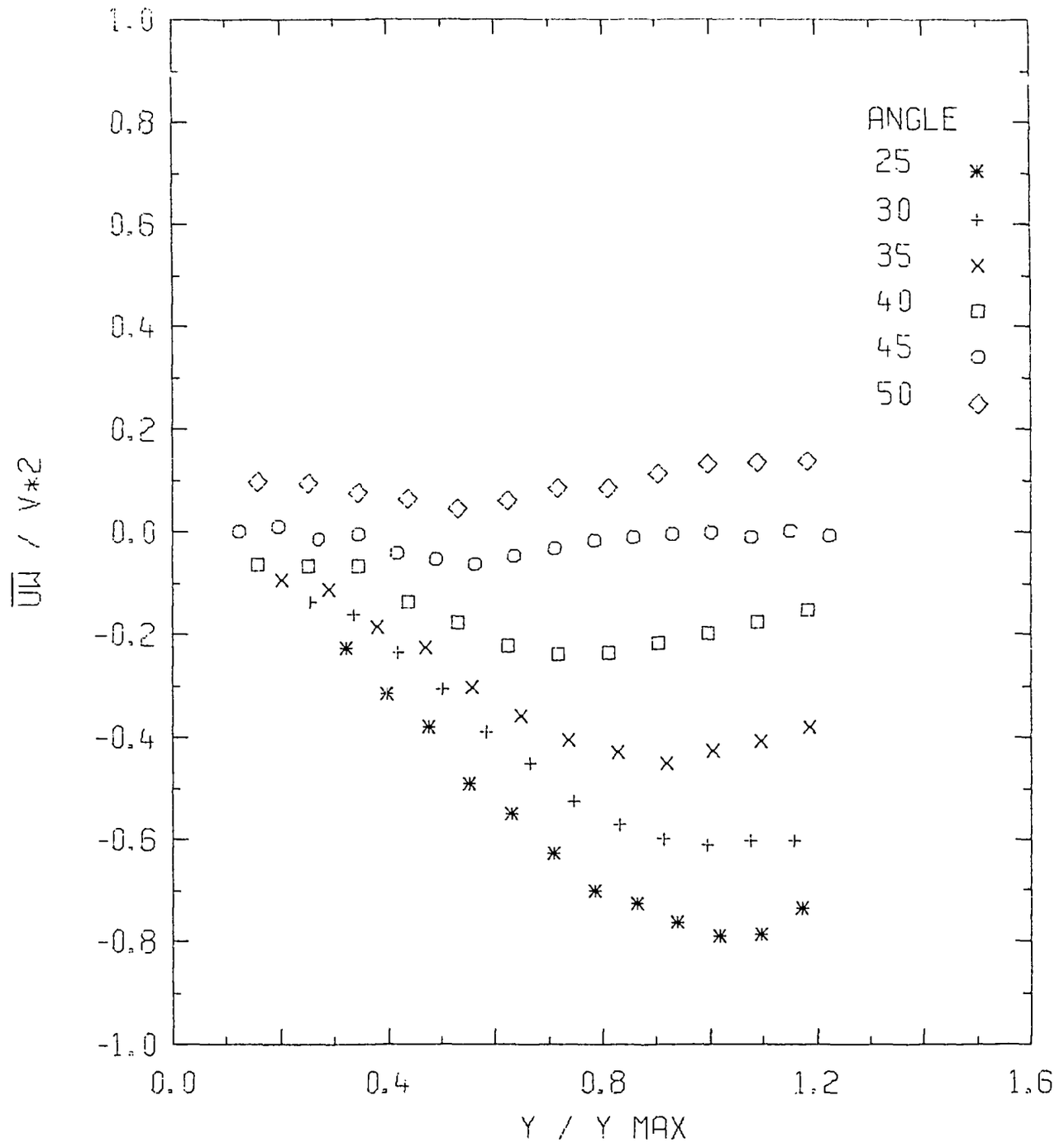

FIGURE 13b AZIMUTHAL TURBULENT SHEAR STRESS $\overline{uw}/v^{*2}(\theta)$.
Re = 22.6 × 10^3; p/d = 1.107

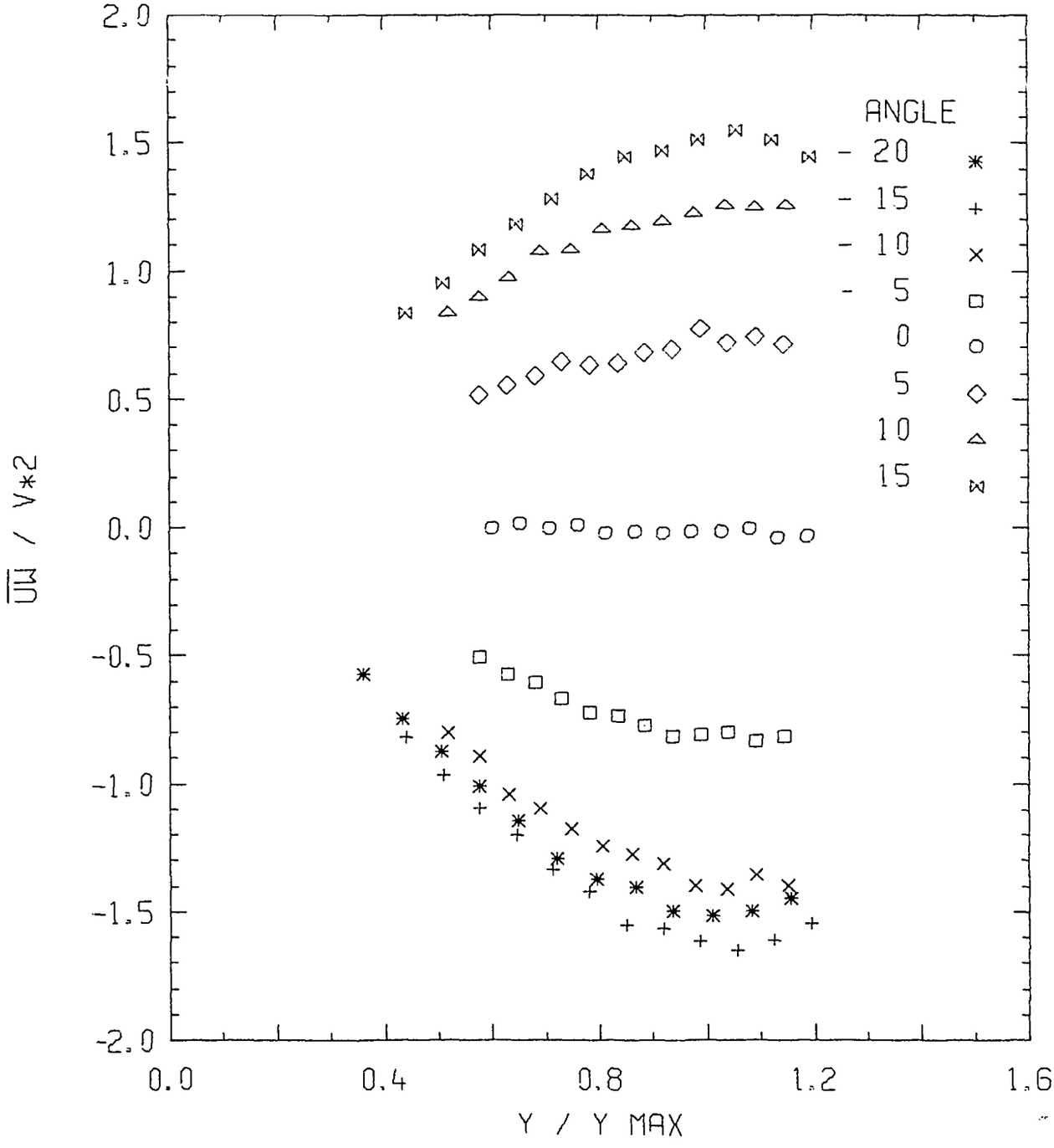

FIGURE 14a AZIMUTHAL TURBULENT SHEAR STRESS $\overline{uw}/v^{*2}(\theta)$.
Re = 207.6 × 10^3; p/d = 1.107

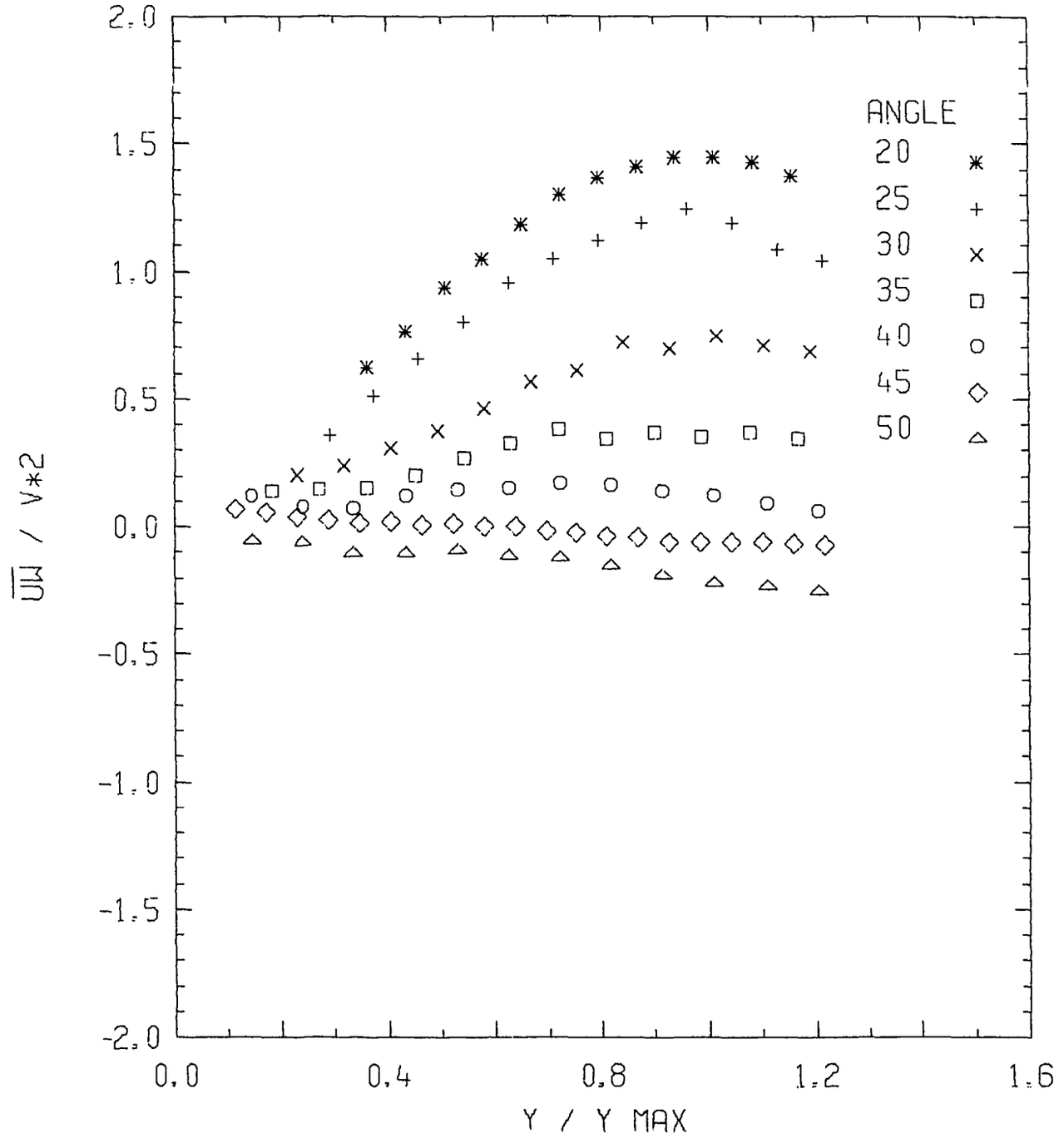

FIGURE 14b. AZIMUTHAL TURBULENT SHEAR STRESS $\overline{uw}/v^{*2}(\theta)$.
Re = 207.6 × 10^3; p/d = 1.107

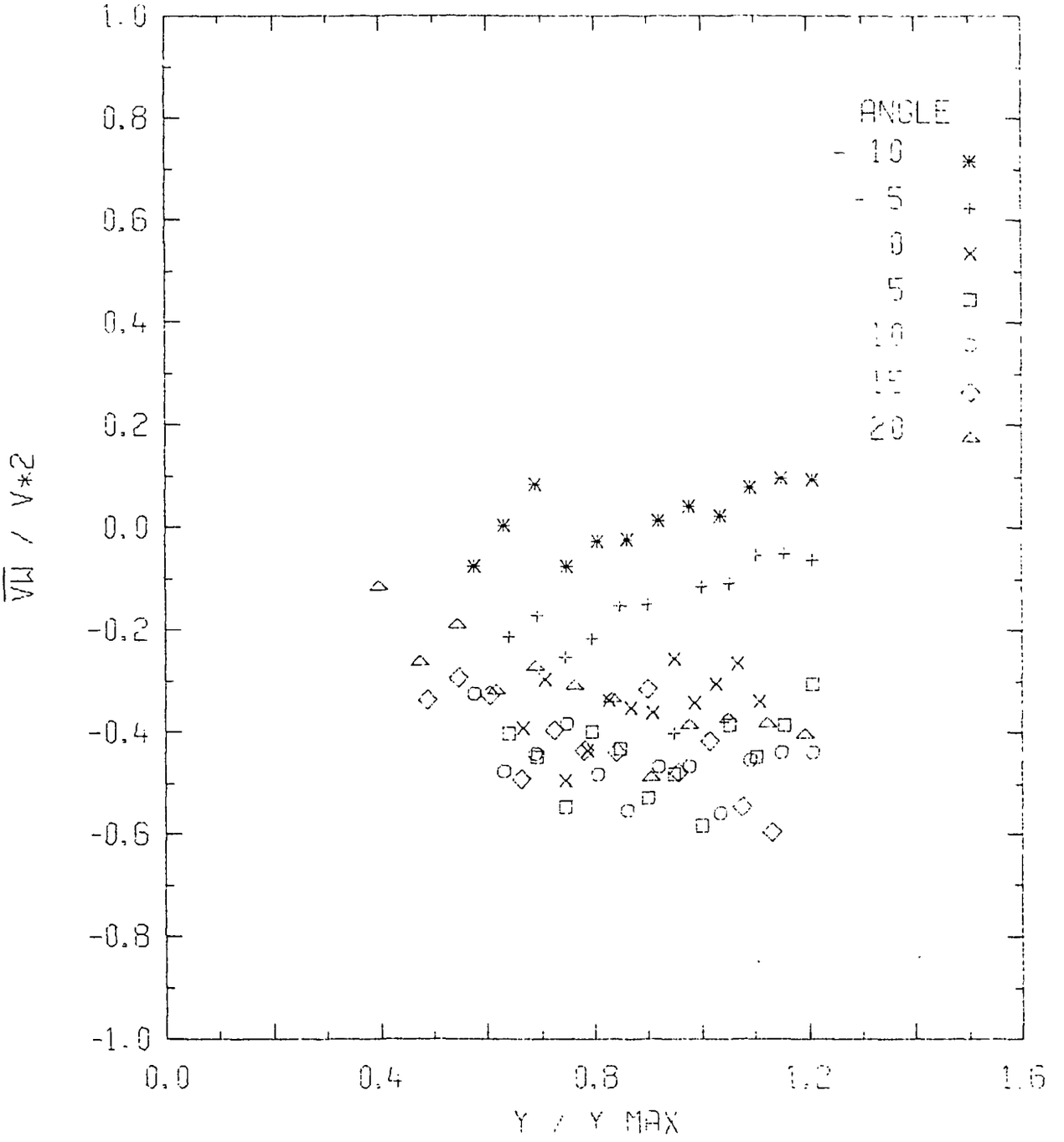

FIGURE 15a TRANSVERSE TURBULENT SHEAR STRESS $\overline{vw}/v^{*2}(\theta)$.
Re = 22.6 × 10^3; p/d = 1.107

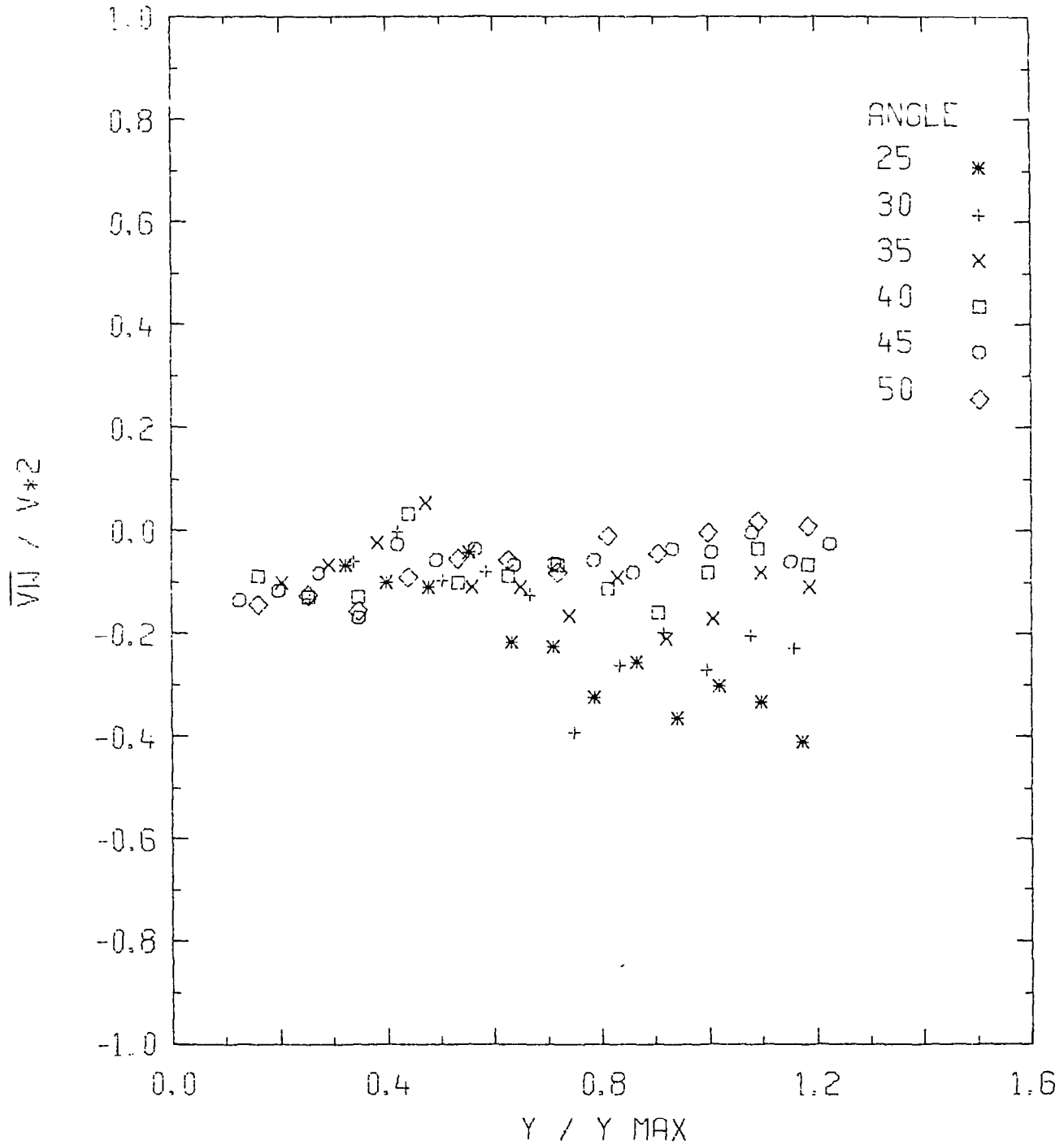

FIGURE 15b TRANSVERSE TURBULENT SHEAR STRESS $\overline{vw}/v^{*2}(\theta)$.
Re 22.6×10^3; p/d = 1.107

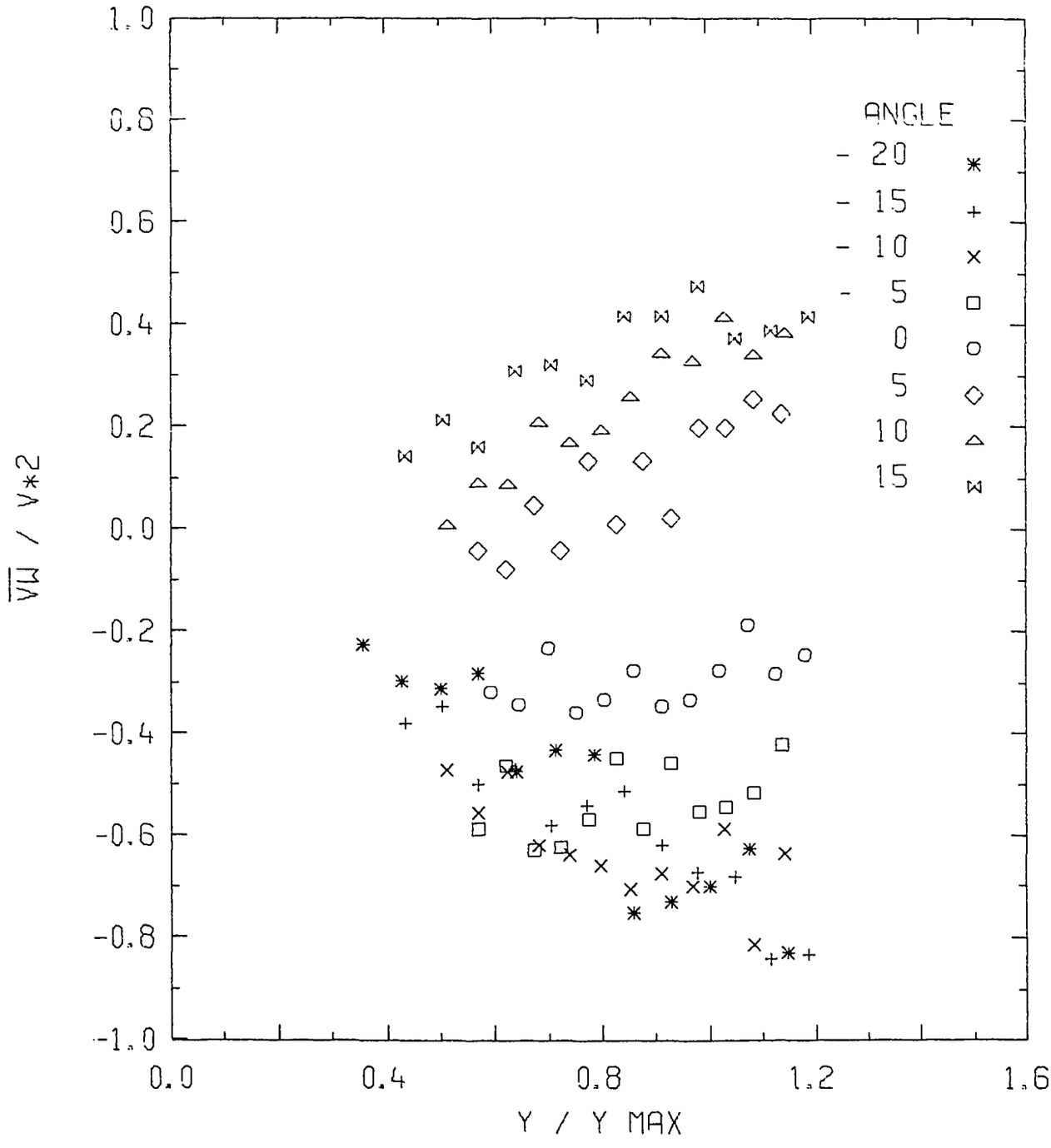

FIGURE 16a TRANSVERSE TURBULENT SHEAR STRESS $\overline{vw}/v^{*2}(\theta)$.
Re = 207.6 × 10^3; p/d = 1.107

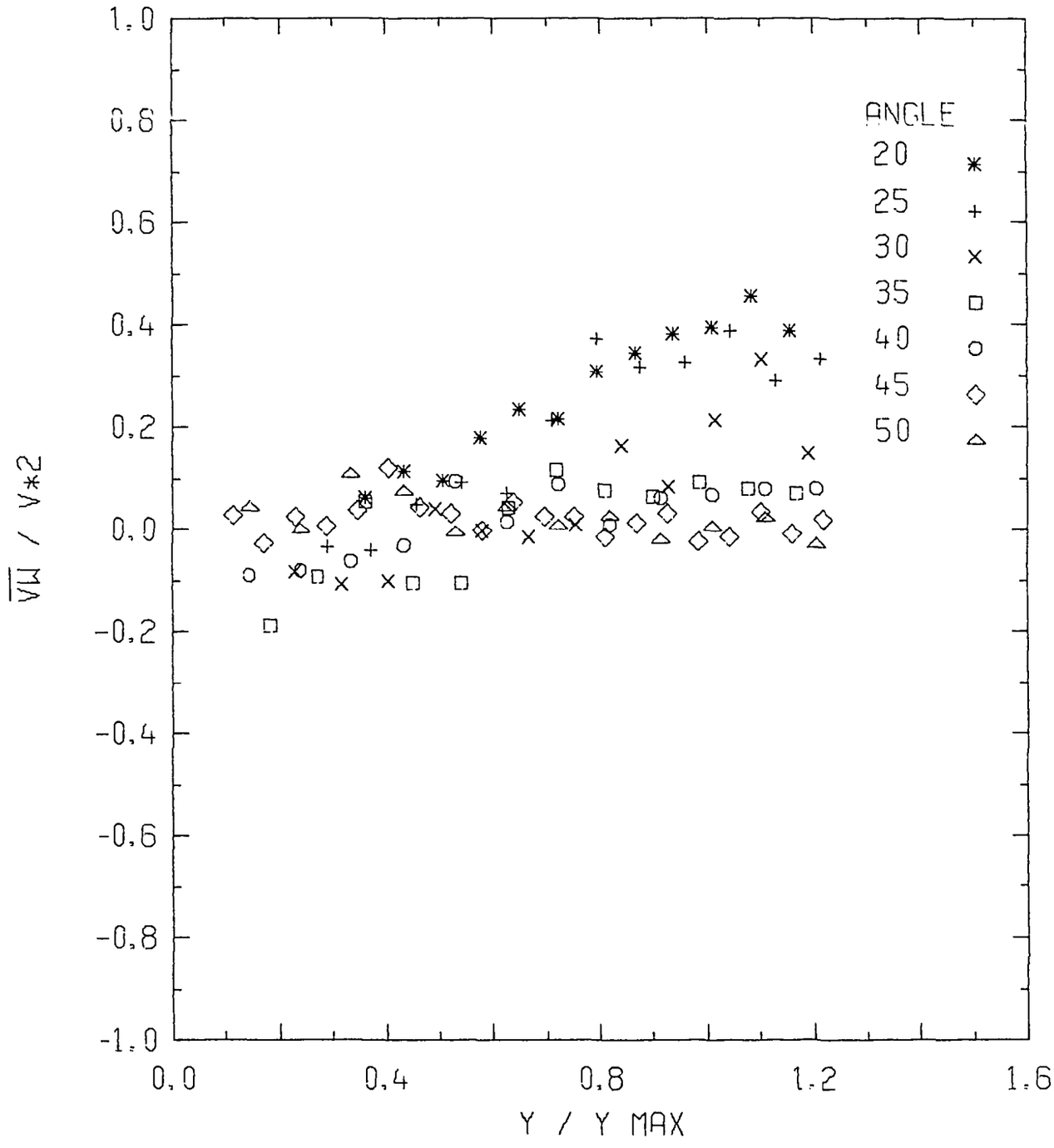

FIGURE 16b TRANSVERSE TURBULENT SHEAR STRESS $\overline{vw}/v^{*2}(\theta)$.
Re = 207.6 × 10^3; p/d = 1.107

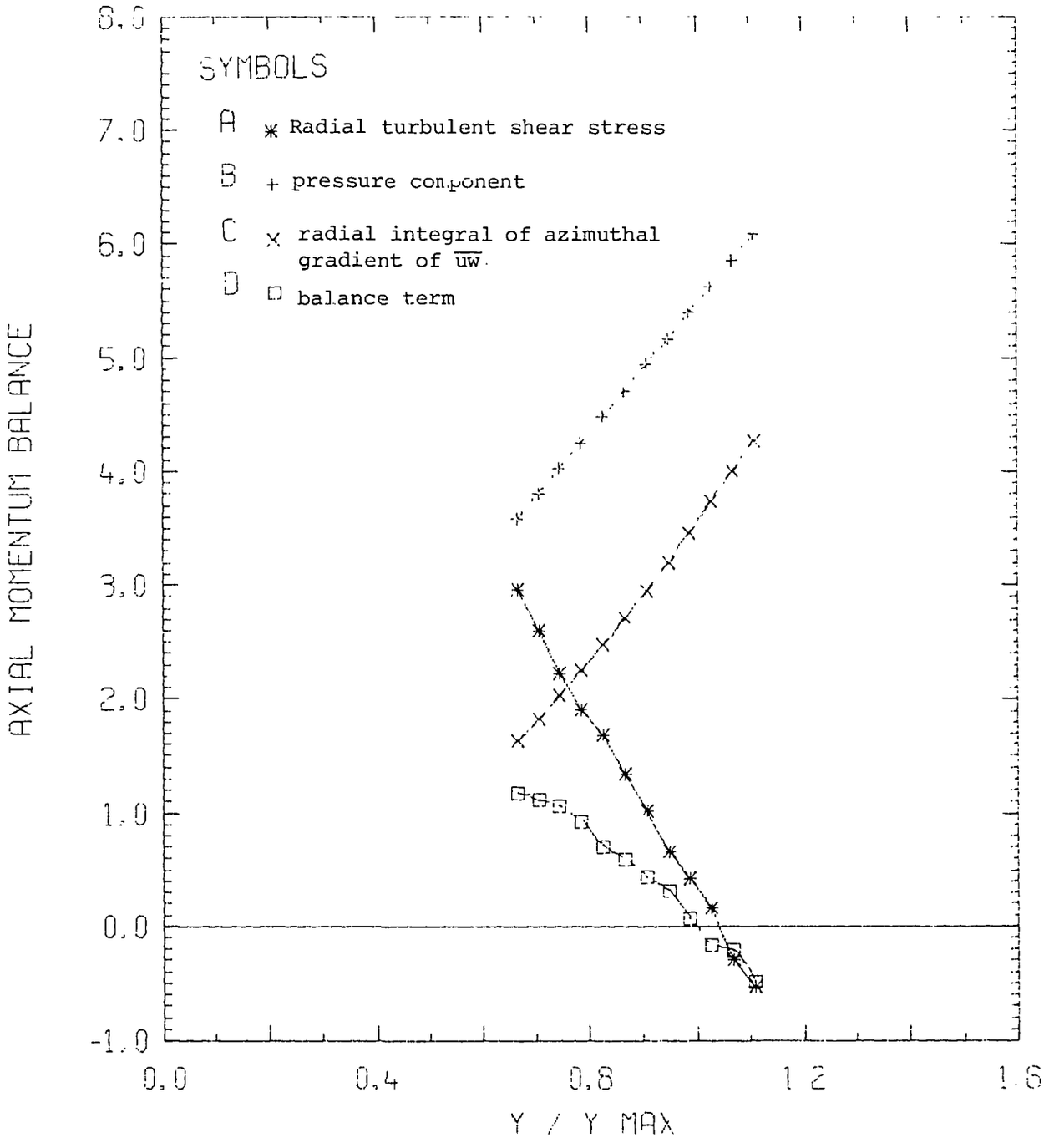

FIGURE 17a AXIAL MOMENTUM BALANCE. Re = 22.6 × 10^3; ANGLE THETA = 0°; p/d = 1.107

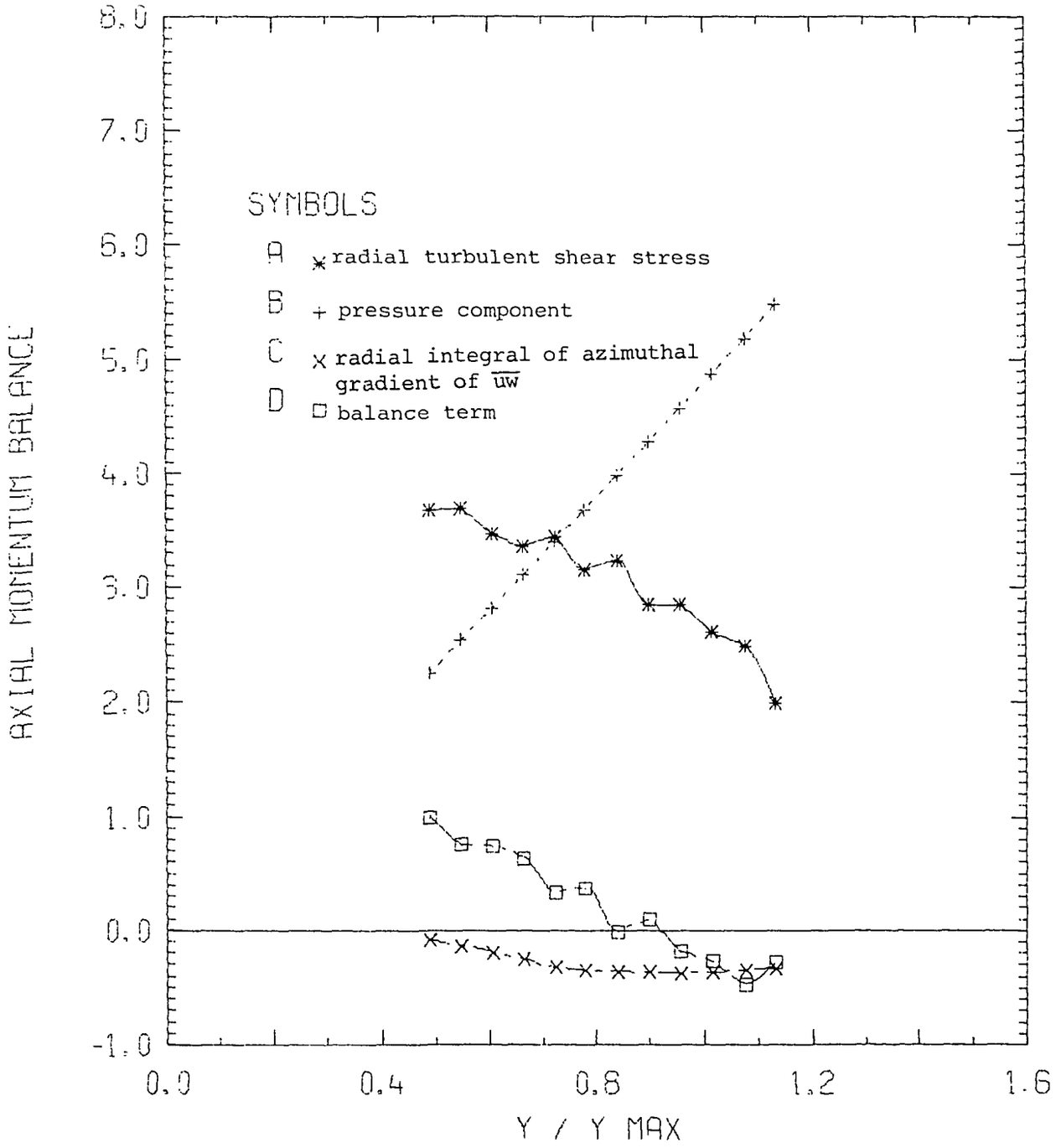

FIGURE 17b AXIAL MOMENTUM BALANCE. Re = 22.6 × 10^3; ANGLE THETA = 15°; p/d = 1.107

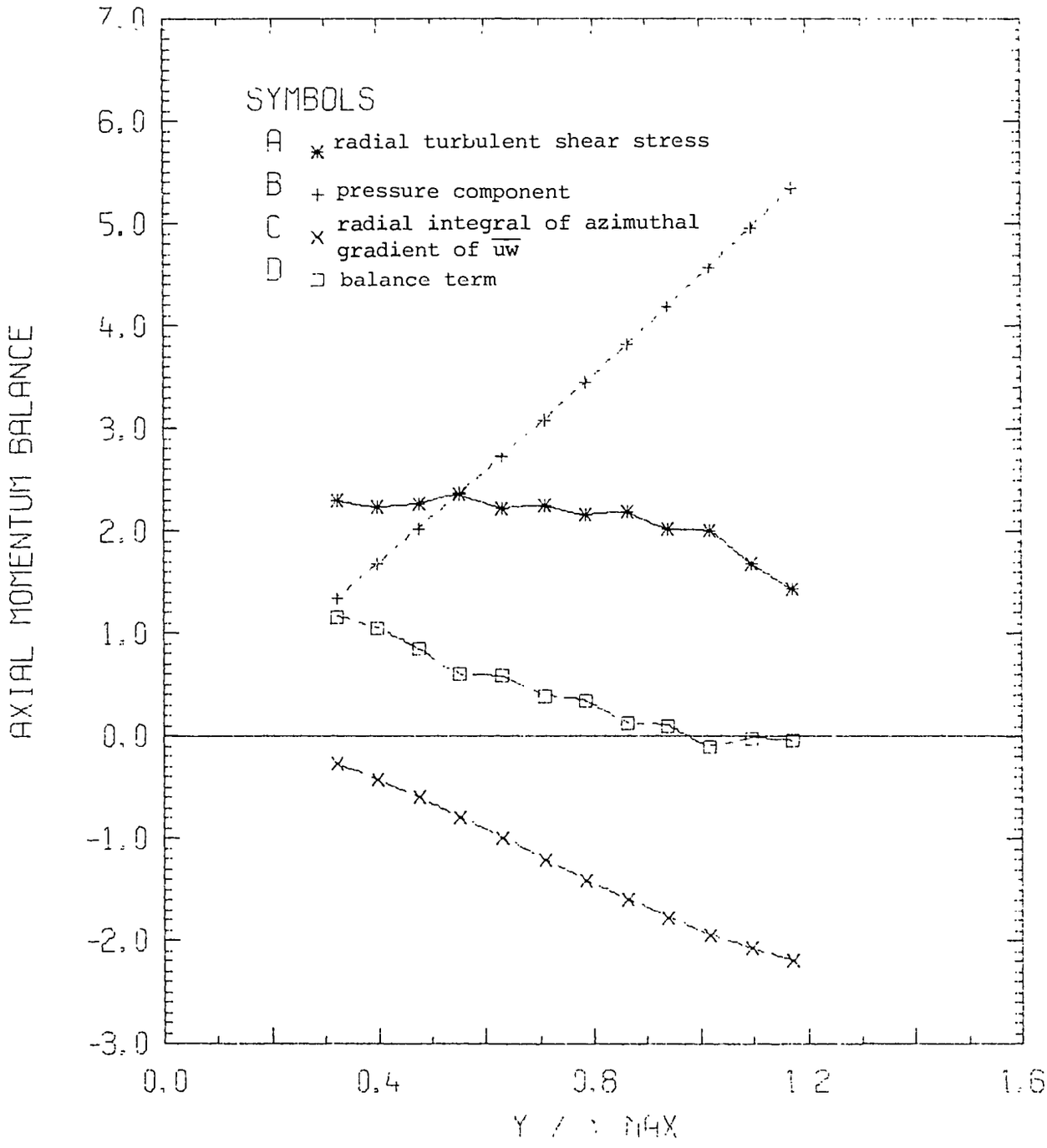

FIGURE 17c AXIAL MOMENTUM BALANCE. Re = 22.6 × 10^3; ANGLE THETA = 25°; p/d = 1.107

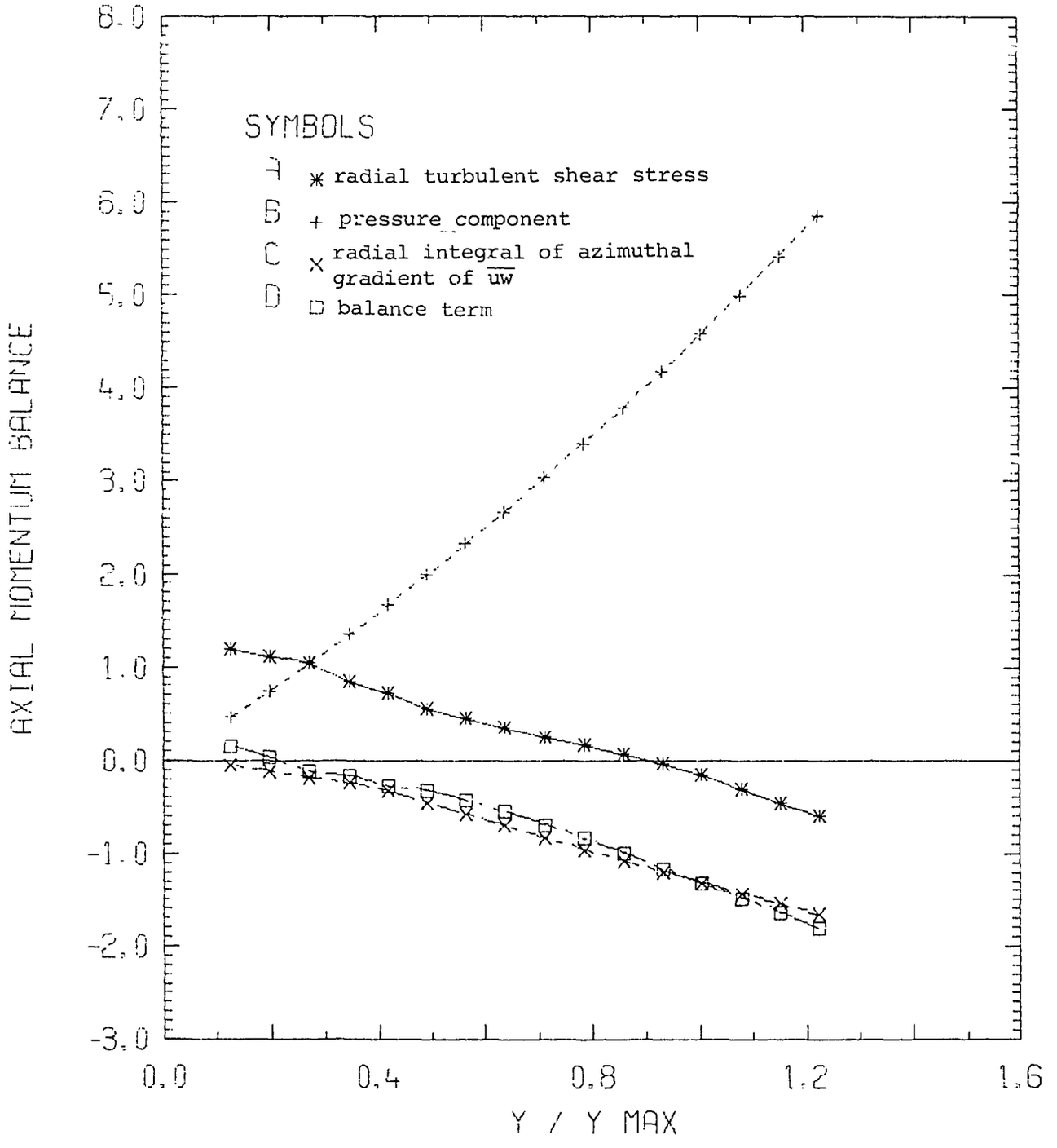

FIGURE 17d AXIAL MOMENTUM BALANCE. Re = 22.6 × 10^3; ANGLE THETA = 45°; p/d = 1.107

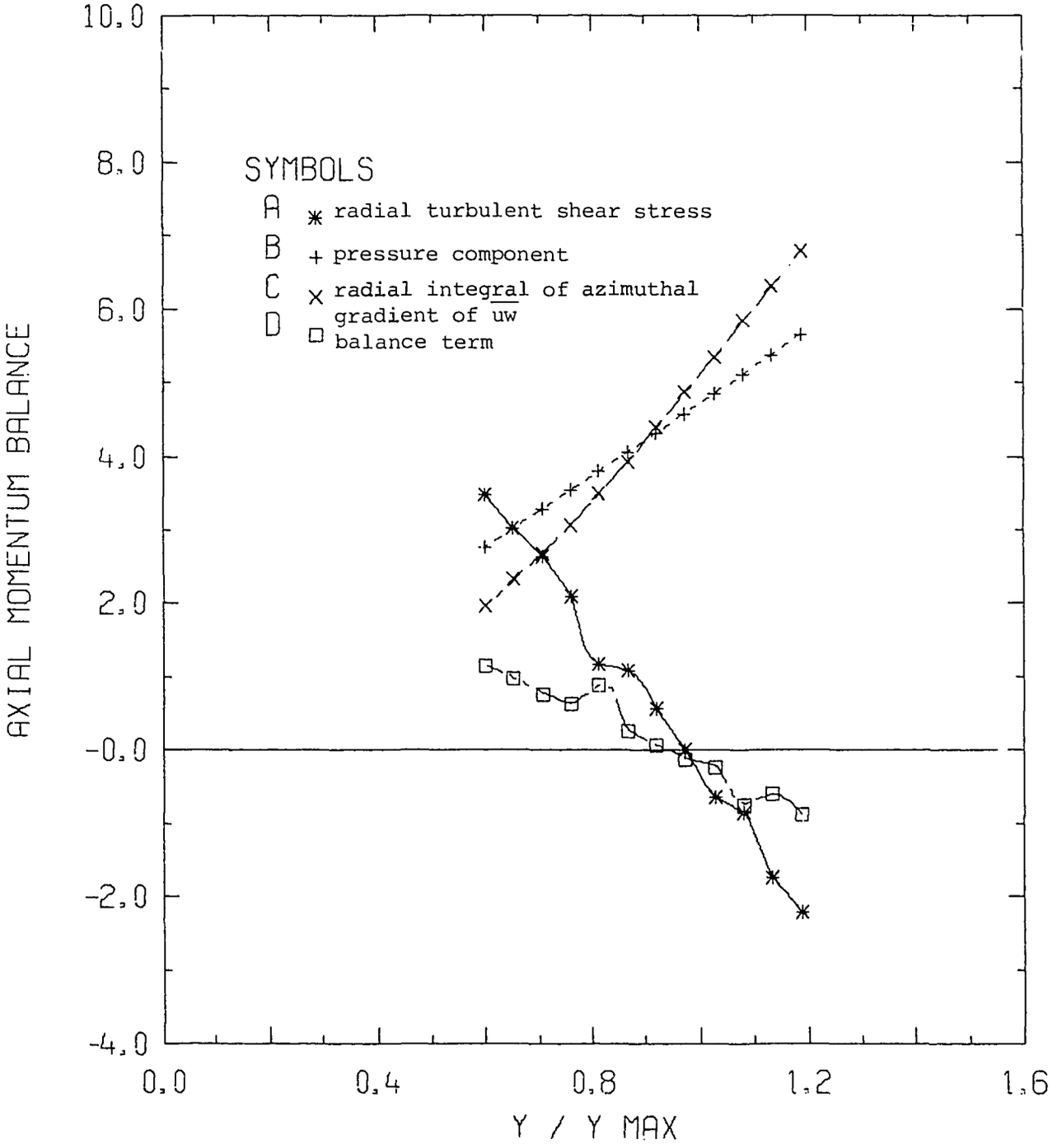

FIGURE 18a AXIAL MOMENTUM BALANCE. Re = 207.6 × 10^3. ANGLE THETA = 0°; p/d = 1.107

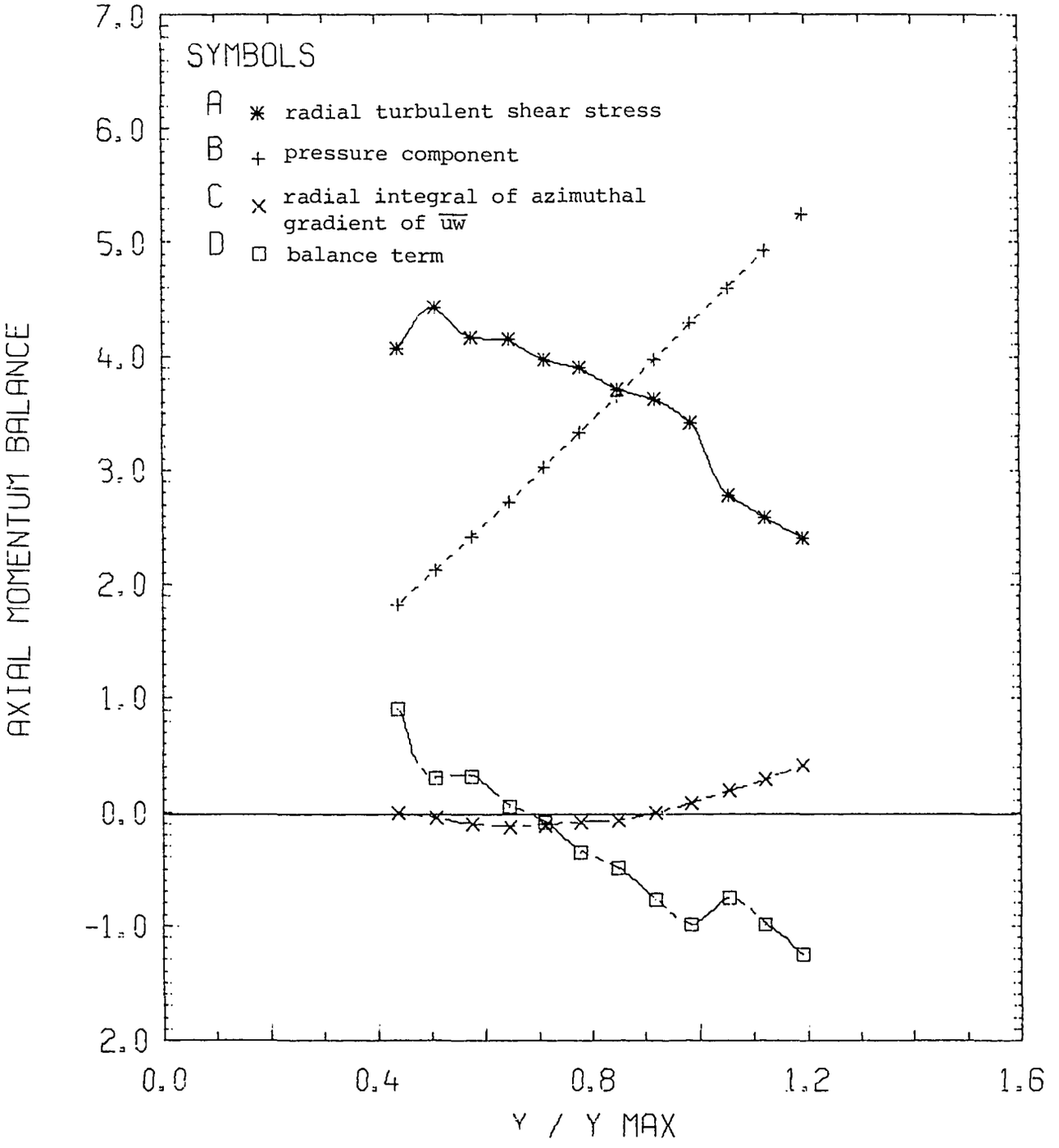

FIGURE 18b AXIAL MOMENTUM BALANCE. Re = 207.6 × 10^3; ANGLE THETA = 15°; p/d = 1.107

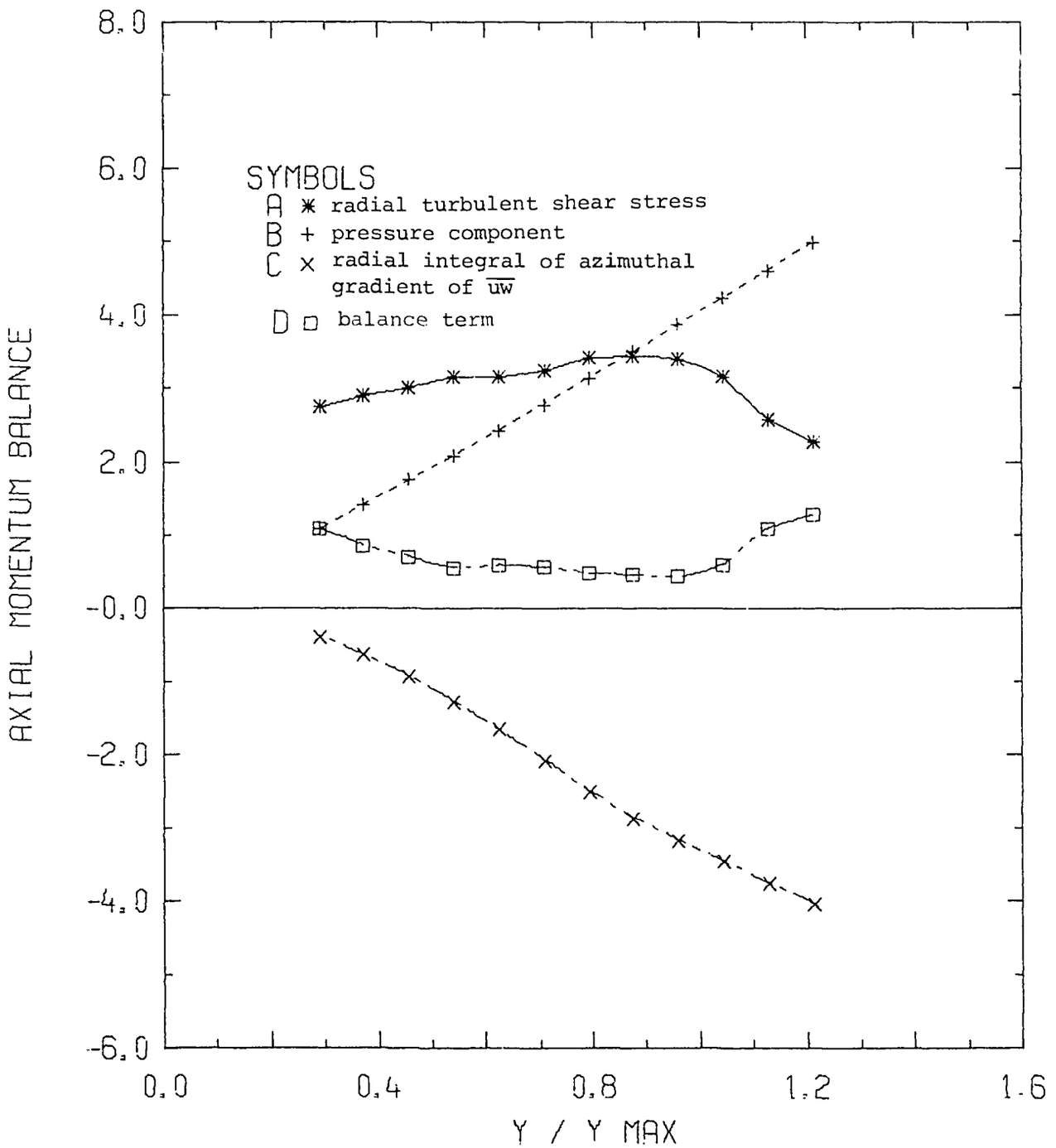

FIGURE 18c AXIAL MOMENTUM BALANCE. Re = 207.6 × 10^3; ANGLE THETA = 25°; p/d = 1.107

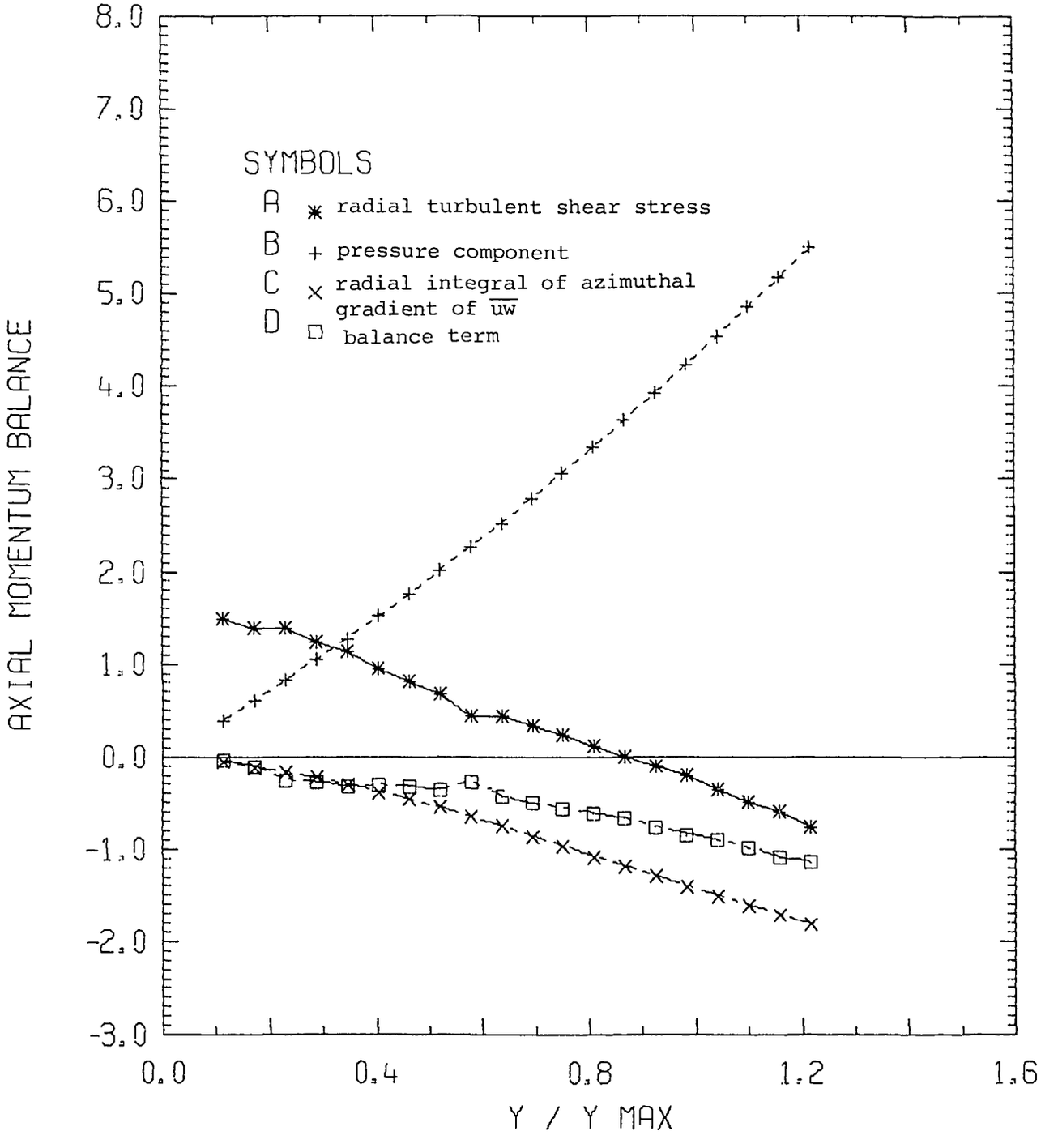

FIGURE 18d AXIAL MOMENTUM BALANCE. Re = 207.6 × 10^3; ANGLE THETA = 45°; p/d = 1.107

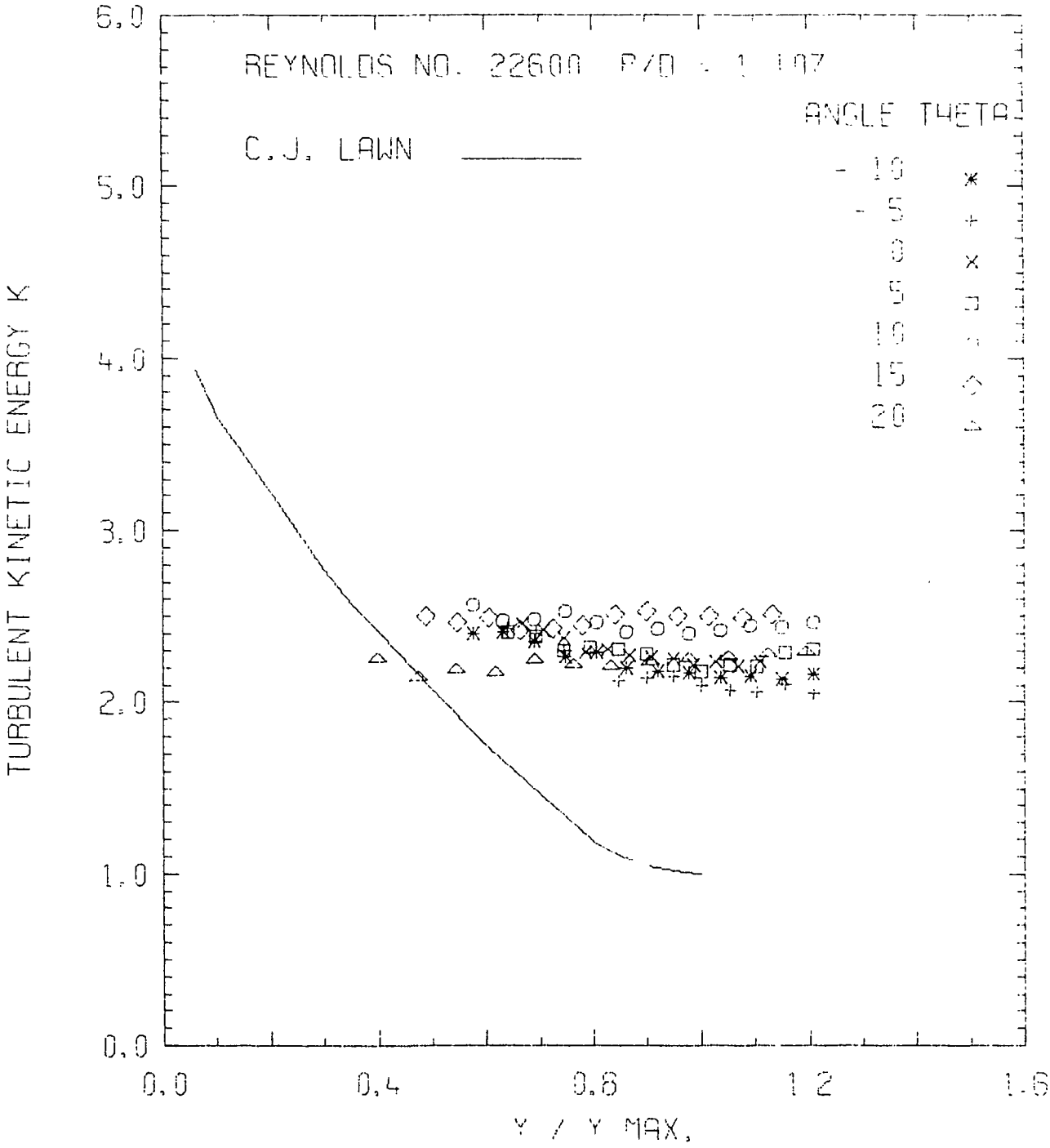

FIGURE 19a TURBULENT KINETIC ENERGY.
Re = 22.6 × 10^3; p/d = 1.107

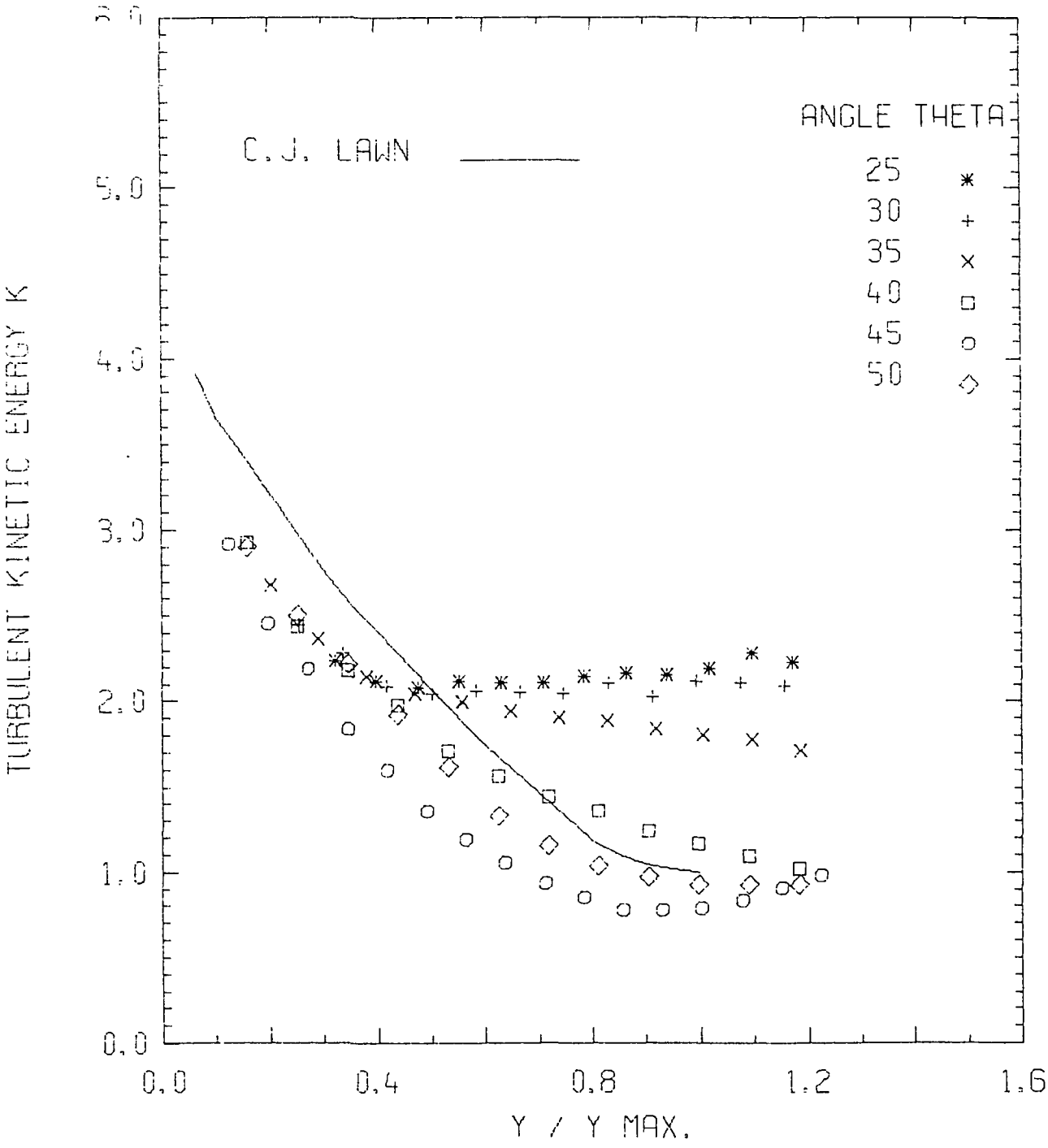

FIGURE 19b TURBULENT KINETIC ENERGY.
Re = 22.6 $\times 10^3$; p/d = 1.107

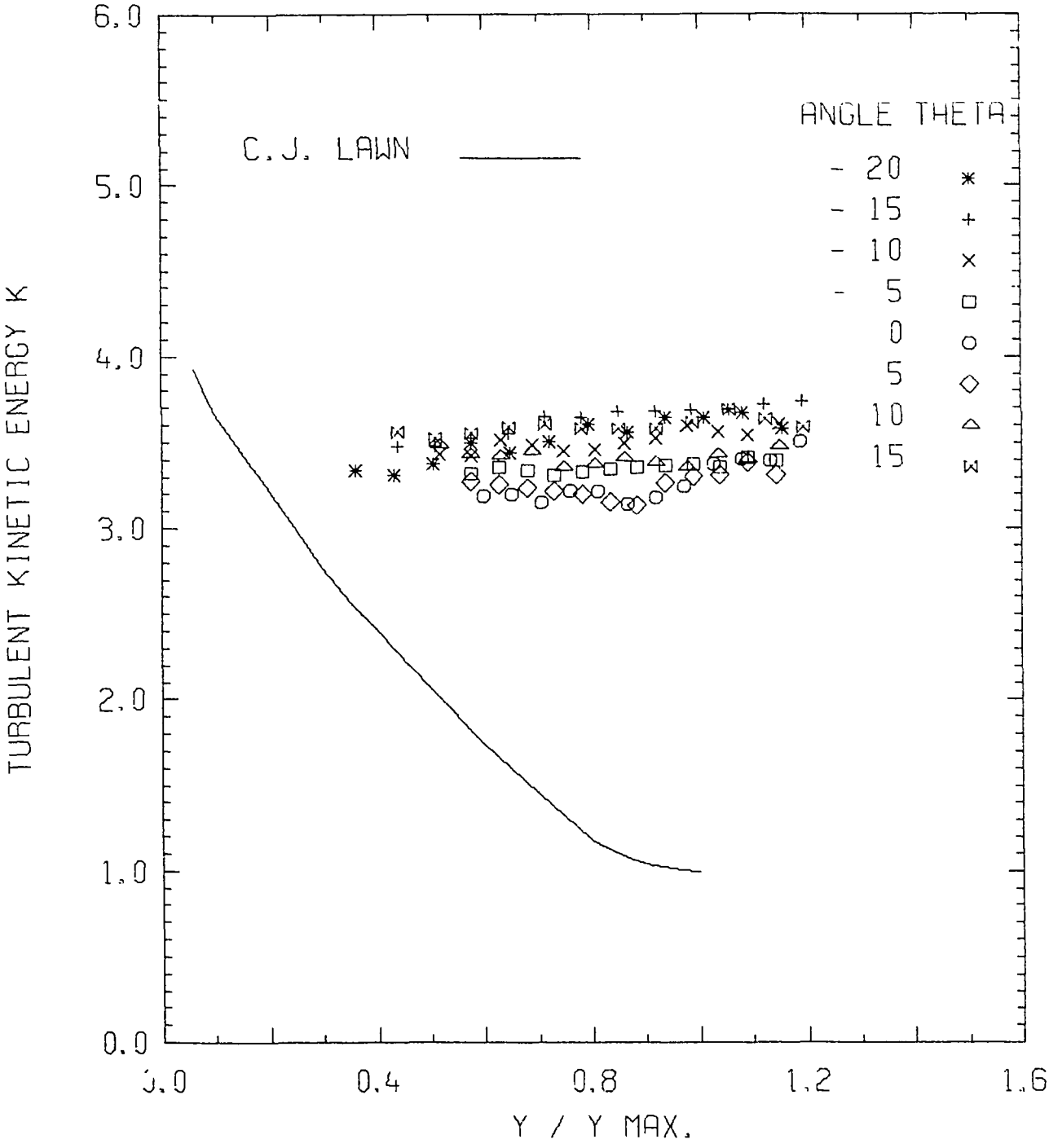

FIGURE 20a TURBULENT KINETIC ENERGY.
Re = 207.6 × 10^3; p/d = 1.107

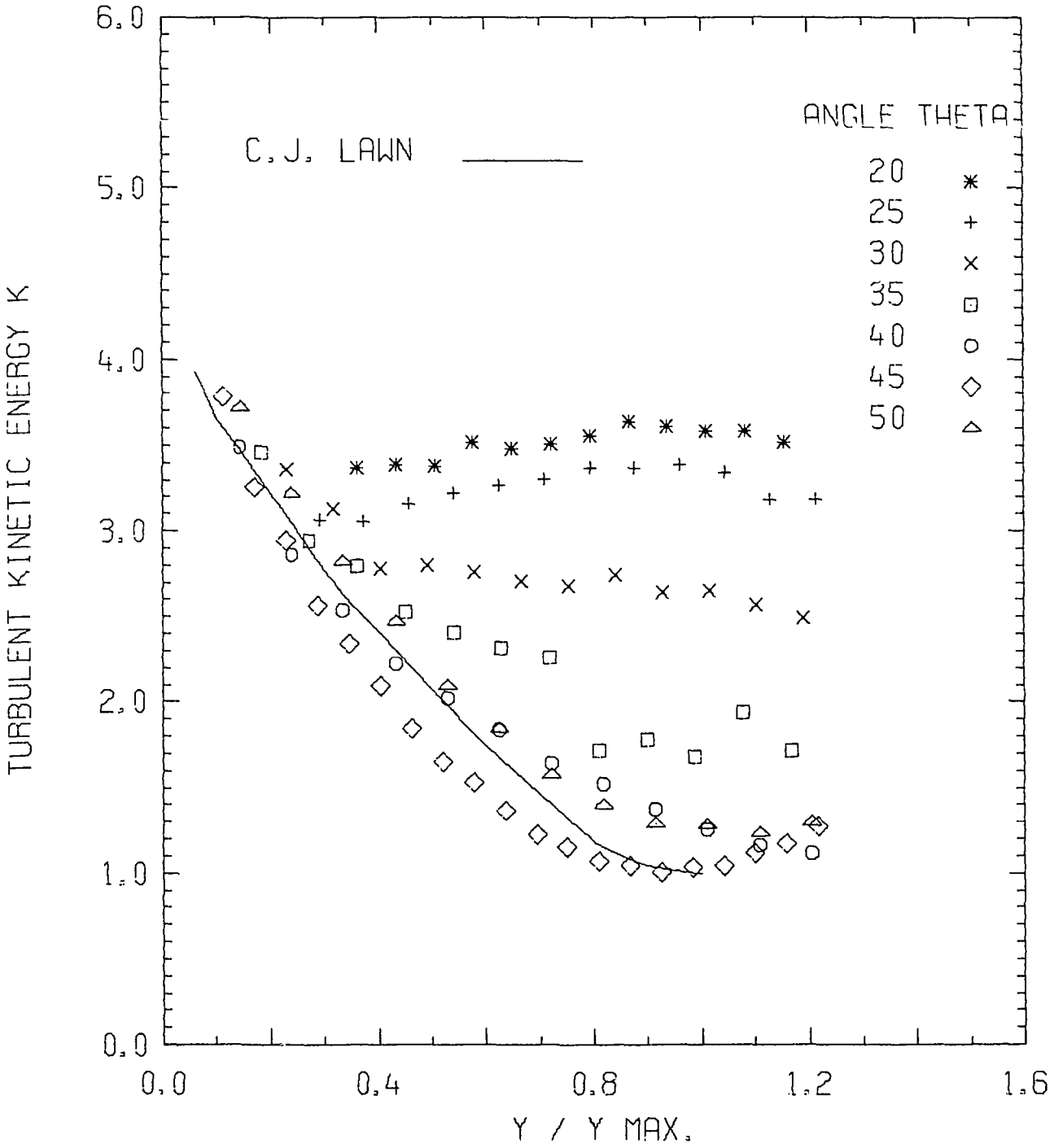

FIGURE 20b TURBULENT KINETIC ENERGY.
Re = 207.6 × 10^3, p/d = 1.107

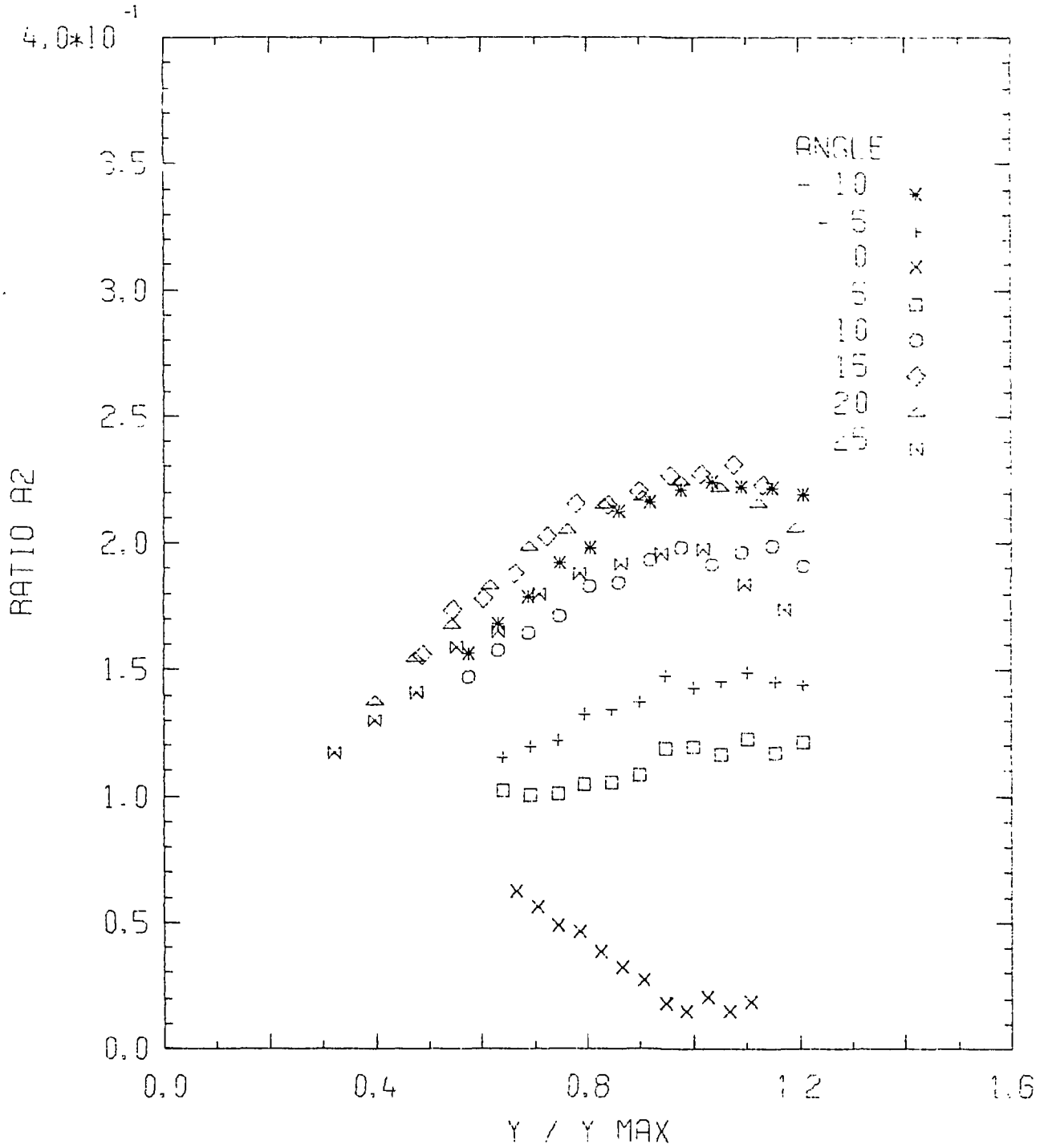

FIGURE 21a REYNOLDS SHEAR STRESS RATIO A2.
Re = 22.6 × 10^3; p/d = 1.107

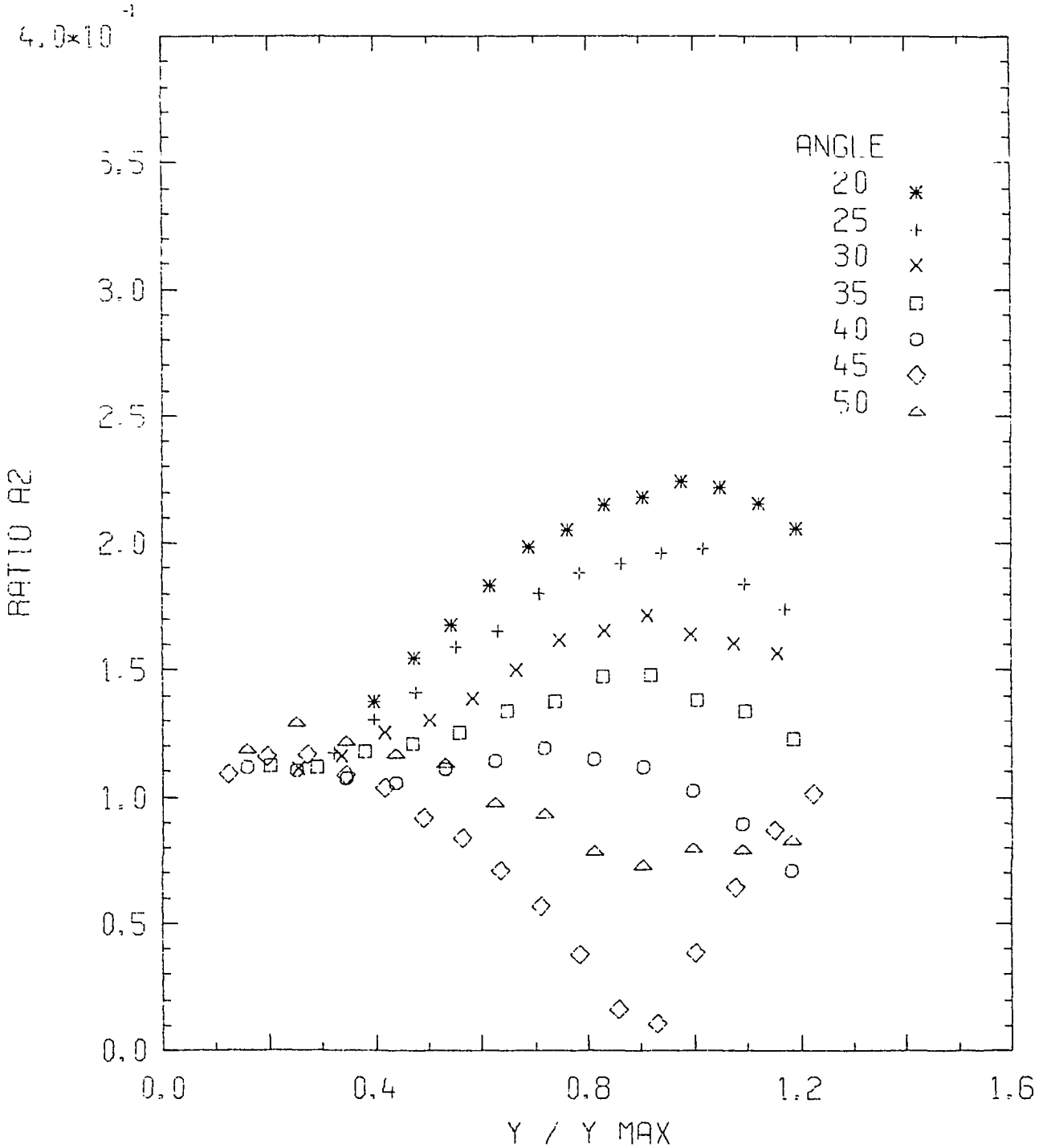

FIGURE 21b REYNOLDS SHEAR STRESS RATIO A2.
Re = 22.6 × 10^3; p/d = 1.107

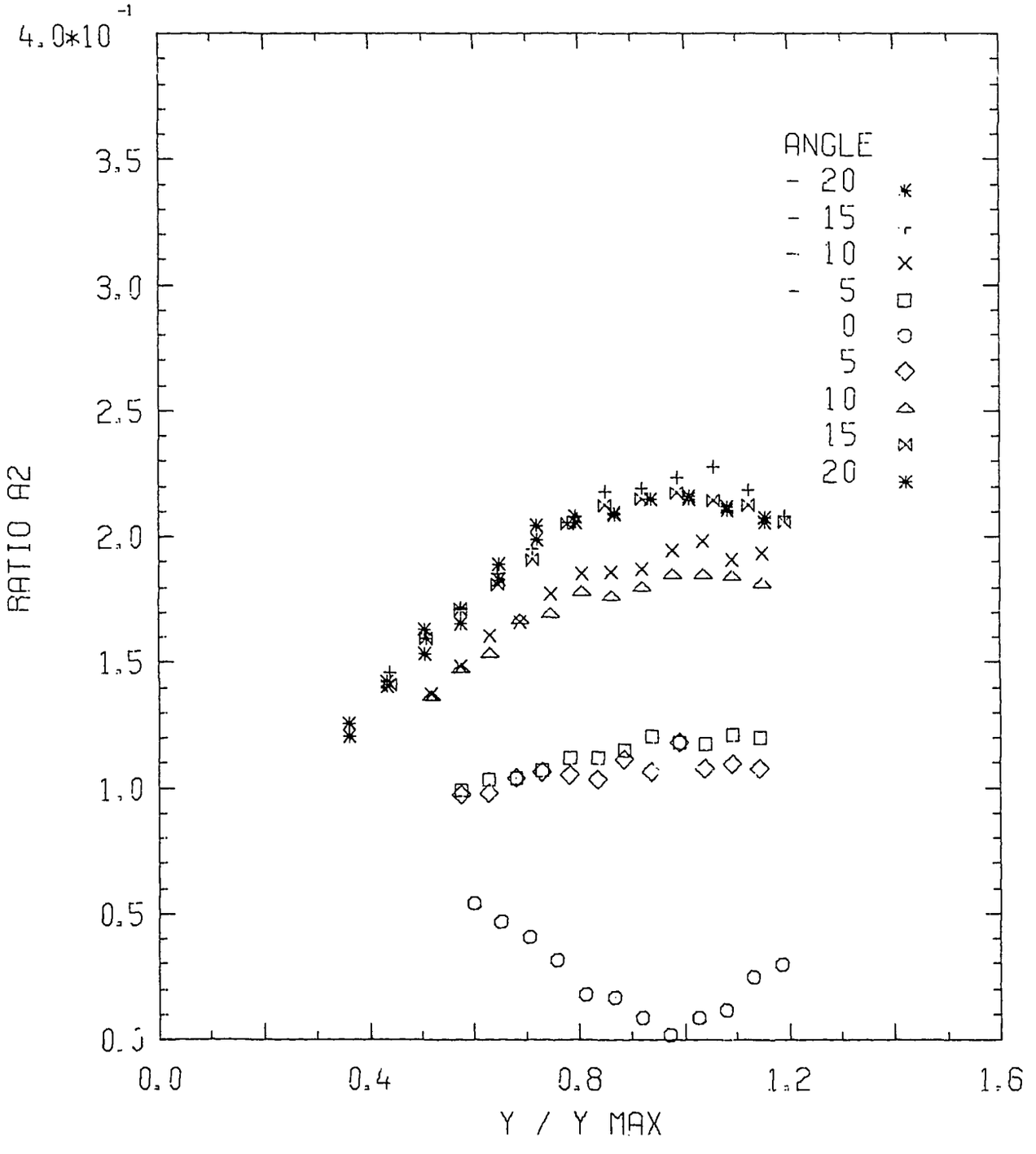

FIGURE 22a REYNOLDS SHEAR STRESS RATIO A2.
Re = 207.6 × 10^3; p/d = 1.107

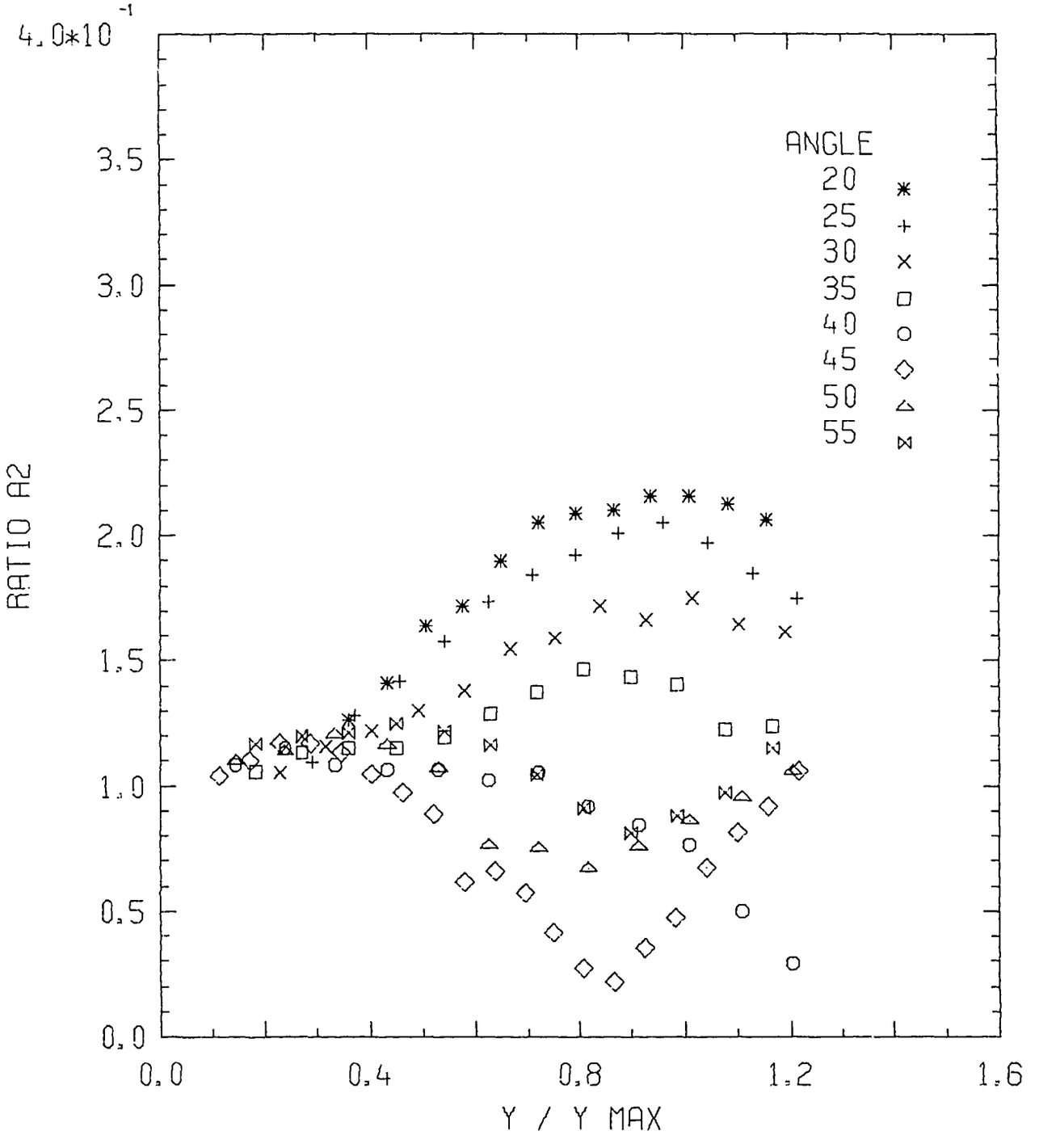

FIGURE 22b REYNOLDS SHEAR STRESS RATIO A2.
Re = 207.6 × 10^3; p/d = 1.107